Passive Components for Dense Optical Integration Based on High Index-Contrast

by

Christina Manolatou

M.S. in Electrical Engineering and Computer Science,
MIT 1995

Submitted to the Department of Electrical Engineering and Computer Science in partial fulfillment of the requirements for the degree of

Doctor of Philosophy

at the

MASSACHUSETTS INSTITUTE OF TECHNOLOGY

June 2001

Author .....
Dept. of Electrical Engineering and Computer Science
June 2001

Certified by .....
Hermann A. Haus
Institute Professor
Dept. of Electrical Engineering and Computer Science
Thesis Supervisor

Accepted by .....
Arthur C. Smith
Chairman, Committee on Graduate Students
Dept. of Electrical Engineering and Computer Science

Passive Components for Dense Optical Integration Based on High Index-Contrast

by

Christina Manolatou

M.S. in Electrical Engineering and Computer Science, MIT 1995

Submitted to the Department of Electrical Engineering and Computer Science, on May 4 2001, in partial fulfillment of the requirements for the degree of Doctor of Philosophy

Abstract

This work presents a theoretical and numerical investigation of high index-contrast passive components that can serve as building blocks at the end-pointsand nodes of WDM communications systems. The main characteristic of these structures is their miniature size (on the order of the optical wavelength), and their low radiation loss due to the strong light confinement in high index-contrast systems. Thus large scale, high density optical integration may be possible with the associated advantages of increased functionality, compactness and low-cost. Novel devices for filtering, optical interconnections and coupling to fibers are presented, specifically: a class of resonant add/drop filters that rely on symmetry and degeneracy of modes, low-loss right-angle bends, splitters, crossings based on transmission cavities, and fiber-chip couplers based on cascades of resonators or lensing mechanisms. Their operating principles are explained and an approximate analysis is obtained by analytical methods such as coupled-mode theory and gaussian/ray optics. For accurate analysis and optimized design, extensive numerical simulations are performed using the Finite Difference Time Domain method. The numerical results are in good agreement with the experimental data obtained for bends that were farbricated and tested at MIT. Issues that remain to be addressed for this technology to be viable and possible future directions are also discussed.

Thesis Supervisor: Hermann A. Haus
Title: Institute Professor

Acknowledgements

I am grateful to prof. Haus for giving me the opportunity to work on such interesting projects and for his guidance and advice all these years. I would also like to thank prof. Ippen and Kimerling for being in my committee; their commends and suggestions helped improve this thesis.

Most of this work would not have been possible without access to the Cray in the San Diego and Texas supercomputer facilities.

In the early stages of this work Shanhui Fan and Pierre Villeneuve, then in Prof. Joannopoulos group, helped me enormously with both the understanding of basic concepts but also with the numerical modelling. I learnt a lot by collaborating with them as well as with th Steven Johnson. I would also like to thank Brent Little for all the discussions, new ideas and advice.

In the last few years I have enjoyed the collaboration and exchange of ideas with many people from Prof. Kimerling's group: Desmond Lim, Kevin Lee, Kazumi Wada, Anu Agarwal and others.

For the most part of my 5 years in this group I have been lucky to share an office with Jalal Khan; I have greatly enjoyed his company and our conversations that have covered all sorts of topics ranging from research to sports. The past one year I have also benefited from sharing my office with Milos Popovic, amazingly smart and hard working but also a great guy.

It would have been impossible to keep a balance in my life as a PhD student and avoid being consumed by stress if I hadn't enjoyed myself so much away from work. My dorm, Ashdown House, with its great community and many friendships helped me feel at home here from the first day. Interacting or becoming friends with people from all over the world, both within and outside MIT, from different cultures and backgrounds, has been perhaps a most valuable experience; I would need a lot fo space to list them all. For the last few years I have also been part of the great running community of Boston. This experience has made me more self-confident and has offered me some unforgettable and exciting moments as well as a reminder that hard work and consistency pay off. For that I am grateful to my teammates and coaches in the Greater Boston Track Club and more recently in the Boston Athletic Association.

A very special person has helped make the last 5 years some of the happiest in my life. Farhan has been my source of inspiration and encouragement, infinitely understanding and caring; words cannot express how much he means to me.

Last but not least, I am grateful to my parents for essentially preparing me for this experience all my life, and for their support when I decided to come to MIT, although they knew how much they would miss me. To them I dedicate this thesis.

Christina Manolatou

Table of Contents

List of Figures

Chapter 1

Introduction

1.1 Motivation

The concept of integrated optics has existed since 1969 when a complete work of waveguide analysis and design of waveguide bends and filters was presented [1],[2]. However it is only recently that favorable conditions for the development of this technology have emerged. The bandwidth requirements for internet services and the promise of high bandwidth links to homes are driving the development of high data-rate communication systems. Wavelength Division Multiplexing (WDM), which is the main approach to increasing the capacity of optical fibers, relies heavily on devices for efficient signal processing at the optical level, thus creating a need for low-cost high-performance integrated optical devices.

The minimum size of integrated optics devices depends on the dielectric contrast of the layers used to form the components. High index-contrast waveguides refer to waveguides with a high-index core and a low-index cladding. Examples of high index-contrast systems (with the advantage that they are compatible with silicon ULSI processing), are strip waveguides of silicon (Si) or silicon nitride (Si_3N_4), on a silicon oxide (SiO_2) substrate with air or SiO_2 cladding. The index differences of ~2-2.5 and ~0.5-1, respectively are much larger than those of typical wave guiding systems, such as optical fibers or doped silica waveguides with index-differences as small as 0.01. High index-contrast waveguides are characterized by stronger light confinement and much smaller cross-sectional dimensions (in the sub micron range) than the above mentioned typical wave guiding systems, which have cross-sectional dimensions on the order of 10x10 μm^2. They also tend to have stronger polarization dependence, greater scattering loss caused by sur-

face roughness and connection to fibers is much more difficult. On the other hand, the light is strongly confined in high index-contrast systems and thus coupling to radiation modes is very small. Moreover, because of the miniature size of such devices, even a high dB/cm loss corresponds to a low overall loss. Thus, abrupt changes in the light flow can be achieved very efficiently in a very small area, allowing the dense integration of optical devices on a chip.

The idea that large index differences lead to miniaturized devices is not new but has only recently gained interest for several reasons [61]: High quality crystalline materials with high dielectric contrast were not available. Tolerances to device imperfection especially with regard to the interfaces between the low- and high- index materials are demanding. Critical dimensions as small as 100nm are involved which were well out of the reach of lithography previously available. Now, advances in nanofabrication allow the consideration of high index-contrast structures of sub micron dimensions for integrated optics.

The devices examined in this thesis are passive devices for wavelength filtering and optical inteconnections. Such devices are essential components of photonic integrated circuits (PIC). PICs contain optically interconnected devices on an appropriately designed solid state substrate, that successively reroute or process the signal while it is still in its optical form. Of great importance is also the ability to couple light and efficiently in and out of the PIC, which a very challenging task due to the large mode mismatch between fibers and integrated waveguides.

The common feature of many of the devices presented here, is that their operation is based on resonance and that their sizes are on the order of the optical wavelength. Their behavior is modelled numerically using the Finite Difference Time Domain (FDTD)

method, while analytical methods, such as the Coupled Mode Theory (CMT) in time serve as a starting point.

1.2 Outline of the thesis

Using the theoretical and numerical tools presented in chapters 2 and 3, respectively, this thesis investigates: symmetric resonant Channel Dropping Filters (CDF) for WDM applications, in chapter 4, high-performance waveguide bends, splitters, and crosses in chapter 5, fiber-chip couplers, in chapter 6 and finally, conclusions and future work, in chapter 7.

1.2.1 Theoretical background

The final design and modelling of our optical structures relies heavily on numerical simulations. However, most of the times it is necessary to start with a theoretical analysis that provides a proof of concept, an intuitive understanding of the operating principles and even an initial guess for the design parameters to be optimized through simulations. Analytical methods we use include: Coupled Mode Theory (CMT) in time for filters and other resonant structures, Gaussian beams and ray optics for lensing structures, Effective Index Method (EIM) to reduce a 3D analysis into two dimensions, etc. A brief theoretical background for these methods and some basic examples that will be useful throughout this thesis are presented in next chapter.

1.2.2 The FDTD method

The method of choice for modelling waveguide based devices, has traditionally been the Beam Propagation Method (BPM), [8],[9]. Because of its inherent assumptions, this method is limited to weakly guided structures with little variation along the propagation direction. An alternative method without such limitations is the Finite Difference Time Domain (FDTD) method [13],[14] (and references therein) which has been extensively applied to the design of complicated RF and microwave devices. As optical devices approach the size of the optical wavelength the FDTD method has emerged as a powerful

tool for the modeling and design of integrated optics, e.g. [12].

The FDTD method solves the full-vector Maxwell's curl equations without any approximation other than the replacement of differential equations with finite differences on a discrete mesh [15]. Very complex structures can thus be modelled in two or three dimensions, provided their features are sufficiently resolved by the discretization. In practice, because the 3D FDTD often has prohibitive time and memory requirements, the 2D method is preferred which, combined with the Effective Index Method (EIM) in the third dimension, offers a sufficiently accurate analysis of most planar devices. Another important limitation of the FDTD method is that a finite spatial domain must be used to model unbounded geometries, so approximate representations of open boundary conditions are used. The challenge is to terminate the mesh in a way that allows scattered waves to leave the computational domain with negligible spurious back-reflections from the border and various methods have been proposed [16]-[20]. Although it is computationally intensive, the FDTD method has the advantage that with only one simulation we can find the system response over a wide frequency range through Discrete Fourier Transform (DFT) or Fast Fourier Transform (FFT) of the time dependent data, thus it is well suited for modelling resonant structures.

1.2.3 Resonant channel add/drop filters

Resonator-based integrated devices can interact with optical signals in a PIC in such a way as to selectively transmit, reflect or detect the signals that are resonant with these devices. Channel add/drop filters can access one channel of a wavelength division multiplexed signal without disturbing the other channels and are therefore important elements in WDM communications. Resonant filters are attractive candidates because they can potentially realize the narrowest linewidth for a given device size and because a number of coupled resonators can shape the simple Lorentzian response of a single resonator yielding desir-

able higher order characteristics[34],[36],[48]. Ring and disk resonators based on semiconductor waveguides with a very large lateral refractive index contrast can have sizes on the order of the optical wavelength and theoretically achieve very high radiation quality factors (Q) due to small bending loss [36],[38]. This small size leads to a free spectral range (FSR) as wide as 6THz (~50nm) capable of accommodating a set of WDM channels across the erbium-doped amplifier bandwidth. However the surface-roughness-induced radiation loss and coupling between counter-propagating waves in a ring [41] can deteriorate the filter performance. An alternative way to achieve the same behavior is based on the excitation of two degenerate symmetric and anti-symmetric standing wave modes in a resonant system with symmetry [44],[47]. An intuitive understanding and approximate prediction of the filter behavior can be gained through CMT in time, but for accurate modelling extensive simulations are required. The FDTD method is particularly suited for these type of structures and is our main numerical tool.

1.2.4 Low-loss waveguide components

The dense integration of photonic devices creates the need for components that provide complicated low-loss optical interconnections within a small chip area. In this work we show that we can use resonant cavities appropriately placed in high index-contrast waveguide bends, splitters and crosses, to greatly enhance the performance of these components [67]. On resonance, the transmission is maximized and the reflection minimized, limited only by the radiation loss. The peak values are set by the ratio of the quality factors of the resonator associated with coupling to radiation and to the waveguide modes, respectively. The name High Transmission Cavity (HTC) has been adopted for these components.

FDTD simulations show that it is possible to achieve up to 99% transmission in sharp 90° bends using this concept. Two of these bends placed back to back can make up a T-

splitter with similarly high performance and the ratio of output power in its two output ports can be varied by displacing the input waveguide with respect to the junctions symmetry plane. Crossings with a cavity of fourfold symmetry at the center can be designed with more than 95% transmission and ~ -30dB crosstalk (power leaking sideways) are also demonstrated numerically.

1.2.5 Fiber-PIC coupling

High index-contrast systems may enable high density optical integration. However, for this technology to be viable in optical communication systems it is necessary to be able to couple light efficiently from an optical fiber into the optical devices on an optical chip and vice versa. This is a very challenging task due to the large mismatch between the fiber mode and the integrated waveguide mode in both size (~10μm vs. <~1μm) and shape (circular vs. highly elliptical).

In this work we investigate theoretically the possibility of coupling light from a fiber into high index contrast waveguides, using structures only a few μm long, much shorter than mode converters encountered in the literature. We present two coupling schemes for lateral mode conversion, one employing cascaded square resonators and one employing lens-like structures. The latter is much easier to design and results in better performance (~90% coupling efficiency). The combination of this mechanism with graded index lensing through a layered structure in the vertical direction is also investigated in a 3D mode conversion scheme.

Chapter 2

Theoretical Background

This chapter contains the theory which is the basis for the analytical calculations in this thesis.

2.1 Modes in optical waveguides

A bidirectional waveguide along the z-axis is invariant under z-mirror symmetry. Any field propagating in the waveguide can be transformed into a symmetrical field propagating in the reverse direction which also satisfies Maxwell's equations. The formalism presented next, closely follows [3].

2.1.1 Normal modes

The normal modes of a waveguide are sourceless fields with a $e^{-j\beta z}$ z-dependence that remain bounded for all x,y. We assume a $e^{j\omega t}$ time dependence. Writing the fields out as

$$\begin{aligned} \vec{E} &= \vec{E}_T + \hat{z}E_z \\ \vec{H} &= \vec{H}_T + \hat{z}H_z \end{aligned} \tag{2.1}$$

Maxwell's curl equations can be written as:

$$\begin{aligned} \beta\vec{E}_T - j\nabla_T E_z &= -\omega\mu\hat{z}\times\vec{H}_T \\ \beta\vec{H}_T - j\nabla_T H_z &= \omega\varepsilon\hat{z}\times\vec{E}_T \\ \nabla_T(\hat{z}\times\vec{E}_T) &= j\omega\mu H_z \\ \nabla_T(\hat{z}\times\vec{H}_T) &= -j\omega\varepsilon E_z \end{aligned} \tag{2.2}$$

If there is a single solution for a given β the mode is non-degenerate. In the case of lossless waveguides β can be purely real or purely imaginary and the corresponding modes are called propagating or evanescent. For non-degenerate modes:

- For real β: $\vec{E}_T$, $\vec{H}_T$ are purely real and E_z, H_z are purely imaginary.

• For imaginary β: $\vec{E}_T, \vec{H}_T$ are purely imaginary and E_z, H_z are purely real.

Forward propagating modes are characterized by some abstract index $\nu \in N$ and are related to backward propagating modes $-\nu$ by z-mirror symmetry:

$$\begin{aligned} \text{mode} \quad +\nu: \quad & \{\vec{e}_{T\nu}(x,y), e_{z\nu}(x,y)\hat{z}, \vec{h}_{T\nu}(x,y), h_{z\nu}(x,y)\hat{z}\}e^{-j\beta_\nu z} \\ \text{mode} \quad -\nu: \quad & \{\vec{e}_{T\nu}(x,y), -e_{z\nu}(x,y)\hat{z}, -\vec{h}_{T\nu}(x,y), h_{z\nu}(x,y)\hat{z}\}e^{j\beta_\nu z} \end{aligned} \tag{2.3}$$

Note that in lossless waveguides, due to time reversal symmetry, the backward propagating modes are related to the complex conjugate of the forward propagating modes as follows:

$$\begin{aligned} \vec{e}_{-\nu} &= \vec{e}_\nu{}^* \\ \vec{h}_{-\nu} &= -\vec{h}_\nu{}^* \end{aligned} \tag{2.4}$$

In open waveguides the set N is divided into a set of discrete points (which can be empty) and a continuous set. Discrete points correspond to the discrete (guided) modes that carry finite power and have a real physical meaning. The continuous parts of N correspond to the continuous (radiating) modes that do not carry finite power and do not have any individual physical existence; however integrals over these modes may be physical fields.

2.1.2 General form of guided fields

For any part of a waveguide limited by two cross-sectional planes, the general solution of the source free Maxwell's equations is a sum of forward and backward propagating modes.

$$\begin{Bmatrix} \vec{E}(x,y,z) \\ \vec{H}(x,y,z) \end{Bmatrix} = \sum_{\nu \in N} \left[A_\nu e^{-j\beta_\nu z} \begin{Bmatrix} \vec{e}_{+\nu}(x,y) \\ \vec{h}_{+\nu}(x,y) \end{Bmatrix} + A_{-\nu} e^{j\beta_\nu z} \begin{Bmatrix} \vec{e}_{-\nu}(x,y) \\ \vec{h}_{-\nu}(x,y) \end{Bmatrix} \right] \tag{2.5}$$

Since the forward and backward components are related by (2.3) the field can be expressed in terms of forward components only by defining

$$\begin{aligned} v_\nu(z) &= A_\nu e^{-j\beta_\nu z} + A_{-\nu} e^{j\beta_\nu z} \\ j_\nu(z) &= A_\nu e^{-j\beta_\nu z} - A_{-\nu} e^{j\beta_\nu z} \end{aligned} \tag{2.6}$$

Then we can write:

$$\begin{Bmatrix} \vec{E}_T(x, y, z) \\ \vec{H}_T(x, y, z) \end{Bmatrix} = \sum_\nu \begin{Bmatrix} v_\nu(z)\vec{e}_{T\nu}(x, y) \\ j_\nu(z)\vec{h}_{T\nu}(x, y) \end{Bmatrix} \tag{2.7}$$

$$\begin{Bmatrix} E_z(x, y, z) \\ H_z(x, y, z) \end{Bmatrix} = \sum_\nu \begin{Bmatrix} j_\nu(z)e_{z\nu}(x, y) \\ v_\nu(z)h_{z\nu}(x, y) \end{Bmatrix} \tag{2.8}$$

2.1.3 Orthogonality relations

The general orthogonality relation of the normal modes is in lossless waveguides is:

$$\frac{1}{2}\iint \vec{e}_\nu(x, y) \times \vec{h}_\mu{}^*(x, y) \cdot \hat{z}dxdy = \frac{1}{2}\iint \vec{e}_{T\nu}(x, y) \times \vec{h}_{T\mu}{}^*(x, y)dxdy = P_\nu \delta_{\nu\mu} \tag{2.9}$$

where P_ν is:

- purely real if β_ν is purely real and is the power carried by the mode.
- purely imaginary if β_ν is purely imaginary.

The power carried along the z-axis by an arbitrary field in a lossless waveguide is

$$P(z) = \frac{1}{2}Re\left\{\iint \vec{E}(x, y) \times \vec{H}^*(x, y) \cdot \hat{z}dxdy\right\} = \sum_\nu Re(P_\nu v_\nu j_\nu{}^*) \tag{2.10}$$

or

$$P(z) = \sum_{\nu,\ \text{free}} P_\nu(|A_\nu|^2 - |A_{-\nu}|^2) + \sum_{\nu,\ \text{evan}} P_\nu(A_{-\nu}A_\nu{}^* - A_{-\nu}{}^*A_\nu) \tag{2.11}$$

Every propagating mode plays its own part in the power independently of other modes. Power carried by evanescent modes couples ν with $-\nu$ modes but ν remains uncoupled from $\mu \neq \nu$.

2.1.4 Completeness of normal modes

In a bidirectional waveguide: Any two-component vector $\vec{V}_T(x, y)$ defined in the xy-plane can be written as a linear combination of the transverse electric and magnetic fields of the forward traveling modes as:

$$\vec{V}_T(x, y) = \sum_{\nu \in N} u_\nu \vec{e}_{T\nu}(x, y) \tag{2.12}$$

or

$$\vec{V}_T(x, y) = \sum_{\nu \in N} w_\nu \vec{h}_{T\nu}(x, y) \tag{2.13}$$

In contrast with expansion (2.5):

- z- dependence of normal modes does not appear in (2.12)-(2.13)
- there is no a priori relation between the waveguide and $\vec{V}_T(x, y)$
- only two components (x and y) are considered in (2.12)-(2.13)

These expansions are the basis of perturbation theories in systems that are close to an ideal waveguide. The starting point consists in using the normal modes of the ideal waveguide to represent the transverse components of the exact complete field through expansions like (2.7) with unknown $v_\nu(z), j_\nu(z)$. Note that (2.8) cannot be also exact unless the system is identical to the ideal waveguide.

Using the orthogonality conditions we can extract the modal amplitudes from the total field expansion of (2.12) (or (2.13)):

$$u_\nu = \frac{1}{2P_\nu} \iint \vec{V}_T(x, y) \times \vec{h}_\nu^*(x, y) \cdot \hat{z} dx dy \tag{2.14}$$

2.2 Excitation of modes by localized currents

The orthogonality relations can be used to derive the fields $\{\vec{E}, \vec{H}\}$ excited in an ideal waveguide by currents $\vec{J}, \vec{M}$ of finite extent as shown in the schematic [3]:

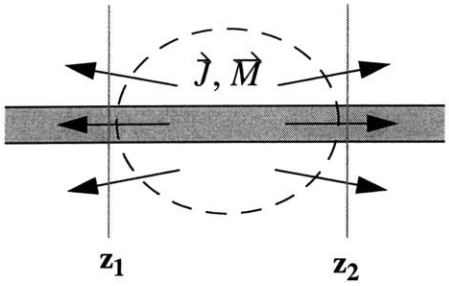

Figure 2.1: Schematic of a waveguide with localized current excitations.

Consider two different field distributions $\{\vec{E}_1, \vec{H}_1\}$ and $\{\vec{E}_2, \vec{H}_2\}$ excited by two different current distributions $\{\vec{J}_1, \vec{M}_1\}$ and $\{\vec{J}_2, \vec{M}_2\}$ at the same frequency and in the same material system. These two fields satisfy a reciprocity relationship:

$$\nabla \cdot (\vec{E}_1 \times \vec{H}_2 + \vec{H}_1 \times \vec{E}_2) = (\vec{J}_1 \cdot \vec{E}_2 - \vec{M}_1 \cdot \vec{H}_2) - (\vec{J}_2 \cdot \vec{E}_1 - \vec{M}_2 \cdot \vec{H}_1) \tag{2.15}$$

We replace $\{\vec{E}_1, \vec{H}_1\}$ with the unknown field $\{\vec{E}, \vec{H}\}$ excited by the currents $\vec{J}, \vec{M}$ and $\{\vec{E}_2, \vec{H}_2\}$ with the sourceless backward traveling mode $\{\vec{e}_{-v}(x, y), \vec{h}_{-v}(x, y)\}e^{j\beta_v z}$ and integrate (2.15) over x,y. The transverse part of ∇ leads to a contour integral at infinity:

$$\oint_{r \to \infty} [\vec{E} \times \vec{h}_{-v} + \vec{H} \times \vec{e}_{-v}] r d\theta \to 0$$

the the LHS of (2.15) reduces to

$$\frac{\partial}{\partial z} \iint (\vec{E} \times \vec{h}_{-v} + \vec{H} \times \vec{e}_{-v}) \cdot \hat{z} e^{j\beta_v z} dx dy \tag{2.16}$$

Since (2.16) depends only on transverse components we use the expansions (2.7) for $\{\vec{E}_T, \vec{H}_T\}$ based on the discussion on completeness in section 2.1.4. Due to the orthogonality relations (2.9) and the relations between the ν, $-\nu$, and ν^* modes, the double integral in (2.16) gives $-4A_\nu P_\nu$. Assuming that the modes are normalized to unit power we finally get:

$$\frac{dA_\nu}{dz} = -\frac{1}{4}\iint(\vec{J}\cdot\vec{e}_{-\nu} - \vec{M}\cdot\vec{h}_{-\nu})e^{j\beta_\nu z}dxdy \tag{2.17}$$

or

$$\frac{dA_\nu}{dz} = -\frac{1}{4}\iint(\vec{J}\cdot\vec{e}_\nu^{\,*} + \vec{M}\cdot\vec{h}_\nu^{\,*})e^{j\beta_\nu z}dxdy \tag{2.18}$$

By integration with respect to z we can find the amplitudes of the forward propagating modes.

Similarly for backward propagating modes we substitute $\{\vec{E}_2, \vec{H}_2\}$ with the sourceless forward traveling mode $\{\vec{e}_\nu(x, y), \vec{h}_\nu(x, y)\}e^{-j\beta_\nu z}$ and using the same relationships as before we get:

$$\frac{dA_{-\nu}}{dz} = \frac{1}{4}\iint(\vec{J}\cdot\vec{e}_\nu - \vec{M}\cdot\vec{h}_\nu)e^{-j\beta_\nu z}dxdy \tag{2.19}$$

In the following sections it will be convenient to use:

$$\begin{aligned} A_\nu &\equiv b_\nu(z)e^{j\beta_\nu z} \\ A_{-\nu} &\equiv b_{-\nu}(z)e^{-j\beta_\nu z} \end{aligned} \tag{2.20}$$

Knowing the forward amplitudes at z_1 and the backward amplitudes at z_2 we can find the amplitudes resulting from the interaction of the waveguide modes with the currents:

$$b_\nu(z_2) = e^{-j\beta_\nu(z_2-z_1)}\left(b_\nu(z_1) - \frac{1}{4}\int_{z_1}^{z_2} dz \iint dxdy(\vec{J}\cdot\vec{e}_\nu^{\,*} - \vec{M}\cdot\vec{h}_\nu^{\,*})e^{j\beta_\nu(z-z_1)}\right)$$
$$b_{-\nu}(z_1) = e^{-j\beta_\nu(z_2-z_1)}\left(b_{-\nu}(z_2) - \frac{1}{4}\int_{z_1}^{z_2} dz \iint dxdy(\vec{J}\cdot\vec{e}_{-\nu}^{\,*} - \vec{M}\cdot\vec{h}_{-\nu}^{\,*})e^{-j\beta_\nu(z-z_2)}\right) \quad (2.21)$$

With the procedure described above we have obtained the transverse components of the total field. The axial components are obtained from the axial part of Maxwell's equations.

$$\nabla_T(\hat{z}\times\vec{E}_T) = j\omega\mu H_z + M_z$$
$$\nabla_T(\hat{z}\times\vec{H}_T) = -j\omega e E_z - J_z \quad (2.22)$$

Using the source-free mode relations

$$\nabla_T(\hat{z}\times\vec{e}_\nu) = j\omega\mu h_{\nu z}$$
$$\nabla_T(\hat{z}\times\vec{h}_\nu) = -j\omega\varepsilon e_{\nu z} \quad (2.23)$$

we finally get:

$$E_z = \sum_{\nu\in N} j_\nu(z)e_{z\nu}(x,y) - \frac{J_z}{j\omega\varepsilon}$$
$$H_z = \sum_{\nu\in N} v_\nu(z)h_{z\nu}(x,y) - \frac{M_z}{j\omega\mu} \quad (2.24)$$

2.3 Scattering matrices

The scattering matrix formalism comes from microwave engineering where it is a fundamental tool for characterizing microwave circuits. It can be extended to optical systems in spite of some difficulties due to radiating modes.

We consider systems like the one shown in the schematic of Figure 2.2 and follow the analysis of [3].

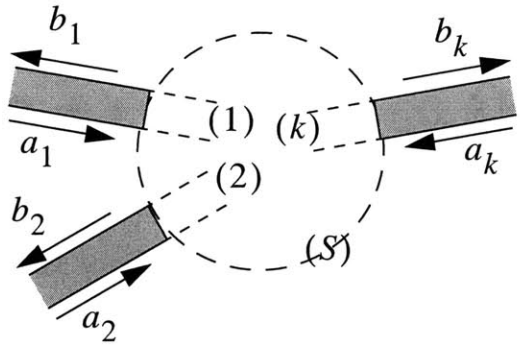

Figure 2.2: Schematic of a multi-port optical system.

The optical system which is assumed passive, is viewed as a black box enclosed inside a surface S. Energy with the outside world is exchanged through several ports that can be optical waveguides or free space beams. The S-matrix theory is based on the following assumptions:

• Every outlet has its own propagation axis and the electromagnetic fields are well confined around these axes, so that effective outlets can be defined outside which the fields are negligible. Physical ports correspond to the intersections of S and the effective outlets.

• The field is negligible everywhere on S outside the ports.

• The outlets are lossless waveguides

• There is no evanescent mode in the ports.

In a given port (k), the transverse field can be given a modal expansion. Assuming that the propagation axis points toward the optical system we can write

$$\begin{aligned} \vec{E}_T(x, y) &= \sum_{\nu \in N(k)} (a_{k\nu} + b_{k\nu}) \vec{e}_{T,k\nu}(x, y) \\ \vec{H}_T(x, y) &= \sum_{\nu \in N(k)} (a_{k\nu} - b_{k\nu}) \vec{h}_{T,k\nu}(x, y) \end{aligned} \tag{2.25}$$

where x, y are the local coordinates, $a_{k\nu}, b_{k\nu}$ are the input and output waves, respectively for the mode ν and $N(k)$ is the set of input modes for this port. The expansions

(2.12),(2.13) are valid only for port k but they can be extended to the whole surface S with the definition:

$$\text{generalized modal field } \mu = \begin{cases} \text{original field } \nu, \text{ within port } k \\ 0 \text{ anywhere else} \end{cases}$$

We can now use the total mode expansion valid throughout S.

$$\begin{aligned} \vec{E}_T &= \sum_{\mu \in M} (a_\mu + b_\mu)\vec{e}_{T,\mu} \\ \vec{H}_T &= \sum_{\mu \in M} (a_\mu - b_\mu)\vec{h}_{T,\mu} \end{aligned} \tag{2.26}$$

where $M = \cup N(k)$ and an extended orthogonality relation:

$$\iint_S \vec{e}_\mu \times \vec{h}_{\mu'}{}^* \cdot \hat{n} dS = 2\delta_{\mu\mu'} \tag{2.27}$$

This relation is valid only for fields on S that are zero outside the ports, $\hat{n}$ is the inward pointing normal and the modes are assumed to be normalized to unit power. If the transverse fields are real then (2.27) holds with $\vec{h}_\mu$ instead of $\vec{h}_\mu{}^*$. The total power absorbed in the system is given by:

$$P = \sum_\mu (|a_\mu|^2 - |b_\mu|^2) = (\bar{\underline{A}}^* \bar{\underline{A}} - \bar{\underline{B}}^* \bar{\underline{B}}) \tag{2.28}$$

where $\bar{\underline{A}}$, $\bar{\underline{B}}$ are the column matrices of the a_μ's and b_μ's are related through the scattering matrix $\bar{\underline{S}}$ as:

$$\bar{\underline{B}} = \bar{\underline{S}} \cdot \bar{\underline{A}} \tag{2.29}$$

If all the elements of $\bar{\underline{A}}$ are zero except some input a_ν, the output waves are given by the ν-th column of $\bar{\underline{S}}$. Then the diagonal term $S_{\nu\nu}$ is the reflection coefficient of the mode ν and the non-diagonal terms $S_{\mu\nu}$ are the transmission coefficients from the mode ν to the mode μ. If the total fields $\vec{E}_T$, $\vec{H}_T$ on S are known, we can use the orthogonality

conditions to obtain $v_\nu = a_\nu + b_\nu$, $j_\nu = a_\nu - b_\nu$ and $v_\mu = a_\mu + b_\mu$, $j_\mu = a_\mu - b_\mu$. Then $S_{\nu\nu}$ and $S_{\mu\nu}$ are given by:

$$S_{\nu\nu} = \frac{v_\nu - j_\nu}{v_\nu + j_\nu} \qquad S_{\mu\nu} = \frac{v_\mu - j_\mu}{v_\nu + j_\nu} \tag{2.30}$$

Some important properties of the scattering matrix are given below:

• If the reference input/output planes at the ports are displaced and l_μ is the displacement associated to the mode (μ), it can be shown that the new scattering matrix $\underline{\bar{S}}'$ is given by:

$$\underline{\bar{S}}' = \underline{\bar{X}}^{-1} \cdot \underline{\bar{S}} \cdot \underline{\bar{X}}^{-1} \quad \text{or} \quad S'_{\mu\nu} = S_{\mu\nu} e^{-j(\beta_\mu l_\mu + \beta_\nu l_\nu)} \tag{2.31}$$

where $\underline{\bar{X}}$ is the diagonal matrix with elements $e^{-j\beta_\mu l_\mu}$.

• A linear, reciprocal system has a symmetric scattering matrix:

$$\underline{\bar{S}}^{\mathrm{T}} = \underline{\bar{S}} \quad \text{or} \quad S_{\mu\nu} = S_{\nu\mu} \tag{2.32}$$

• If the system is lossless its scattering matrix is unitary:

$$\underline{\bar{S}}^{\dagger}\underline{\bar{S}} = \bar{I} \quad \text{or} \quad \sum_{\nu} |S_{\mu\nu}|^2 = 1 \tag{2.33}$$

where $\underline{\bar{S}}^{\dagger} = \underline{\bar{S}}^{*\mathrm{T}}$.

The theory presented here will be useful in the calculation of the coupling efficiency between fundamental fiber and waveguide modes obtained by different fiber-chip coupling schemes in Chapter 6.

2.4 Effective index method

Because in most cases it is cumbersome to apply the above theory or preform numerical simulations using the full-vector modes of 3D waveguide-based structures it might be preferable to perform the analysis in two dimensions using an effective 2D model derived from the real 3D structure. An approximate method which appears in many variations and is widely used as a starting point for 2D numerical simulations, is the Effective Index

Method (EIM). Its origin is in [30] where the analysis of slab waveguides is extended to channel waveguides with 3D field solutions that are the products of solutions of two independent slab waveguides. This leads to a set of transcendental equation for the transverse propagation constants k_x, k_y and the propagation constant is $\beta^2 = k_o^2 n_i^2 - k_x - k_y$. This analysis was modified in [31] by assigning the effective index $n_e^2 = n_i^2 - (k_x/k_o)^2$ to the wider of the two slabs (referring to Figure 2.3). Both analyses yield reliable results well above cutoff and for large aspect ratios but have large discrepancies from the exact solutions near cutoff. We present its simplest forms here. Two waveguide systems often encountered are shown: in Figure 2.3(a) and (b) and the equivalent 2D system in (c).

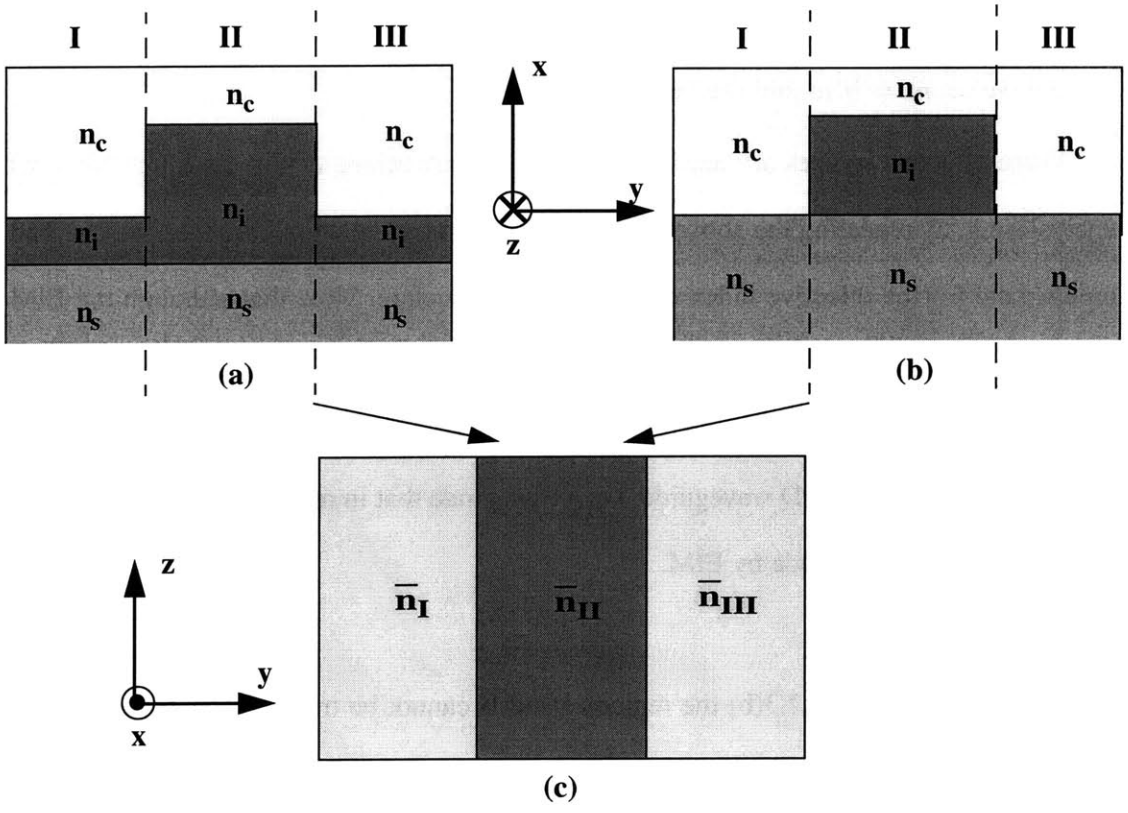

Figure 2.3: Schematic of (a) a rib waveguide (b) a ridge waveguide (c) 2D system resulting from effective index method.

Case (a)

In this case we simply treat each of the regions I,II,II as a slab waveguide and find the effective indices $\bar{n}_I$, $\bar{n}_{II}$, $\bar{n}_{III}$, respectively from the transverse resonance condition.

$$k_o d\sqrt{n_i^2 - n_e^2} = \text{atan}\left(r_s \frac{\sqrt{n_e^2 - n_s^2}}{\sqrt{n_i^2 - n_e^2}} \right) + \text{atan}\left(r_c \frac{\sqrt{n_e^2 - n_c^2}}{\sqrt{n_i^2 - n_e^2}} \right) + m\pi \tag{2.34}$$

where $n_e = \bar{n}_I$, $\bar{n}_{II}$, $\bar{n}_{III}$, $k_o = 2\pi/\lambda$, d is the thickness of the slab waveguide in each region and:

$$r_{s,c} = \begin{cases} 1 & \text{for TE modes} \\ \left(\dfrac{n_{s,c}}{n_i} \right)^2 & \text{for TM modes} \end{cases} \tag{2.35}$$

and we set $m = 0$ to find the fundamental mode.

These effective indices are used in the equivalent structure of Figure 2.3(c) for a 2D analysis, e.g. by repeating the above procedure for the orthogonal polarization we can find an estimate for the effective index of the total 3D structure. Note that although the EIM may can give a good estimate of the effective index, especially for large aspect ratios, it tends break down near cutoff. It also often leads to wrong conclusions about the number of modes supported by the 3D waveguide, i.e. a waveguide that in reality is single-mode may be found to be double-mode by EIM.

Case (b)

In the case of Figure 2.3(b) the regions I and II cannot be treated as slab waveguides and we use a perturbation approach which is also applicable in case (a). We start from finding the effective index for the slab waveguide of region II $\bar{n}_{II}$ from (2.34), and the associated fundamental mode profile, and then use perturbation theory to find the effective indices in regions I and II [7].

If we know the mode profile $\varphi(x)$ and propagation constant β of a waveguide structure with index distribution $n(x)$ then we can find the change $\Delta\beta$ of the propagation constant of a slightly modified distribution $n^2(x) + \Delta n^2(x)$ by assuming that $\varphi(x)$ is unchanged. The scalar wave equation satisfied by $\varphi(x)$ is:

$$\nabla^2\varphi + [k_o^2(n^2 + \Delta n^2) - (\beta + \Delta\beta)^2]\varphi = 0 \tag{2.36}$$

where $k_o = 2\pi/\lambda$ and $\beta = k_o n_e$.

To first order we can write $(\beta + \Delta\beta)^2 = \beta^2 + 2\beta\Delta\beta$ and we use the fact that $\varphi(x)$ is the exact solution of

$$\nabla^2\varphi + [k_o^2 n^2 - \beta^2]\varphi = 0 \tag{2.37}$$

so (2.36) becomes:

$$[k_o^2\Delta n^2 - 2\beta\Delta\beta]\varphi = 0 \tag{2.38}$$

We now multiply (2.38) by φ^* and integrate over x to get:

$$\Delta n_e = \frac{\int \Delta n^2 |\varphi|^2 dx}{2n_e \int |\varphi|^2 dx} \tag{2.39}$$

Equation (2.39) is applied in region (I) with $n_e = \bar{n}_{II}$, $\phi(x) = \phi_{II}(x)$ and $\Delta n^2(x) = n_I^2(x) - n_{II}^2(x)$ to give $\Delta n_e = \Delta\bar{n}_I$ and in region (II) with $n_e = \bar{n}_{II}$, $\phi(x) = \phi_{II}(x)$ and $\Delta n^2(x) = n_{III}^2(x) - n_{II}^2(x)$ to give $\Delta n_e = \Delta\bar{n}_{II}$

Then $\bar{n}_I = n_I + \Delta\bar{n}_I$ and $\bar{n}_{II} = n_{II} + \Delta\bar{n}_{II}$.

Note that this method can also be applied in case (a) giving slightly more accurate results. In this work the equivalent 2D structure resulting from EIM will be used as input in 2D FDTD simulations of 3D guided wave structures.

2.5 Resonators

Most of the waveguide devices discussed in this work are based on resonant cavities. Resonance is a general physical phenomenon that takes many forms, one of the most familiar being in circuit theory, e.g. LC circuits. The basic characteristic is the buildup of energy in the resonator due to the excitation of one or more resonant modes and the gradual dissipation of this energy due to loss and/or coupling with input/output ports. In the case of integrated optics the loss is due to radiation or material absorption and the input/output ports are optical waveguides directly or evanescently coupled to the cavity. We use the coupling of modes in time approach presented in [6] to describe the evolution of the resonant mode amplitude a. The squared magnitude of this amplitude is equal to the energy stored in the resonant cavity:

$$|a|^2 = W \tag{2.40}$$

In the absence of any external excitation, the mode in the cavity decays exponentially with a finite lifetime τ due to various mechanisms of power dissipation such as material loss, radiation, coupling to waveguides etc. The basic equation is:

$$\frac{da}{dt} = \left(j\omega_o - \frac{1}{\tau}\right)a \tag{2.41}$$

where ω_o is the resonant frequency and $1/\tau = \sum(1/\tau_i)$ is the sum of all decay rates $1/\tau_i$.

The rate of change of the energy in the cavity is equal to the dissipated power. From (2.40) and (2.41) we have:

$$\frac{dW}{dt} = \frac{d|a|^2}{dt} = -\frac{2}{\tau}W = -P_d \tag{2.42}$$

The quality factor Q of the resonator is given by:

$$\frac{1}{Q} = \frac{P_d}{\omega_o W} = \frac{2}{\omega_o \tau} \tag{2.43}$$

and is related to the spectral full half maximum width $\Delta\omega_{1/2}$ by:

$$\frac{1}{Q} = \frac{\Delta\omega_{1/2}}{\omega_o} \tag{2.44}$$

2.5.1 Coupled resonators

We use the same formalism to describe the coupling of two resonators which, for simplicity are assumed lossless.

$$\begin{aligned} \frac{da_1}{dt} &= j\omega_1 a_1 + \mu_{12} a_2 \\ \frac{da_2}{dt} &= j\omega_2 a_2 + \mu_{21} a_1 \end{aligned} \tag{2.45}$$

where $a_i, \omega_i, \quad i = 1, 2$ are the mode amplitudes and resonant frequencies, respectively, and μ_{12}, μ_{21} are the coupling coefficients which can be found by energy conservation arguments in [6]. The rate of change of the total energy must be zero:

$$\frac{d}{dt}(|a_1|^2 + |a_2|^2) = a_1^* \mu_{12} a_2 + a_1(\mu_{12} a_2)^* + a_2^* \mu_{21} a_1 + a_2(\mu_{21} a_1)^* = 0 \tag{2.46}$$

This relation must hold for all a_1, a_2, thus:

$$\mu_{12} = -\mu_{21}^* = -j\mu \tag{2.47}$$

If the resonators are identical ($\omega_1 = \omega_2 = \omega_o$) it is easy to show that the total system has two eigenmodes with even and odd symmetry, $a_{s,a} = a_1 \pm a_2$, respectively and the resonant frequency is split into two frequencies $\omega_{s,a} = \omega \mp \mu$.

2.5.2 Resonator-waveguide coupling

The use of a resonator as part of an optical system involves coupling with waveguides and interaction of the resonant and waveguide modes.

Evanescent coupling

In evanescent coupling the resonator mode is excited by the mode field of a side coupled waveguide as shown in the schematic of Figure 2.4. Our analysis is based on the theory presented in Section 2.2 in combination with the theory in [34]. A modified version appears in [47].

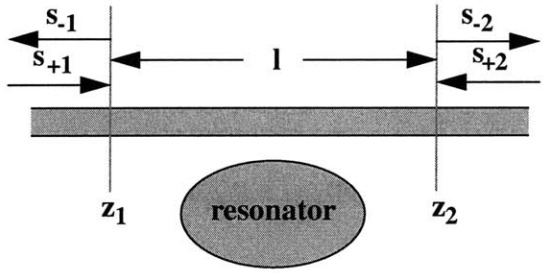

Figure 2.4: Schematic of a resonator evanescently coupled to a waveguide

In general, the resonator modes interact with the forward and backward propagating modes of the waveguide over a finite length along which the fields of the resonator modes overlap with the waveguide fields. The interaction region is assumed to be fully contained between the input/output reference planes, defined on either side of the resonator, as shown in Figure 2.4. For simplicity we consider a resonator and a waveguide each supports only one mode in the frequency range of interest. The resonator mode amplitude is denoted by a and $|a|^2$ is equal to the energy in the mode. The unperturbed resonator mode field is denoted by $\grave{e}_r(x, y, z)$ normalized to unit energy. The amplitudes of the incoming (outgoing) waves at the waveguide are denoted by $s_{+1}(s_{-1})$ and $s_{+2}(s_{-2})$, respectively and $|s_{\pm(1,2)}|^2$ is the power carried by the waveguide modes. For simpler notation the subscripts $\nu, -\nu$ of the waveguide modes are omitted. The fields of the unperturbed forward and backward traveling waveguide mode are $\{\grave{e}_+(x, y), \grave{h}_+(x, y)\}$ and

$\{\vec{e}_-(x,y), \vec{h}_-(x,y)\} = \{\vec{e}^*(x,y), -\vec{h}^*(x,y)\}$, respectively, normalized to unit power. The influence of the coupling along the interaction length is expressed by the z-varying amplitudes $b_\pm(z) = A_\pm e^{\mp j\beta z}$ which satisfy:

$$\begin{aligned} b_\pm(z_1) &= s_{\pm 1} \\ b_\pm(z_2) &= s_{\mp 2} \end{aligned} \tag{2.48}$$

We can readily use (2.21) with $\vec{J} = j\omega\varepsilon_o(n^2(x,y,z) - n_r^{\,2}(x,y,z))a(\omega)\vec{e}_r(x,y,z)$ and $\vec{M} = 0$ where $n(x,y,z), n_r(x,y,z)$ are the index distributions of the total system and the resonator respectively and $\vec{J}$ is the polarization current excited in the waveguide by the resonator mode. We get:

$$s_{-2} = e^{-j\beta(z_2-z_1)}\left(s_{+1} - j\frac{\omega\varepsilon_o}{4}\int_{z_1}^{z_2} dz \iint dxdy(n^2 - n_r^2)\vec{e}_r \cdot \vec{e}_-\, e^{j\beta(z-z_1)} a\right) \tag{2.49}$$

$$s_{-1} = e^{-j\beta(z_2-z_1)}\left(s_{+2} - j\frac{\omega\varepsilon_o}{4}\int_{z_1}^{z_2} dz \iint dxdy(n^2 - n_r^2)\vec{e}_r \cdot \vec{e}_+\, e^{-j\beta(z-z_2)} a\right) \tag{2.50}$$

The evolution of the resonator mode in time is given by:

$$\frac{da}{dt} = \left(j\omega_o - \frac{1}{\tau_o} - \frac{1}{\tau_e}\right)a + \kappa_1 s_{+1} + \kappa_2 s_{+2} \tag{2.51}$$

where ω_o is the resonant frequency, $1/\tau_o$ is the decay rate due to loss, $1/\tau_e$ is the decay rate into the waveguide mode and κ_1, κ_2 are the input coupling coefficients associated with the forward and backward propagating modes in the bus.The input coupling coefficients $\kappa_{1,2}$ can be found by power conservation. Neglecting the loss the rate of change of the energy in the resonator mode must be equal to the difference between the incoming and outgoing power:

$$\frac{d|a|^2}{dt} = |s_{+1}|^2 + |s_{+2}|^2 - |s_{-1}|^2 - |s_{-2}|^2 \tag{2.52}$$

From (2.51) we have:

$$\frac{d|a|^2}{dt} = -\frac{2}{\tau_e}|a|^2 + \kappa_1 s_{+1} a^* + c.c. + \kappa_2 s_{+2} a^* + c.c. \tag{2.53}$$

Substituting (2.49)-(2.50) into (2.52) and comparing with (2.53) we find:

$$\kappa_1 = -j\frac{\omega\varepsilon_o}{4}\int_{z_1}^{z_2} dz \iint dxdy(n^2 - n_r^2)\hat{e}_r^* \cdot \hat{e}_- \, {}^* e^{-j\beta(z-z_1)} \tag{2.54}$$

$$\kappa_2 = -j\frac{\omega\varepsilon_o}{4}\int_{z_1}^{z_2} dz \iint dxdy(n^2 - n_r^2)\hat{e}_r^* \cdot \hat{e}_+ \, {}^* e^{j\beta(z-z_2)} \tag{2.55}$$

$$|\kappa_1|^2 + |\kappa_2|^2 = \frac{2}{\tau_e} \tag{2.56}$$

Setting $z_2 - z_1 = l$, the outgoing waves can now be written as:

$$\begin{aligned} s_{-1} &= e^{-j\beta l}(s_{+2} - \kappa_2^* a) \\ s_{-2} &= e^{-j\beta l}(s_{+1} - \kappa_1^* a) \end{aligned} \tag{2.57}$$

Equations (2.57) show that in the absence of the resonator the waveguide mode propagates undisturbed with a phase delay due to the finite length l.

If the excitation is $s_{+1} \sim e^{j\omega t}$, $s_{+2} = 0$, then at steady state we get from (2.51):

$$a = \frac{\kappa_1 s_{+1}}{j(\omega - \omega_o) + \frac{1}{\tau_o} + \frac{1}{\tau_e}} \tag{2.58}$$

and (2.57) become:

$$\begin{aligned} s_{-1} &= -e^{-j\beta l}\frac{\kappa_2^* \kappa_1}{j(\omega - \omega_o) + \frac{1}{\tau_o} + \frac{1}{\tau_e}} s_{+1} \\ s_{-2} &= e^{-j\beta l}\left(1 - \frac{|\kappa_1|^2}{j(\omega - \omega_o) + \frac{1}{\tau_o} + \frac{1}{\tau_e}}\right) s_{+1} \end{aligned} \tag{2.59}$$

The above analysis can be generalized for the case of a resonant structure supporting $M \geq 1$ modes, evanescently coupled to $N \geq 1$ waveguides:

$$\frac{da_m}{dt} = \left(j\omega_{om} - \frac{1}{\tau_{om}} - \sum_n \frac{1}{\tau_{emn}}\right)a_m + \sum_n \kappa_{m,(2n-1)} s_{+(2n-1)} + \kappa_{m,2n} s_{+2n} \tag{2.60}$$

$$\begin{aligned} s_{-(2n-1)} &= e^{-j\beta_n l_n}\left(s_{+2n} - \sum_m \kappa^*_{m,2n} a_m\right) \\ s_{-2n} &= e^{-j\beta_n l_n}\left(s_{+(2n-1)} - \sum_m \kappa^*_{m,(2n-1)} a_m\right) \end{aligned} \tag{2.61}$$

$$\left|\kappa_{m,(2n-1)}\right|^2 + \left|\kappa_{m,2n}\right|^2 = \frac{2}{\tau_{emn}} \tag{2.62}$$

where $m = 1, \ldots, M$ counts the resonator modes and $n = 1, \ldots, N$ the waveguides. $\kappa_{m,(2n-1)}$, ($\kappa_{m,2n}$) express the coupling between the mth resonator mode and forward (backward) propagating mode in the nth waveguide and $\frac{1}{\tau_{emn}}$ is the decay rate of the mth resonator into the nth waveguide. The results of this analysis will be useful for the study of the resonant channel dropping filters in Chapter 4.

Direct coupling

The simplest case is shown in the schematic. The resonator is enclosed in a surface S that intersects the input waveguide at $z = z_2$ and we make the assumptions of section 2.3 for the field distributions. In general the input/output reference plane can chosen at any $z = z_1 \leq z_2$. The method of Section 2.2 can be applied again in combination with the theory of [6]. This time the excitations are the surface currents at $z = z_2$ produced by the resonator fields tangential to that plane whereas the fields inside S are taken zero:

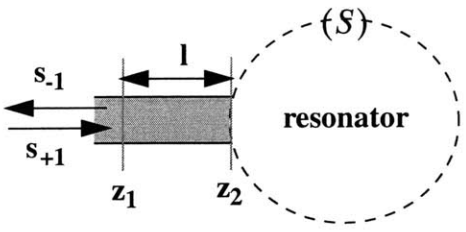

Figure 2.5: Schematic of a resonator directly coupled to a waveguide.

$$\begin{aligned} \vec{J} &= -\hat{z} \times \vec{h}_r(x, y, z)\delta(z_2)a \\ \vec{M} &= \hat{z} \times \vec{e}_r(x, y, z)\delta(z_2)a \end{aligned} \tag{2.63}$$

In this case the boundary conditions are:

$$\begin{aligned} b_{\pm}(z_1) &= s_{\pm 1} \\ b_{-}(z_2) &= -b_{+}(z_2) \end{aligned} \tag{2.64}$$

$$b_{+}(z_2) = e^{-j\beta(z_2 - z_1)}\left(s_{+1} - \frac{1}{4}\iint dxdy(-\hat{z} \times \vec{h}_r \cdot \vec{e}_{-} - \hat{z} \times \vec{e}_r \cdot \vec{h}_{-})e^{j\beta(z_2 - z_1)}a\right) \tag{2.65}$$

$$s_{-1} = e^{-j\beta(z_2 - z_1)}\left(b_{-}(z_2) - \frac{1}{4}\iint dxdy(-\hat{z} \times \vec{h}_r \cdot \vec{e}_{+} - \hat{z} \times \vec{e}_r \cdot \vec{h}_{+})a\right) \tag{2.66}$$

Combining (2.65) and (2.66)and using the second of (2.64) we get:

$$s_{-1} = -e^{-j2\beta(z_2 - z_1)}\left(-s_{+1} + \frac{1}{4}\iint dxdy(\hat{z} \times \vec{e}_r) \cdot (\vec{h}_{+} - \vec{h}_{-})e^{j\beta(z_2 - z_1)}a\right) \tag{2.67}$$

or, using (2.4) and the fact that $\vec{h}_T = \vec{h}_T^{\,*}$, $h_z = -h_z^{\,*}$ as well as the vector identity $(\vec{a} \times \vec{b}) \cdot \vec{c} = (\vec{b} \times \vec{c}) \cdot \vec{a}$ we get:

$$s_{-1} = -e^{-j2\beta(z_2 - z_1)}\left(-s_{+1} + \frac{1}{2}\iint dxdy\vec{e}_r \times \vec{h}_{T+} \cdot \hat{z}e^{j\beta(z_2 - z_1)}a\right) \tag{2.68}$$

The same result is obtained if we expand the fields on the left of $z = z_2$ in terms of the waveguide modes and on the right in terms of the resonator modes and apply the orthogonality conditions for the waveguide modes to the continuity condition for the tangential electric fields at $z = z_2$.

The evolution of the resonator mode is given by:

$$\frac{da}{dt} = \left(j\omega_o - \frac{1}{\tau_o} - \frac{1}{\tau_e}\right)a + \kappa_1 s_{+1} \tag{2.69}$$

and the rate of change of the energy is:

$$\frac{d|a|^2}{dt} = |s_{+1}|^2 - |s_{-1}|^2 \tag{2.70}$$

Or:

$$\frac{d|a|^2}{dt} = -\frac{2}{\tau_e}|a|^2 + \kappa_1 s_{+1} a^* + c.c. \tag{2.71}$$

Substituting (2.68) into (2.70) and comparing with (2.71) we get:

$$\kappa_1 = \frac{1}{2}\iint dxdy \hat{e}_r^* \times \hat{h}_{T+}^* \cdot \hat{z} e^{-j\beta(z_2 - z_1)} a \tag{2.72}$$

$$|\kappa_1|^2 = \frac{2}{\tau_e} \tag{2.73}$$

Setting $z_2 - z_1 = l$, the outgoing waves can now be written as:

$$s_{-1} = e^{-j2\beta l}(-s_{+1} + \kappa_1^* a) \tag{2.74}$$

Equation (2.74) shows that the absence of the resonator is equivalent to a short that results in complete reflection of the input with a phase delay due to the finite length l.

If $s_{+1} \sim e^{j\omega t}$ then, using (2.69) at steady state, we get:

$$a = \frac{\kappa_1 s_{+1}}{j(\omega - \omega_o) + \frac{1}{\tau_o} + \frac{1}{\tau_e}} \tag{2.75}$$

And (2.74) becomes:

$$s_{-1} = -e^{-j2\beta l}\left(1 - \frac{|\kappa_1|^2}{j(\omega - \omega_o) + \frac{1}{\tau_o} + \frac{1}{\tau_e}}\right) s_{+1} \tag{2.76}$$

The above analysis can be generalized for $M \geq 1$ modes excited in the resonator and for $N \geq 1$ ports, with the following relationships:

$$\frac{da_m}{dt} = \left(j\omega_{om} - \frac{1}{\tau_{om}} - \sum_n \frac{1}{\tau_{emn}}\right) a_m + \sum_n \kappa_{mn} s_{+n} \tag{2.77}$$

$$s_{-n} = e^{-j2\beta_n l_n}\left(-s_{+n} + \sum_m \kappa_{mn}^* a_m\right) \tag{2.78}$$

$$|\kappa_{mn}|^2 = \frac{1}{\tau_{emn}} \tag{2.79}$$

where $m = 1, \ldots, M$ counts the resonator modes and $n = 1, \ldots, N$ the waveguides. κ_{mn} is the coupling between the mth resonator mode and the nth waveguide mode and $\frac{1}{\tau_{emn}}$ is the associated external decay rate.

The results of this analysis will be useful for the study of the low-loss waveguide components in Chapter 5.

2.6 Gaussian beams

Free-space propagation and wave guiding problems can be simplified if we approximate the spatial dependence for the fields by Gaussian functions. The theory presented in this section will be useful in the analytical study of fiber-chip couplers.

2.6.1 Propagation of Gaussian beams

Gaussian beams are the exact solutions of the paraxial equation in media with refractive

index profile of the form:

$$n^2(x, y) = n_o^2\left(1 - \frac{x^2}{h_x^2} - \frac{y^2}{h_y^2}\right) \tag{2.80}$$

The case of free space of index n_o is covered by $h_x = h_y = \infty$. We follow the analysis of [4].

From Maxwell's equations for time harmonic fields we get

$$\nabla^2\vec{E} + \omega^2\mu_o\varepsilon_o n^2\vec{E} = -\nabla\left(\frac{1}{n^2}\vec{E}\cdot\nabla n^2\right) \tag{2.81}$$

(2.82)

We assume that $\frac{\nabla n^2}{n^2} << 1$ over a wavelength and factor out the fast z-variation by setting $\vec{E} = \hat{x}\psi(x, y, z)e^{-jkz}$ where $k = k_o n_o$, $k_o = \omega\sqrt{\mu_o\varepsilon_o}$. Then (2.81) becomes:

$$\frac{\partial^2\psi}{\partial x^2} + \frac{\partial^2\psi}{\partial y^2} + \frac{\partial^2\psi}{\partial z^2} + k^2\left(1 - \frac{x^2}{h_x^2} - \frac{y^2}{h_y^2}\right)\psi = 0 \tag{2.83}$$

In the paraxial approximation

$$\frac{\partial^2\psi}{\partial z^2} << k\frac{\partial\psi}{\partial z}, k^2\psi$$

so (2.83) becomes:

$$\frac{\partial^2\psi}{\partial x^2} + \frac{\partial^2\psi}{\partial y^2} - j2k\frac{\partial\psi}{\partial z} + k^2\left(1 - \frac{x^2}{h_x^2} - \frac{y^2}{h_y^2}\right)\psi = 0 \tag{2.84}$$

Substituting into (2.84) the trial solution:

$$\psi(x, y, z) = \exp\left\{-j\left[P(z) + \frac{kx^2}{2q_x(z)} + \frac{ky^2}{2q_y(z)}\right]\right\} \tag{2.85}$$

with initial conditions $q_x(z_x) = q_{ox}$, $q_y(z_y) = q_{oy}$ we find, as shown in [4]:

$$P = -\frac{j}{2}\left[\ln\left(\frac{q_x(z)}{q_{ox}}\right) + \ln\left(\frac{q_y(z)}{q_{oy}}\right)\right] \tag{2.86}$$

and

$$q_{x,y}(z) = \frac{q_{o(x,y)}\cos[(z-z_{x,y})/h_{x,y}] + h_{x,y}\sin[(z-z_{x,y})/h_{x,y}]}{-(q_{o(x,y)}/h_{x,y})\sin[(z-z_{x,y})/h_{x,y}] + \cos[(z-z_{x,y})/h_{x,y}]} \tag{2.87}$$

The real and imaginary parts of $1/q_{x,y}(z)$ give the radii R_x, R_y and beam waists w_x, w_y, respectively in the x,y directions:

$$\frac{1}{q_{x,y}(z)} = \frac{1}{R_{x,y}(z)} - j\frac{2}{kw^2_{x,y}(z)} \tag{2.88}$$

Knowing how the q-parameters of the gaussian beam evolve during propagation we can trace the evolution of the phase front curvature and the beam waist.

If the initial beam widths and q-parameters are:

$$\tilde{w}_{o(x,y)} = \sqrt{\frac{2h_{x,y}}{k}} \qquad \tilde{q}_{o(x,y)} = -j\frac{kw^2_{o(x,y)}}{2} = -jh_{x,y} \tag{2.89}$$

which correspond to the eigenmode of (2.83) then the beam propagates through the medium maintaining its width and plain wave fronts. Otherwise, when $w_{o(x,y)} \neq \tilde{w}_{o(x,y)}$ the widths in x- and y- directions vary periodically with z as: ([5])

$$w^2(z) = w^2_{o(x,y)}\cos^2\left(\frac{z}{h_{x,y}}\right)\left\{1 + \left(\frac{\tilde{w}_{o(x,y)}}{w_{o(x,y)}}\right)^4 \tan^2\left(\frac{z}{h_{x,y}}\right)\right\} \tag{2.90}$$

with oscillation periods $h_{x,y}/2$

In a uniform medium $h_x = h_y = \infty$ and from (2.87) we find:

$$q_{x,y}(z) = q_{o(x,y)} + z \tag{2.91}$$

$$w_{x,y}{}^2(z) = w^2_{o(x,y)}\left(1 + \frac{z^2}{z^2_{o(x,y)}}\right) \qquad R_{x,y}(z) = z\left(1 + \frac{z^2_{o(x,y)}}{z^2}\right) \tag{2.92}$$

where $z_{o(x,y)} = kw^2_{o(x,y)}/2$ and w_o is the minimum waist. These relations show that as a gaussian beam propagates in free space it spreads out curving its phase fronts.

In a dielectric structure with cylindrical symmetry $h_x = h_y$ the gaussian beam has cylindrical symmetry as well and is described by one q-parameter $q_x = q_y = q$ and $R_x = R_y = R$, $w_x = w_y = w$.

Restoring the e^{-jkz} dependence in (2.85) we can obtain the propagation constant and effective index: ([5])

$$\beta = k - \frac{1}{kw_x^2} - \frac{1}{kw_y^2} \quad \text{and} \quad n_e = n_o\left[1 - \frac{1}{(k_o n_o w_x)^2} - \frac{1}{(k_o n_o w_y)^2}\right] \tag{2.93}$$

It is interesting to note that the variational method with gaussian trial functions presented in 2.6.3 results in the correct answer for the effective index and the beam width only for the eigenmode of a quadratic medium.

2.6.2 ABCD matrices

In the previous analysis the evolution of the q-parameter of a gaussian beam as it propagates through a medium is in general given by a transformation of the form

$$q_2 = \frac{Aq_1 + B}{Cq_1 + D} \tag{2.94}$$

where A, B, C, D are the elements of the matrix describing the behavior of a ray through an optical system as:

$$\begin{bmatrix} r_2 \\ r_2' \end{bmatrix} = \begin{bmatrix} A & B \\ C & D \end{bmatrix} \begin{bmatrix} r_1 \\ r_1' \end{bmatrix} \tag{2.95}$$

where r_i is the distance of the ray in medium $i = 1, 2$ from the z-axis and r_i' its slope.

The advantage of the ABCD formalism is that a cascade of different elements can is simply described by the product of the individual ABCD matrices. It is also easy to follow the evolution of the q-parameter and therefore of the beam waist and phase front as the beam propagates through different stages of the cascade. For elliptical Gaussian beams $q_x \neq q_y$ and the ABCD matrices are used separately in the x and the y direction to describe the evolution of the two q-parameters. The ABCD matrices for basic optical elements that serve as building blocks for common optical systems are shown below ([4]):

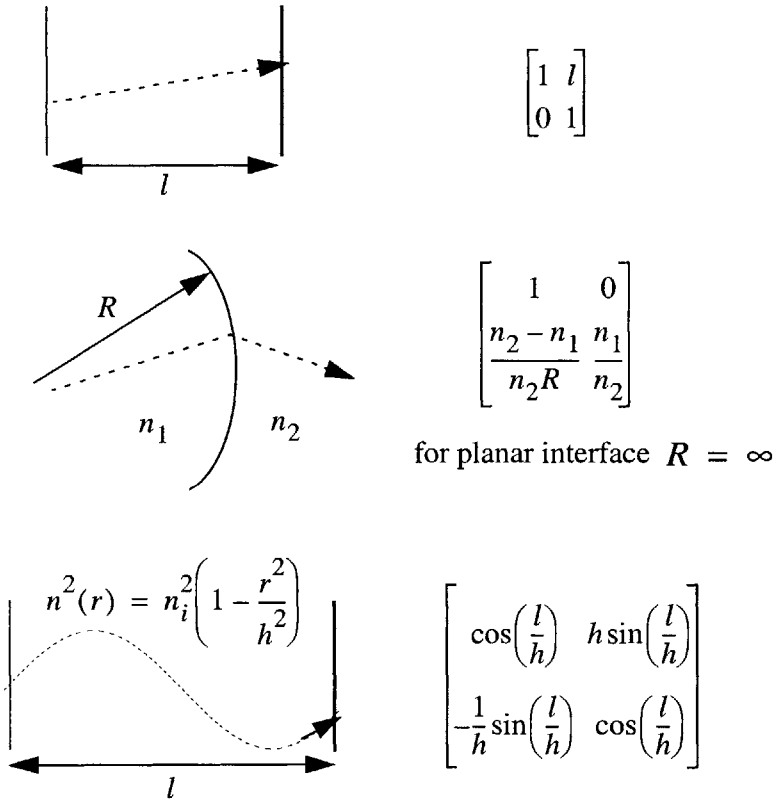

Figure 2.6: ABCD matrices for basic elements (from [4]).

2.6.3 Approximation of effective index and mode profile using Gaussians

It is well known that the fundamental mode of an optical fiber can be well approximated with a Gaussian beam especially in the practical range $1.8 \le V \le 2.4$, where $V = k_o a\sqrt{n_i^2 - n_o^2}$ is the normalized frequency, a is the core radius and n_i, n_o are the core and cladding index, respectively. In this range the fiber is single mode and the field is well confined. This approximation has the advantage of replacing a complicated expression for the mode field with a much simpler form $\sim e^{-(r/w)^2}$ which depends on a single parameter.

In order to find the parameter w which best approximates the mode field we use a trial field distribution $\phi(x, y)$ in a stationary expression for the propagation constant $\beta = 2\pi n_e/\lambda$ [3]. This approach leads to the best approximation for both w and n_e.

With a $e^{-j\beta z}$ z-dependence the scalar equation is:

$$\nabla_T^2\phi(x, y) + k_o^2[n^2(x, y) - n_e^2]\phi(x, y) = 0 \tag{2.96}$$

We multiply (2.96) by ϕ^* and integrate over all x,y to get:

$$n_e^2 = \frac{\iint n^2(x, y)|\phi(x, y)|^2 dxdy - \frac{1}{k_o^2}\iint|\nabla_T\phi(x, y)|^2 dxdy}{\iint|\phi(x, y)|^2 dxdy} \tag{2.97}$$

With $\phi = e^{-(r/w)^2}$, $r = \sqrt{x^2 + y^2}$ we obtain:

$$n_e^2 = n_i^2 - (n_i^2 - n_o^2)e^{-2\left(\frac{a}{w}\right)^2} - \frac{2}{k_o^2 w^2} \tag{2.98}$$

and the best width is found from

$$\frac{\partial n_e}{\partial w} = 0 \Rightarrow w = \frac{a}{\sqrt{\ln V}} \tag{2.99}$$

$$n_e^2 = n_i^2 - \frac{1}{k_o^2 a^2}(1 + 2\ln V) \tag{2.100}$$

We now apply the same method for a symmetric waveguide with rectangular cross-section and index distribution:

$$n(x, y) = \begin{cases} n_i & |x| \le a, |y| \le b \\ n_o & |x| > a, |y| > b \end{cases} \tag{2.101}$$

With the trial function $\phi(x, y) = e^{-[(x/w_x)^2 + (y/w_y)^2]}$ in (2.97) we get:

$$n_e^2 = \mathrm{erf}\left(\sqrt{2}\frac{a}{w_x}\right)\mathrm{erf}\left(\sqrt{2}\frac{b}{w_y}\right)(n_i^2 - n_o^2) + n_o^2 - \frac{1}{k_o^2}\left(\frac{1}{w_x^2} + \frac{1}{w_y^2}\right) \tag{2.102}$$

where

$$\mathrm{erf}(x) = \frac{2}{\sqrt{\pi}}\int_0^x \exp(-t^2)dt$$

The best estimate for the widths and the effective index is found from:

$$\frac{\partial n_e^2}{\partial w_x} = \frac{\partial n_e^2}{\partial w_y} = 0 \tag{2.103}$$

We note that for a step-index waveguide the approximation of the mode profile by a Gaussian is better suited for the field inside a waveguide core and for getting an approximate value of n_e. It is a poor approximation of the evanescent field in the cladding especially for strongly guided modes. However this approximation can be useful in the study of coupling between fibers and waveguides of different cross-sections.

Chapter 3

The Finite Difference Time Domain (FDTD) Method

3.1 The Yee algorithm

The FDTD method has been extensively applied to the design of complicated RF and microwave devices with dimensions comparable to the wavelength of operation. As the size of photonic components approaches that of the optical wavelength, FDTD has the potential to play a similarly useful role in the design of optical devices as a complement to the widely used beam propagation method (BPM).

The BPM has been the main modeling tool of waveguiding structures with slow variation along the propagation direction, negligible back-reflections and low beam divergence. It was first proposed in [8] and later in a more efficient form in [9]. Many extensions of the basic BPM scheme have been proposed to overcome its limitations, such as the wide-angle full-vector BPM [10] and the bidirectional BPM [11]. However, in practice, the BPM is not viewed as a suitable method for modelling high index-contrast structures that in general are characterized by strong guidance and rapid changes along the propagation direction. For such cases the FDTD may be a better choice.

The FDTD method solves the full vector Maxwell's equations without any approximation other than the replacement of differential equations with finite differences. The spatial domain is divided into a 2D or 3D mesh (in the simplest case rectangular) and, given an initial field distribution or a source excitation, the code updates, at every time step, the electric and magnetic fields at each location following Yee's algorithm [15]. This algorithm solves for both electric and magnetic fields in time and space using the coupled Maxwell's curl equations $\nabla\times\vec{E} = -\frac{\partial}{\partial t}\mu\vec{H}$, $\nabla\times\vec{H} = \frac{\partial}{\partial t}\varepsilon\vec{E}$ rather than solving for the electric or magnetic field alone with a wave equation. As shown in Figure 3.1 the Yee

algorithm places the $\vec{E}$ and $\vec{H}$ components in 3D space so that every $\vec{E}$ ($\vec{H}$) component is surrounded by four circulating $\vec{H}$ ($\vec{E}$) components. This provides a simple picture of a three dimensional space filled by an interlinked array of Faraday and Ampere contours which can be helpful in specifying field boundary conditions and singularities. Other features of this algorithm are [14]:

• The resulting finite-difference expressions for the space derivatives of the curl operators are central-differences and second-order accurate.

• Tangential and components are naturally continuous across material interfaces that are parallel to the grid coordinate axes so in this case no special care is needed to match the field boundary conditions at the interface.

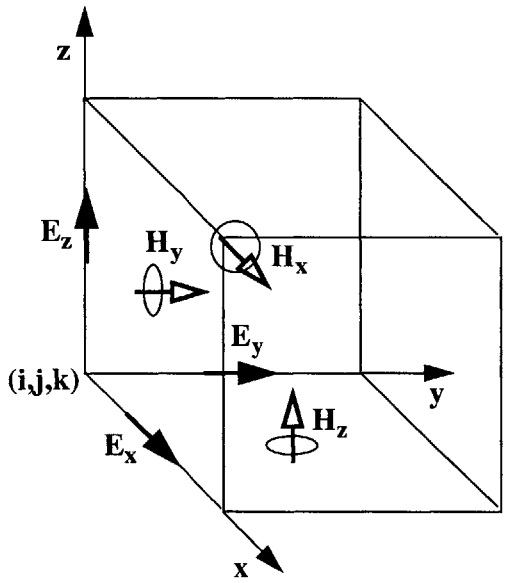

Figure 3.1: Yee's cell and assignment of electric and magnetic field components

• The material permittivity, permeability and conductivity at each component location have to be specified in advance. For a rectangular mesh this results in a staircase approxi-

mation of the geometry of interest with a space resolution set by the size of the lattice cell.

• The location of the $\vec{E}$ and $\vec{H}$ components in the grid and the central-differences of these components implicitly enforce Gauss's law so that the Yee mesh is divergence-free for a source-free space of interest.

• The $\vec{E}$ and $\vec{H}$ field components are in a leapfrog arrangement in time as illustrated in Figure 3.2. All the electric field computations in the space of interest are completed and stored in memory for a particular point in time. Then all the magnetic field computations in the space are completed and stored in memory using the electric field data just computed. The $\vec{E}$ field for the next point in time is then computed using the newly obtained $\vec{H}$ and this process continues until the time stepping is completed. This leapfrog time stepping is fully explicit and no matrix inversion is involved. The resulting finite-differences for the time derivatives are also central and second order accurate and the time stepping algorithm is non-dissipative.

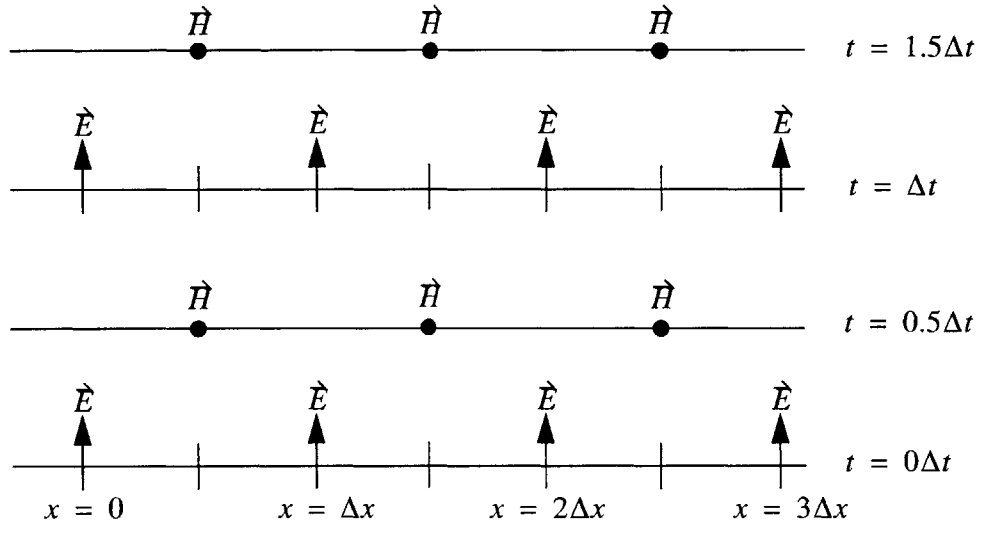

Figure 3.2: Space-time chart of the Yee algorithm showing the use of central differences for the space derivatives and leapfrog for the time derivatives (from [14]).

3.2 Finite Differencing

3.2.1 Three-dimensional algorithm

The field components are represented by 3D matrices based on the Yee cell as follows:

$$
\begin{aligned}
E_x(x, y, z;t) &= E_x((i+1/2)\Delta x, j\Delta y, k\Delta z, (n+1/2)\Delta t) \equiv E_x\big|_{i+1/2,\,j,\,k}^{n+1/2} \\
E_y(x, y, z;t) &= E_y(i\Delta x, (j+1/2)\Delta y, k\Delta z, (n+1/2)\Delta t) \equiv E_y\big|_{i,\,j+1/2,\,k}^{n+1/2} \\
E_z(x, y, z;t) &= E_z(i\Delta x, j\Delta y, (k+1/2)\Delta z, (n+1/2)\Delta t) \equiv E_z\big|_{i,\,j,\,k+1/2}^{n+1/2}
\end{aligned}
\tag{3.1}
$$

$$
\begin{aligned}
H_x(x, y, z;t) &= H_x(i\Delta x, (j+1/2)\Delta y, (k+1/2)\Delta z, n\Delta t) \equiv H_x\big|_{i,\,j+1/2,\,k+1/2}^{n} \\
H_y(x, y, z;t) &= H_y((i+1/2)\Delta x, j\Delta y, (k+1/2)\Delta z, n\Delta t) \equiv H_y\big|_{i+1/2,\,j,\,k+1/2}^{n} \\
H_z(x, y, z;t) &= H_z((i+1/2)\Delta x, (j+1/2)\Delta y, k\Delta z, n\Delta t) \equiv H_z\big|_{i+1/2,\,j+1/2,\,k}^{n}
\end{aligned}
\tag{3.2}
$$

As an example we show the expressions for the updating of the x-components of the electric and magnetic field at each grid point. Similar expressions can be derived for the rest of the field components.

$$
\begin{aligned}
E_x\big|_{i+1/2,\,j,\,k}^{n+1/2} &= \frac{1-\dfrac{\sigma_{i,j,k}\Delta t}{2\varepsilon_{i,j,k}}}{1+\dfrac{\sigma_{i,j,k}\Delta t}{2\varepsilon_{i,j,k}}} E_x\big|_{i+1/2,\,j,\,k}^{n-1/2} \\
&+ \frac{\dfrac{\Delta t}{\varepsilon_{i,j,k}}}{1+\dfrac{\sigma_{i,j,k}\Delta t}{2\varepsilon_{i,j,k}}} \left(\begin{array}{c} \dfrac{H_z\big|_{i+1/2,\,j+1/2,\,k}^{n} - H_z\big|_{i+1/2,\,j-1/2,\,k}^{n}}{\Delta y} \\ \dfrac{H_y\big|_{i+1/2,\,j,\,k+1/2}^{n} - H_y\big|_{i+1/2,\,j,\,k-1/2}^{n}}{\Delta z} \end{array} \right)
\end{aligned}
\tag{3.3}
$$

$$H_x\Big|_{i,\,j+1/2,\,k+1/2}^{n} = \frac{1-\dfrac{\sigma^*_{i,j,k}\Delta t}{2\mu_{i,j,k}}}{1+\dfrac{\sigma^*_{i,j,k}\Delta t}{2\mu_{i,j,k}}} H_x\Big|_{i,\,j+1/2,\,k+1/2}^{n-1}$$

$$-\frac{\dfrac{\Delta t}{\mu_{i,j,k}}}{1+\dfrac{\sigma^*_{i,j,k}\Delta t}{2\mu_{i,j,k}}}\left(\frac{E_z\Big|_{i,\,j+1,\,k+1/2}^{n+1/2} - E_z\Big|_{i+1/2,\,j,\,k+1/2}^{n+1/2}}{\Delta y} - \frac{E_y\Big|_{i,\,j+1/2,\,k+1}^{n+1/2} - E_y\Big|_{i,\,j+1/2,\,k}^{n+1/2}}{\Delta z}\right) \tag{3.4}$$

Where ε is the permittivity, μ the permeability, σ the electric conductivity and σ^* the magnetic conductivity, also represented by 3D matrices.

An important issue in the discretization is the proper choice of the time step Δt relative to the spatial steps Δx, Δy, Δz that guarantees the stability of the algorithm. It can be shown that the algorithm is stable when the following relationship holds:

$$c\Delta t \le \frac{1}{\sqrt{\dfrac{1}{(\Delta x)^2}+\dfrac{1}{(\Delta y)^2}+\dfrac{1}{(\Delta z)^2}}} \tag{3.5}$$

Equation (3.5) is known as the CFL criterion. If $\Delta x = \Delta y = \Delta z = \Delta$ then (3.5) is simplified to

$$\Delta t \le \frac{\Delta}{c\sqrt{3}} \tag{3.6}$$

It is noted that this simple stability condition holds for uniform rectangular grids while more complex conditions may be required for variable or unstructured meshing.

3.2.2 Two-dimensional algorithm

Because the full 3D FDTD simulation can be very demanding in time and memory it is often preferable to perform a calculation in a 2D domain derived from the initial 3D struc-

ture, by ignoring the variation of the fields along one direction, e.g along the z-axis. Then Maxwell's equations are decoupled into two systems of equations:

TE fields (E_x, E_y, H_z)

$$\frac{\partial E_x}{\partial t} = \frac{1}{\varepsilon}\left(\frac{\partial H_z}{\partial y} - \sigma E_x\right) \tag{3.7}$$

$$\frac{\partial E_y}{\partial t} = \frac{1}{\varepsilon}\left(-\frac{\partial H_z}{\partial x} - \sigma E_y\right) \tag{3.8}$$

$$\frac{\partial H_z}{\partial t} = \frac{1}{\mu}\left(\frac{\partial E_x}{\partial y} - \frac{\partial E_y}{\partial x} - \sigma^* H_z\right) \tag{3.9}$$

TM fields (E_z, H_x, H_y)

$$\frac{\partial H_x}{\partial t} = \frac{1}{\mu}\left(-\frac{\partial E_z}{\partial y} - \sigma^* H_x\right) \tag{3.10}$$

$$\frac{\partial H_y}{\partial t} = \frac{1}{\mu}\left(\frac{\partial E_z}{\partial x} - \sigma^* H_y\right) \tag{3.11}$$

$$\frac{\partial E_z}{\partial t} = \frac{1}{\varepsilon}\left(\frac{\partial H_y}{\partial x} - \frac{\partial H_x}{\partial y} - \sigma E_z\right) \tag{3.12}$$

and the discretization is analogous to the 3D case only now the fields and material properties are given by 2D matrices. Figure 3.3 shows how the Yee cell is modified in this case.

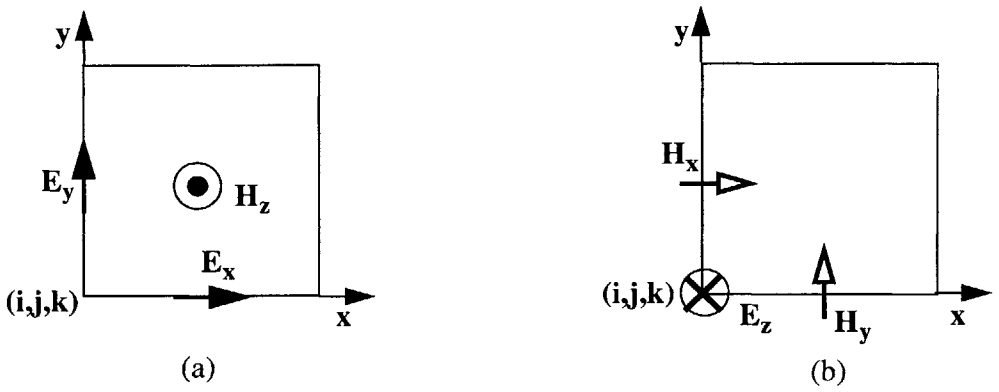

Figure 3.3: Yee's cell for the 2D case: (a) TE (b) TM

The stability condition (3.5) is modified accordingly:

$$c\Delta t \leq \frac{1}{\sqrt{\frac{1}{(\Delta x)^2} + \frac{1}{(\Delta y)^2}}} \tag{3.13}$$

which in the case $\Delta x = \Delta y = \Delta$ reduces to

$$\Delta t \leq \frac{\Delta}{c\sqrt{2}} \tag{3.14}$$

3.3 Boundary conditions

The main limitation of FDTD and other numerical methods based on finite-differencing, is the modelling of unbounded geometries by a finite computational domain. Thus the finite-difference equations must be modified at the boundaries of the truncated grid to approximate fields that are leaving the computational domain without back reflections. Many techniques have been proposed to implement an Absorbing Boundary Condition (ABC) [16],[17],[18]. These ABC's permits outgoing waves to leave the computational domain using a one-way wave equation. The waves incident on the boundaries still suffer from unwanted back reflections into the computational domain that are low close to normal incidence but can be high for other angles. These spurious reflections may contaminate the

simulation results and lead to instabilities, especially in the case of resonant structures. Many improvements of this technique have been developed that are based on a more accurate approximation of the one-way equation. A different approach was proposed in by Berenger[19],[20], called Perfectly Matched Layer (PML) that, compared with traditional ABCs, reduces spurious reflections by orders of magnitude from $\sim 10^{-2} - 10^{-3}$ down to $\sim 10^{-5} - 10^{-7}$ for all angles of incidence. This allows the border to be brought much closer to the structures inside the computational domain resulting in a smaller grid. The PML boundary condition, originally proposed in 2D, was extended to 3D [22]. It has also been used in other numerical tools such as finite-difference mode-solvers and BPM, [25] and [26], respectively.

In the PML technique the computational domain is surrounded by a layer of an artificial anisotropic conductor with graded electric and magnetic conductivity. Each electric and magnetic field component is split into two components in the absorbing boundary so that one component "sees" the loss and the other does not. The net effect is a non-physical absorbing medium adjacent to the outer FDTD mesh boundary that has a wave impedance independent of the angle of incidence and of the frequency of the scattered waves. The fields inside the PML decay exponentially very sharply and where the PML mesh is truncated the fields can be simply set to zero. Another way to view the PML is as a complex coordinate stretching transformation along the three cartesian coordinates [21].

In 3D all six vector field components are split and the resulting PML modification of Maxwell's equations yields 12 equations:

$$\mu_o \frac{\partial H_{xy}}{\partial t} + \sigma^*_y H_{xy} = \frac{\partial}{\partial y}(E_{zx} + E_{zy}) \qquad \mu_o \frac{\partial H_{xz}}{\partial t} + \sigma^*_z H_{xz} = \frac{\partial}{\partial z}(E_{yx} + E_{yz}) \tag{3.15}$$

$$\mu_o \frac{\partial H_{yz}}{\partial t} + \sigma^*_z H_{yz} = -\frac{\partial}{\partial z}(E_{xy} + E_{xz}) \qquad \mu_o \frac{\partial H_{yx}}{\partial t} + \sigma^*_x H_{yx} = \frac{\partial}{\partial x}(E_{zx} + E_{zy}) \tag{3.16}$$

$$\mu_o \frac{\partial H_{zx}}{\partial t} + \sigma^*_x H_{zx} = -\frac{\partial}{\partial z}(E_{yx} + E_{zy}) \qquad \mu_o \frac{\partial H_{zy}}{\partial t} + \sigma^*_y H_{zy} = \frac{\partial}{\partial x}(E_{xy} + E_{xz}) \tag{3.17}$$

$$\varepsilon_o \frac{\partial E_{xy}}{\partial t} + \sigma_y E_{xy} = \frac{\partial}{\partial y}(H_{zx} + H_{zy}) \qquad \varepsilon_o \frac{\partial E_{xz}}{\partial t} + \sigma_z E_{xz} = -\frac{\partial}{\partial z}(H_{yx} + H_{yz}) \tag{3.18}$$

$$\varepsilon_o \frac{\partial E_{yz}}{\partial t} + \sigma_z E_{yz} = \frac{\partial}{\partial z}(H_{xy} + H_{xz}) \qquad \varepsilon_o \frac{\partial E_{yx}}{\partial t} + \sigma_x E_{yx} = -\frac{\partial}{\partial x}(H_{zx} + H_{zy}) \tag{3.19}$$

$$\varepsilon_o \frac{\partial E_{zx}}{\partial t} + \sigma_x E_{zx} = \frac{\partial}{\partial z}(H_{yx} + H_{zy}) \qquad \varepsilon_o \frac{\partial E_{zy}}{\partial t} + \sigma_y E_{zy} = -\frac{\partial}{\partial x}(H_{xy} + H_{xz}) \tag{3.20}$$

In the 2D case only the z-component of the electric (magnetic) field for TE (TM) polarization is split into two subcomponents. For the TM case the modified Maxwell's equations are:

$$\varepsilon_o \frac{\partial E_{zx}}{\partial t} + \sigma_x E_{zx} = \frac{\partial H_y}{\partial z} \qquad \varepsilon_o \frac{\partial E_{zy}}{\partial t} + \sigma_y E_{zy} = \frac{\partial H_x}{\partial z} \tag{3.21}$$

$$\mu_o \frac{\partial H_x}{\partial t} + \sigma^*_y H_x = -\frac{\partial}{\partial y}(E_{zx} + E_{zy}) \qquad \mu_o \frac{\partial H_y}{\partial t} + \sigma^*_x H_y = \frac{\partial}{\partial z}(E_{zx} + E_{zy}) \tag{3.22}$$

The electric and magnetic conductivities $\sigma_{x,\,y,\,z}$ and $\sigma^*_{x,\,y,\,z}$ are chosen to match the wave impedance as:

$$\frac{\sigma_\alpha}{\varepsilon_o} = \frac{\sigma^*_\alpha}{\mu_o} \qquad \alpha = x, y, z \tag{3.23}$$

A schematic of the PML boundaries in 2D with the associated conductibities is shown in Figure 3.4.

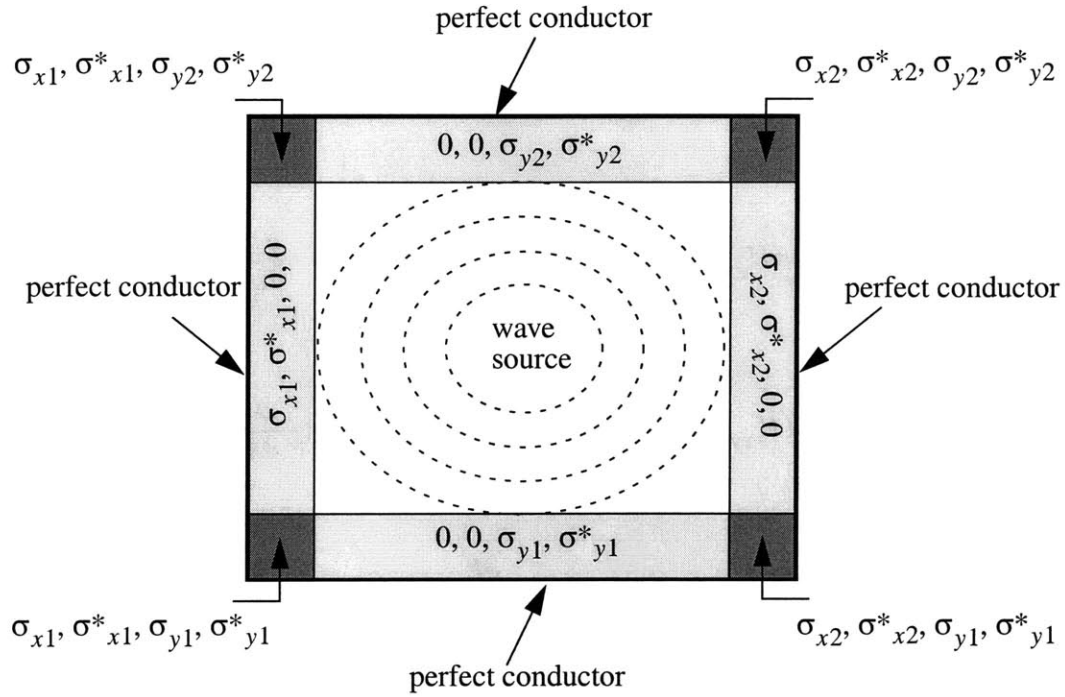

Figure 3.4: PML boundaries in a 2D computational domain

The loss is increased gradually with depth ρ within each PML as

$$\sigma(\rho) = \sigma_{max}\left(\frac{\rho}{\delta}\right)^n \tag{3.24}$$

where δ is the PML thickness. Typically $n = 2$, however it has been shown that the residual back reflection from the boundary is further reduced if $n = 4$ [27], which is used in this thesis as well.

From (3.24) we get a PML reflection factor of

$$R(\theta) = \exp\left(\frac{-2\sigma_{max}\delta\cos\theta}{(n+1)\varepsilon_o c}\right) \tag{3.25}$$

where θ is the angle of incidence. The conductivities are assigned by choosing $R(0)$ usually around 10^{-6}.

Because the attenuation of the outgoing waves within the PML is so rapid that the Yee time stepping algorithm may not be suitable; instead a exponential time stepping is used [14]. For example:

$$E_{zx}(t) = e^{-\sigma_x t/\varepsilon_o} E_{zx} + \frac{1}{\sigma_x}\frac{\partial H_y}{\partial x}\left(e^{-\sigma_x t/\varepsilon_o} - 1\right) \tag{3.26}$$

and the discretized form:

$$E_{zx}\Big|_{i,j}^{n+1/2} = e^{-\sigma_x \Delta t/\varepsilon_o} E_{zx}\Big|_{i,j}^{n-1/2} + \frac{e^{-\sigma_x \Delta t/\varepsilon_o} - 1}{\sigma_x \Delta x}\left(H_y\Big|_{i+1/2,j}^{n} - H_y\Big|_{i-1/2,j}^{n}\right) \tag{3.27}$$

The PML method has been modified to terminate optical waveguides in [23] and it is widely used in this form for simulations in guided wave optics. All the FDTD simulations in this thesis employ the same method. It must noted that in spite the superior performance of the PML, it has been shown that it does not act as an absorber for evanescent waves [24] which become more important for frequencies below the cutoff of waveguiding structures. However, most our simulations involve 2D waveguides with zero cutoff frequency (TE) thus no such problems are expected.

3.4 Source implementation

The simplest way to implement a source for the excitation of the fields in the computational domain is to impose a field or current with appropriate spatial and temporal dependence at one or more points, at each time step. This leads to a field that propagates in all directions (for a point source) or forwards and backwards (for a surface excitation) posing a problem when we want to find the back-reflections from an object of interest.

A modification of the FDTD algorithm known as total-field/scattered-field formulation is used to make the electromagnetic wave emanating from a source propagate in only one direction with negligible power flux in the opposite direction ([14] and references therein). This approach is based on the linearity of Maxwell's equations which allows a decomposition of the fields as

$$\begin{aligned} \vec{E}_{tot} &= \vec{E}_{inc} + \vec{E}_{scat} \\ \vec{H}_{tot} &= \vec{H}_{inc} + \vec{H}_{scat} \end{aligned} \tag{3.28}$$

where the incident fields $\vec{E}_{inc}, \vec{H}_{inc}$ are assumed known and are the field values that would exist in vacuum. $\vec{E}_{scat}, \vec{H}_{scat}$ are the scattered field values which are initially unknown and result from the interaction of the incident wave with any materials in the computational domain. The FDTD algorithm can be applied to each of these fields in a computational domain that is zoned into two regions as shown in Figure 3.5, a total fields region and a scattered fields region, separated by a virtual interface used to connect the fields in each region.

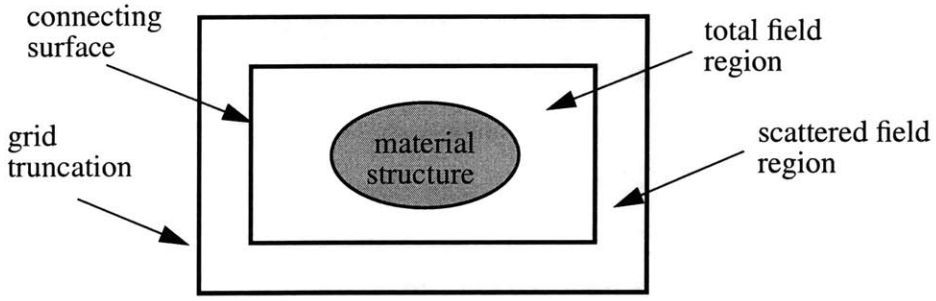

Figure 3.5: Zoning of FDTD grid (from [14])

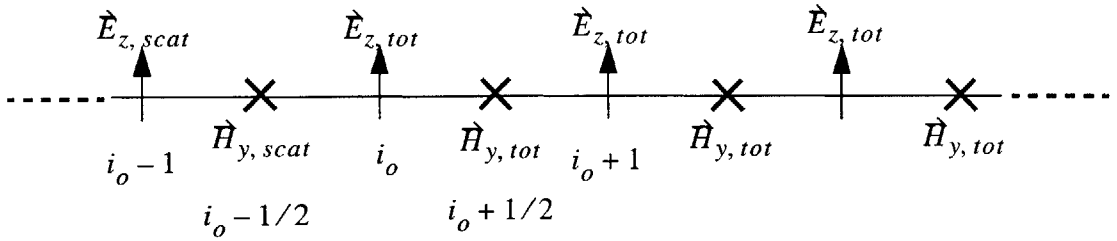

Figure 3.6: 1D example of total/scattered field region interface

Special care is needed when the finite differences are taken across to ensure consistency of the algorithm. The Yee algorithm naively applied across the interface of Figure 3.6 yields:

$$E_{z,\,tot}\Big|_{i_o}^{n+1} = E_{z,\,tot}\Big|_{i_o}^{n} + \frac{\Delta t}{\varepsilon \Delta x}\left(H_{y,\,tot}\Big|_{i_o+1/2}^{n+1/2} - H_{y,\,scat}\Big|_{i_o-1/2}^{n+1/2}\right) \tag{3.29}$$

stored in memory — stored in memory

$$H_{y,\,scat}\Big|_{i_o-1/2}^{n+1} = H_{y,\,scat}\Big|_{i_o-1/2}^{n-1/2} + \frac{\Delta t}{\mu \Delta x}\left(E_{z,\,tot}\Big|_{i_o}^{n} - E_{z,\,scat}\Big|_{i_o-1}^{n}\right) \tag{3.30}$$

stored in memory — stored in memory

In equations (3.29)and (3.30) scattered fields are subtracted from total fields and the updating of the total fields is incorrect. Correction terms that are functions of the assumed known incident fields must be added to make the algorithm consistent. We use the fact that:

$$H_{y,\,scat}\Big|_{i_o-1/2}^{n+1/2} = H_{y,\,tot}\Big|_{i_o-1/2}^{n+1/2} - H_{y,\,inc}\Big|_{i_o-1/2}^{n+1/2} \tag{3.31}$$

$$E_{z,\,tot}\Big|_{i_o}^{n} = E_{z,\,inc}\Big|_{i_o}^{n} + E_{z,\,scat}\Big|_{i_o}^{n} \tag{3.32}$$

and we substitute (3.31) into (3.29) and (3.32) into (3.30). The corrected relations now read:

$$E_{z,\,tot}\Big|_{i_o}^{n+1} = E_{z,\,tot}\Big|_{i_o}^{n} + \frac{\Delta t}{\varepsilon \Delta x}\left(H_{y,\,tot}\Big|_{i_o+1/2}^{n+1/2} - H_{y,\,tot}\Big|_{i_o-1/2}^{n+1/2}\right) - \frac{\Delta t}{\varepsilon \Delta x} H_{y,\,inc}\Big|_{i_o-1/2}^{n+1/2} \quad (3.33)$$

stored in memory — stored in memory — known

$$H_{y,\,scat}\Big|_{i_o-1/2}^{n+1} = H_{y,\,scat}\Big|_{i_o-1/2}^{n-1/2} + \frac{\Delta t}{\mu \Delta x}\left(E_{z,\,scat}\Big|_{i_o}^{n} - E_{z,\,scat}\Big|_{i_o-1}^{n}\right) - \frac{\Delta t}{\mu \Delta x} E_{z,\,inc}\Big|_{i_o}^{n} \quad (3.34)$$

stored in memory — stored in memory — known

The data for the incident fields have the time dependence of (3.38) (next section) or simply sinusoidal dependence $E_s(n) = \sin[2\pi f_o(n\Delta t - 3\tau)]$ and the spatial dependence can be chosen to be the fundamental mode profile at the center frequency f_o, for the waveguide where the source is located. This mode profile can be obtained using a finite difference mode-solver e.g. [28],[29] or can be approximated by a Gaussian profile. Other source options include electric or magnetic dipoles and planes waves, the latter being more common for sources in free space.

3.5 The use of Discrete Fourier Transform (DFT) in FDTD

It is often desirable to obtain frequency dependent phasor quantities from the time dependent real field quantities, for further processing. A typical example is the calculation of radiation (far) fields using the field distribution on surfaces within the computational domain. This is known as the near-to-far-field transformation and eliminates the need to extend the computational domain to the far field in order to obtain the far-field data ([14] and references therein).

In this thesis, we need the phasor quantities of the electric and magnetic fields in order to obtain the Poynting vector and consequently the power flux through waveguide cross sections as a function of frequency (e.g. as it is done in [38]). Thus transmission and reflection responses of the devices of interest can be calculated. These data can be efficiently and simultaneously obtained for multiple frequencies with only one FDTD run. A wideband electromagnetic excitation of the structure of interest is provided and the DFT

of all the field components is performed recursively in parallel with the time-stepping for each frequency of interest and point on the cross section. The DFT data for each frequency and point on the cross-section are stored in the memory as sums that are updated at each time step by the addition of the new term. For example in the 2D TE case, the calculation of the power flowing in the x-direction through a waveguide cross-section defined by $i = i_o, \quad j_1 \le j \le j_2$ is done through DFT sums that are updated at every time step, i.e.:

$$\begin{aligned}
\tilde{E}_{R,y}\Big|^{m}_{i_o,\, j+1/2} &= \tilde{E}_{R,y}\Big|^{m}_{i_o,\, j+1/2} + E_y\Big|^{n+1/2}_{i_o,\, j+1/2} \cos\left(2\pi f_m\left(n+\frac{1}{2}\right)\Delta t\right) \\
\tilde{E}_{I,y}\Big|^{m}_{i_o,\, j+1/2} &= \tilde{E}_{I,y}\Big|^{m}_{i_o,\, j+1/2} + E_y\Big|^{n+1/2}_{i_o,\, j+1/2} \left[-\sin\left(2\pi f_m\left(n+\frac{1}{2}\right)\Delta t\right)\right]
\end{aligned} \tag{3.35}$$

$$\begin{aligned}
\tilde{H}_{R,z}\Big|^{m}_{i_o,\, j} &= \tilde{H}_{R,z}\Big|^{m}_{i_o,\, j} + H_z\Big|^{n}_{i_o,\, j} \cos(2\pi f_m n\Delta t) \\
\tilde{H}_{I,z}\Big|^{m}_{i_o,\, j} &= \tilde{H}_{I,z}\Big|^{m}_{i_o,\, j} + H_z\Big|^{n}_{i_o,\, j} \left[-\sin(2\pi f_m n\Delta t)\right]
\end{aligned} \tag{3.36}$$

where m counts the discrete frequencies f_m of interest, and n is the time step. $\tilde{E}_{R,y}, \tilde{H}_{R,z}$ are the real parts of the DFT of the electric and magnetic fields at f_m and $\tilde{E}_{I,y}, \tilde{H}_{I,z}$ the corresponding imaginary parts. The power through the waveguide cross section at the each frequency f_m, is obtained after the completion of the time stepping by summing the real parts of the Poynting contributions over the entire cross section:

$$P_y^m = \sum_{j=j_1}^{j_2} \left\{ \tilde{E}_{R,x}\Big|^{m}_{i_o+1/2,\, j} \tilde{H}_{R,z}\Big|^{m}_{i_o,\, j} + \tilde{E}_{I,x}\Big|^{m}_{i_o+1/2,\, j} \tilde{H}_{I,z}\Big|^{m}_{i_o,\, j} \right\} \tag{3.37}$$

The electric field of the source excitation usually has a temporal dependence of the form:

$$E_s(n) = \exp\left[-\left(\frac{n\Delta t - 3\tau}{\tau}\right)^2\right]\sin[2\pi f_o(n\Delta t - 3\tau)] \tag{3.38}$$

and an appropriate spatial dependence, depending on the source location, e.g. the fundamental for waveguide excitation at the center frequency f_o.

The Gaussian pulse in time transforms to a Gaussian pulse in frequency which, with proper choice of τ, extends over the entire bandwidth of interest centered around f_o. The form of (3.38) ensures that the source waveform is essentially zero at the start of the time stepping and that it has odd symmetry in time about the peak of the Gaussian envelope. The spectrum of the source is concentrated about f_o and has zero dc component.

The DFTs of the fields along selected cross-sections can be also be used in overlap integrals (sums) with a known mode profile, following the discussion in Section 2.1 and assuming that the proper orthogonality and normalizations hold. Thus we can find the fraction of power coupled into this particular mode only instead of the total power flux that may contain contributions from other guided and radiation modes.

When we are interested of the spectrum of the field at only a few points, a faster method is to simply store at each time step the value of the field at the points of interest and then apply the Fast Fourier Transform (FFT) to the stored data.

When such calculations are performed the FDTD simulation must be run for a sufficiently large number of time steps so that the impulse response of the structure of interest has the time to ring down to zero otherwise the computed DFT is inaccurate due to windowing effects of the true impulse response. Similarly, a large number of time steps is required to ensure that the FFT can adequately resolve narrow spectral peaks, which is important when high-Q resonant structures are involved.

3.6 Resonator calculations using FDTD

The fact that with one FDTD simulation it is possible to obtain information about the behavior of a structure over a wide frequency range makes this method particularly suited for modeling resonant cavities. The quantities of interest are: (a) the resonant frequency and wavelength, (b) the quality factor Q_o due to loss or radiation (c) the quality factor Q_e due to external (direct or evanescent) coupling to waveguides, and (c) the reflection/transmission spectra at the ports of resonant systems with one or more input/output ports. The quality factors are related to the exponential decay rate of the amplitude of the resonant mode and the resonant frequency by:

$$Q_o = \frac{\omega_o \tau_o}{2} \qquad Q_e = \frac{\omega_o \tau_e}{2} \tag{3.39}$$

where $1/\tau_o$, $1/\tau_e$ are the decay rates of the resonant mode amplitude due to loss and external coupling, respectively. The total ("loaded") Q is given by

$$\frac{1}{Q} = \frac{1}{Q_o} + \frac{1}{Q_e} \tag{3.40}$$

and can be found by the power or intensity spectrum by

$$Q = \frac{f_o}{\Delta f_{1/2}} \tag{3.41}$$

where f_o is the resonant frequency and $\Delta f_{1/2}$ is the full width half maximum bandwidth of the Lorentzian response.

In order to find f_o and Q_o of an uncoupled cavity we first provide a source excitation in the form of a dipole within the cavity or the fundamental mode of a side-coupled waveguide. When the mode field is established inside the cavity the source is turned off, the coupling waveguide, if any, is removed and the cavity fields are left to ring down due to radiation. The field values at one or more points inside the cavity are stored in memory

at every step and the cavity is surrounded by a virtual box inside which the electromagnetic energy is calculated at each step in time. At the end of the simulation, the time sequence of the field values at the chosen point(s) is transformed by FFT to yield the amplitude spectrum assuming that the number of time steps has been sufficient for the FFT to accurately resolve the frequency response. If the resonances are very narrow the Q may not be extracted accurately from the spectrum. It is then preferable to extract it from the exponential decay of the amplitude at the monitored point or the decay rate of the energy in the virtual box and then use (3.39) to find Q_o. If the source bandwidth is wide enough to excite more than one high-Q resonances, the time dependent sequence of the field amplitude or the energy shows the beating of these modes at different frequencies and is not helpful to finding the decay rate. If Q_o cannot be found accurately from the widths of the spectral peaks obtained by FFT it may be necessary to rerun the simulation with a spectrally narrow excitation to ensure excitation of only one mode. The magnitude of the mode amplitude a decays exponentially as

$$|a(t)| = |a(0)|\exp\left(-\frac{t}{\tau}\right) = |a(0)|\exp\left(-\frac{\omega_o t}{2Q_o}\right) \tag{3.42}$$

and the energy W of the mode in the cavity decays as

$$W(t) = W(0)\exp\left(-\frac{\omega_o}{Q_o}t\right) \tag{3.43}$$

The Q can be easily extracted using the above relations from the slope of the functions $\ln(|a(t)|) = \ln(|a(0)|) - \omega_o t/2Q$ or $\ln(W(t)) = \ln(W(0)) - \omega_o t/Q$

To calculate the "loaded" Q of a resonant cavity due to coupling to a waveguide we start again by exciting the cavity with the mode of a side coupled waveguide and temporal dependence of the form of (3.38) to cover the bandwidth of interest. There is a buildup of

energy in the cavity which then decays into the waveguide. If the resonator supports standing wave modes then the total system acts as a reflector. The transmission spectrum (calculated by DFT during the simulation as described in Section 3.5) has a dip at the resonance frequency and the reflection spectrum has a peak at the resonance frequency. from the latter the total Q can be extracted using (3.41). If the cavity is lossless the transmission dip goes all the way to zero and the reflection peak goes up to unity. In practice there is always some loss which leads to incomplete reflection and the magnitude of the reflection peak depends on the ratio Q_o/Q_e. Thus f_o, Q_o, Q_e can be simply found from the transmission or reflection response. If the coupling between resonator and waveguide is very weak then the resonance frequency f_o and Q_o of the uncoupled resonator do not change in the presence of the waveguide. However, in most cases of interest, the coupling is strong enough to result in a shift of f_o and Q_o from the values of the unloaded resonator. The basic relations that allow an easy extraction of the basic resonator quantities from the transmission and/or reflection spectra of a resonator side-coupled to a waveguide are given below.

$$|T|^2 = \frac{\left(1-\frac{\omega}{\omega_o}\right)^2+\left(\frac{1}{2Q_o}\right)^2}{\left(1-\frac{\omega}{\omega_o}\right)^2+\left(\frac{1}{2Q}\right)^2} \qquad |R|^2 = \frac{\left(\frac{1}{2Q_e}\right)^2}{\left(1-\frac{\omega}{\omega_o}\right)^2+\left(\frac{1}{2Q}\right)^2} \tag{3.44}$$

and at resonance:

$$|T_o|^2 = \frac{1}{\left(1+\frac{Q_o}{Q_e}\right)^2} \qquad |R_o|^2 = \frac{1}{\left(1+\frac{Q_e}{Q_o}\right)^2} \tag{3.45}$$

In Chapter 4 these relations are used to exctract the Q's from FDTD simulation transmission data of resonant filters.

Chapter 4

Resonant Add/Drop Filters

4.1 Introduction

The wide use of optical wavelength division multiplexing (WDM) calls for compact, efficient filters for multiplexing and demultiplexing all the channels in a data stream or for adding and dropping an individual channel leaving all the rest unperturbed. The main requirements for the amplitude response of such filters are 1) low insertion loss 2) low crosstalk (typically < -25dB), that is rejection of out-of-band signals 3) fast roll-off of the passband edges. Recently the phase response has also received some attention in the context of communication systems [49]-[51].

Add/drop filters and multiplexers/demultiplexers are very important components in WDM systems and have been investigated extensively in the literature. Three broad types of filters have emerged [49]: 1) Mach-Zehnder interferometer (MZI) based devices which include the waveguide grating router (WGR) [32],[33] 2) fiber Bragg gratings (FBGs), including apodized and chirped gratings and 3) resonant cavity filters [35],[36],[44] which are the focus of this work. Filters of this type may offer superior spectral responses compared with the other filtering mechanisms. The passband shape of a resonator filter can be custom designed by the use of multiply coupled resonators [34],[36],[48]. Further, the response outside of the resonant passband is free of side lobes, and the roll-off rate along the passband edge is governed by the number of mutually coupled resonators. Resonator filters can also be analyzed as lumped elements, their response depends on each resonator as a unit, but not on the details of the resonator. The passband shape depends sensitively on the relative interactions among all resonators, and on their interactions with the bus waveguides to which the input and output ports are connected.

High index-contrast resonators have dimensions of a few wavelengths and are of particular interest as building blocks for resonant add/drop filters. They have a large free spectral range (FSR) and thus can accommodate the entire bandwidth of erbium-doped amplifiers, are capable of both filtering and routing functions, and are ideally suited to large-scale integration. Ring and disk resonators are the most common building blocks for resonant filtering and routing functions [36],[40]. The strong light confinement in high index-contrast systems allows Q's on the order of $10^3 - 10^4$ in rings with radius only $3 - 10\mu m$ [36]. This type of resonators supports a purely traveling wave, thus a single ring or disk resonator placed between two optical waveguides, one acting as the signal bus and the other as the receiving waveguide, can transfer all the channel power from the bus to the receiver. While this is an ideal basic structure for channel add/drop, its performance can be affected adversely by the coupling between counter propagating waves caused by surface roughness [41]. Moreover high-index contrast microring resonators are coupled to input and output waveguides via a point contact, and therefore a very small gap, of the order of 100 nm, is required for sufficient coupling which pose a challenge in the fabrication [39]. Racetrack resonators [42] may offer a solution to this problem but the effect of surface roughness is still an issue.

It has been shown that the performance of a ring channel dropping filter could be realized with a standing wave resonant structure instead, which is not as sensitive to surface roughness. The operating principle is based on the excitation of two degenerate modes in a symmetric resonant structure. The concept was first proposed using group theoretical arguments and illustrated numerically using photonic crystal microcavities [44],[45]. In this chapter we use a simpler formulation based on CMT in time to explain the operation of the filter and present numerical examples using conventional high index-contrast

waveguides and cavities [47]. The theory presented in the following sections is based on Section 2.5 and [47],[48].

4.2 Four-port system with single mode resonator

The basic implementation of the channel add/drop filters considered here is a four-port system that consists of a resonator placed between two waveguides. A schematic is shown in Figure 4.1. The resonator is evanescently coupled to the two waveguides which we shall refer to as the bus and the receiver, respectively. The response of this system can be found using the theory presented in section for evanescent resonator-waveguide coupling.

In this section, we consider a resonator that supports only one mode in the frequency range of interest, with amplitude denoted by a normalized to the mode energy.

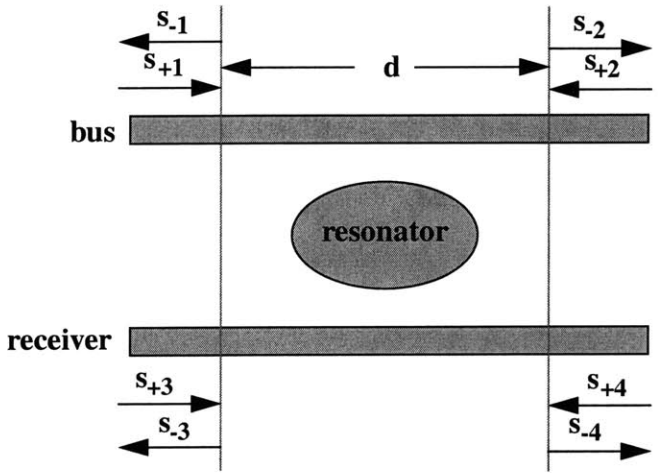

Figure 4.1: Schematic of a four-port filter consisting of a resonator evanescently coupled to two waveguides.

The waveguides are assumed to be single-mode and the waveguide dispersion is ignored in our analysis. This simplification is justified if the resonance peak is narrow. The amplitudes of the incoming (outgoing) waves in the bus are denoted by $s_{+1}(s_{-1})$ and $s_{+2}(s_{-2})$ and in the receiver waveguide by $s_{+3}(s_{-3})$ and $s_{+4}(s_{-4})$, respectively and are

normalized to the power in the waveguide mode. The squared magnitude of these amplitudes is equal to the power in the waveguide mode. The evolution of the resonator mode is described by:

$$\frac{da}{dt} = \left(j\omega_o - \frac{1}{\tau_o} - \frac{1}{\tau_e} - \frac{1}{\tau'_e}\right)a + \kappa_1 s_{+1} + \kappa_2 s_{+2} + \kappa_3 s_{+3} + \kappa_4 s_{+4} \tag{4.1}$$

where ω_o is the resonant frequency, $1/\tau_o$ is the decay rate due to loss, $1/\tau_e$, $1/\tau_e'$ are the rates of decay into the bus and the receiver, respectively, κ_1, κ_2 are the input coupling coefficients associated with the forward and backward propagating modes in the bus, and κ_3, κ_4 are similarly defined for the receiver. The decay rates are related to the unloaded quality factor and the external quality factors and of the resonator by $Q_o = \omega_o\tau_o/2$, $Q_e = \omega_o\tau_e/2$, $Q'_e = \omega_o\tau'_e/2$.

Following the analysis of section 2.5.2 the outgoing waves are given by:

$$s_{-1} = e^{-j\beta d}(s_{+2} - \kappa^*_2 a) \tag{4.2}$$

$$s_{-2} = e^{-j\beta d}(s_{+2} - \kappa^*_1 a) \tag{4.3}$$

$$s_{-3} = e^{-j\beta' d}(s_{+4} - \kappa^*_4 a) \tag{4.4}$$

$$s_{-4} = e^{-j\beta' d}(s_{+3} - \kappa^*_3 a) \tag{4.5}$$

where β, β' are the propagation constants in the bus and the receiver, respectively. As shown in 2.5.2, the squared magnitude of the coupling coefficients is equal to the decay rates into the waveguide modes. So we can write:

$$\kappa_i = \sqrt{\frac{1}{\tau_{e_i}}}e^{j\theta_i} \qquad i = 1,...,4 \tag{4.6}$$

with $1/\tau_{e1}(1/\tau_{e2})$ and $1/\tau_{e3}(1/\tau_{e4})$ defined as the decay rates in the forward (backward) direction in the bus and the receiver, respectively, satisfying:

$$\frac{1}{\tau_{e_1}} + \frac{1}{\tau_{e_2}} = \frac{2}{\tau_e} \qquad \frac{1}{\tau_{e_3}} + \frac{1}{\tau_{e_4}} = \frac{2}{\tau'_e} \tag{4.7}$$

and θ_i, $i = 1 \ldots 4$ are the respective phases. We choose 1 as the input port and we set $s_{+i} = 0$, $i = 2 \ldots 4$. If $s_{+1} \sim e^{j\omega t}$, then, from (4.1) we find, at steady state

$$a = \frac{\sqrt{\frac{1}{\tau_{e_1}}} e^{j\theta_1}}{j(\omega - \omega_o) + \frac{1}{\tau_o} + \frac{1}{\tau_e} + \frac{1}{\tau'_e}} s_{+1} \tag{4.8}$$

Substitution of (4.8) in (4.2)-(4.5) yields the filter response of the system:

$$\frac{s_{-1}}{s_{+1}} \equiv R = -e^{-j\beta d} \frac{\sqrt{\frac{1}{\tau_{e_1}\tau_{e_2}}} e^{j(\theta_1 - \theta_2)}}{j(\omega - \omega_o) + \frac{1}{\tau_o} + \frac{1}{\tau_e} + \frac{1}{\tau'_e}} \tag{4.9}$$

$$\frac{s_{-2}}{s_{+1}} \equiv T = e^{-j\beta d} \left(1 - \frac{\frac{1}{\tau_{e_1}}}{j(\omega - \omega_o) + \frac{1}{\tau_o} + \frac{1}{\tau_e} + \frac{1}{\tau'_e}} \right) \tag{4.10}$$

$$\frac{s_{-3}}{s_{+1}} \equiv D_L = -e^{-j\beta' d} \frac{\sqrt{\frac{1}{\tau_{e_1}\tau_{e_4}}} e^{j(\theta_1 - \theta_4)}}{j(\omega - \omega_o) + \frac{1}{\tau_o} + \frac{1}{\tau_e} + \frac{1}{\tau'_e}} \tag{4.11}$$

$$\frac{s_{-4}}{s_{+1}} \equiv D_R = -e^{-j\beta' d} \frac{\sqrt{\frac{1}{\tau_{e_1}\tau_{e_3}}} e^{j(\theta_1 - \theta_3)}}{j(\omega - \omega_o) + \frac{1}{\tau_o} + \frac{1}{\tau_e} + \frac{1}{\tau'_e}} \tag{4.12}$$

where R represents the reflection at the input port, T the transmission through the bus and D_L, D_R represent the transmission (channel dropping) into the left and right ports of

the receiver, respectively. From (4.9)-(4.12) we can derive the different behavior of a traveling wave and a standing-wave mode in this configuration.

Traveling wave mode: In this case the power in the resonator flows continuously in one direction only e.g. in a ring or disk resonator as shown in Figure 4.2(a). Thus, from(4.7) we have

$$\frac{1}{\tau_{e2}} = \frac{1}{\tau_{e3}} = 0$$
$$\frac{1}{\tau_{e3}} = \frac{2}{\tau_e} \qquad \frac{1}{\tau_{e4}} = \frac{2}{\tau'_e} \tag{4.13}$$

therefore (4.9),(4.12) lead to $R = D_R = 0$ over the entire bandwidth.

At $\omega = \omega_o$, the power incident in the bus in the forward direction is partially transferred to the receiver in the backward direction, limited only by loss. If in addition

$$\frac{1}{\tau_e} - \frac{1}{\tau'_e} = \frac{1}{\tau_o} \tag{4.14}$$

then at resonance, from (4.10),(4.11) we get $T = 0$ and $|D_L|^2 = 1 - \tau_e/\tau_o$, and the input signal power at $\omega = \omega_o$ is completely removed from the bus and transferred (dropped) to port 3 of the receiver reduced by a fraction τ_e/τ_o due to loss. Thus a system consisting of a single travelling mode resonator between two waveguides operates as first order channel dropping filter.

Standing wave mode: In this case there is no net power flowing in either direction of the resonator (pure standing wave) e.g. in a quarter-wave shifted DFB resonator as shown in Figure 4.2(b). The resonant mode decays equally into the forward and backward propagating modes of the waveguide so from (4.7) we have

$$\frac{1}{\tau_{e1}} = \frac{1}{\tau_{e2}} = \frac{1}{\tau_e} \qquad \frac{1}{\tau_{e3}} = \frac{1}{\tau_{e4}} = \frac{1}{\tau'_e} \tag{4.15}$$

If in addition (4.14) is satisfied, the power transfer into the receiver at resonance is maximized and from (4.9)-(4.12) we find $|R|^2 = |T|^2 = 0.25$ and $|D_L|^2 = |D_R|^2 = 0.25(1 - \tau_e/\tau_o)$. That is, at best, half the input power at $\omega = \omega_o$ remains in the bus and is equally distributed between ports 1 and 2 while the other half, reduced by a fraction τ_e/τ_o due to loss, is equally distributed into ports 3 and 4 of the receiver. Thus a single standing wave resonator between two waveguides is not sufficient for the channel dropping function. A theoretical example of the filter response illustrating the different behavior of the two types of resonators is shown in Figure 4.2(c).

Clearly, a single-mode traveling wave resonator side-coupled to the bus and the receiver can fully transfer a channel at the resonance frequency from the bus to the receiver while a single-mode standing wave resonator is not adequate for channel dropping.

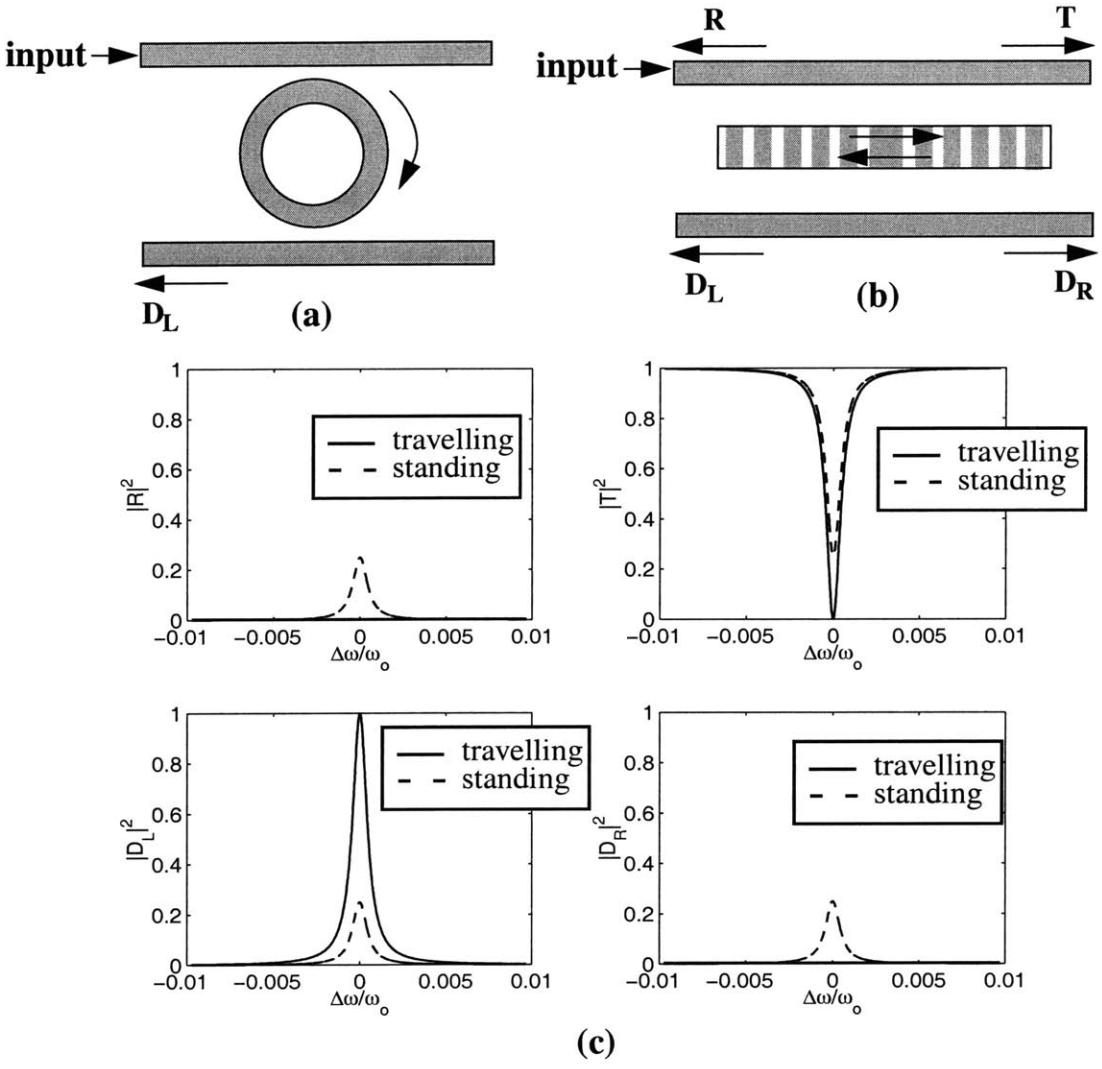

Figure 4.2: Four-port systems using (a) a traveling wave, (b) a standing wave resonator, and (c) an example of the corresponding filter response with $Q_e = Q'_e = 2000$ and negligible loss.

4.3 Symmetric standing-wave channel add/drop filters

In this section we show how it is possible to obtain the response of a single-mode traveling-wave resonant filter using a pair of standing-wave modes.

4.3.1 General form of a symmetric add/drop filter

We consider a resonant structure supporting two standing-wave modes, placed between the bus and the receiver, with a symmetry plane perpendicular to the waveguides, at

$z = 0$ as shown in the schematic of Figure 4.3(a). The two modes of the system are symmetric and anti-symmetric with respect to this plane. The symmetric mode has amplitude a_s and the anti-symmetric mode has amplitude a_a. With the reference planes defined at $z = \pm d/2$, the phases of the coupling coefficients differ by even (odd) multiples of π in the case of the symmetric (anti-symmetric) modes. Thus, the forward and backward incident waves couple into the symmetric mode *in phase* and into the anti-symmetric mode *out of phase* and the expressions for the resonator modes can be simplified as:

$$\frac{da_s}{dt} = \left(j\omega_s - \frac{1}{\tau_{o_s}} - \frac{1}{\tau_{e_s}} - \frac{1}{\tau'_{e_s}} \right) a_s + \kappa_s (s_{+1} + s_{+2}) + \kappa'_s (s_{+3} + s_{+4}) \tag{4.16}$$

$$\frac{da_a}{dt} = \left(j\omega_a - \frac{1}{\tau_{o_a}} - \frac{1}{\tau_{e_a}} - \frac{1}{\tau'_{e_a}} \right) a_a + \kappa_a (s_{+1} - s_{+2}) + \kappa'_a (s_{+3} - s_{+4}) \tag{4.17}$$

where $\omega_{s,a}$ are the resonant frequencies, $1/\tau_{o_{s,a}}$ are the decay rates due to loss, $1/\tau_{e_{s,a}}, 1/\tau'_{e_{s,a}}$ are the rates of decay into the signal bus and the receiver, respectively, and $\kappa_{s,a}$, $\kappa'_{s,a}$ are the input coupling coefficients associated with the bus and the receiver, respectively. The amplitudes of the outgoing waves are given by:

$$s_{-1} = e^{-j\beta d} (s_{+2} - \kappa^*_s a_s + \kappa^*_a a_a) \tag{4.18}$$

$$s_{-2} = e^{-j\beta d} (s_{+1} - \kappa^*_s a_s - \kappa^*_a a_a) \tag{4.19}$$

$$s_{-3} = e^{-j\beta' d} (s_{+4} - \kappa'^*_s a_s + \kappa'^*_a a_a) \tag{4.20}$$

$$s_{-4} = e^{-j\beta' d} (s_{+3} - \kappa'^*_s a_s - \kappa'^*_a a_a) \tag{4.21}$$

In analogy with (4.6), the input coupling coefficients can be written as

$$\kappa_{s,a} = \sqrt{\frac{1}{\tau_{e_{s,a}}}} e^{j\theta_{s,a}} \qquad \kappa'_{s,a} = \sqrt{\frac{1}{\tau'_{e_{s,a}}}} e^{j\theta'_{s,a}} \tag{4.22}$$

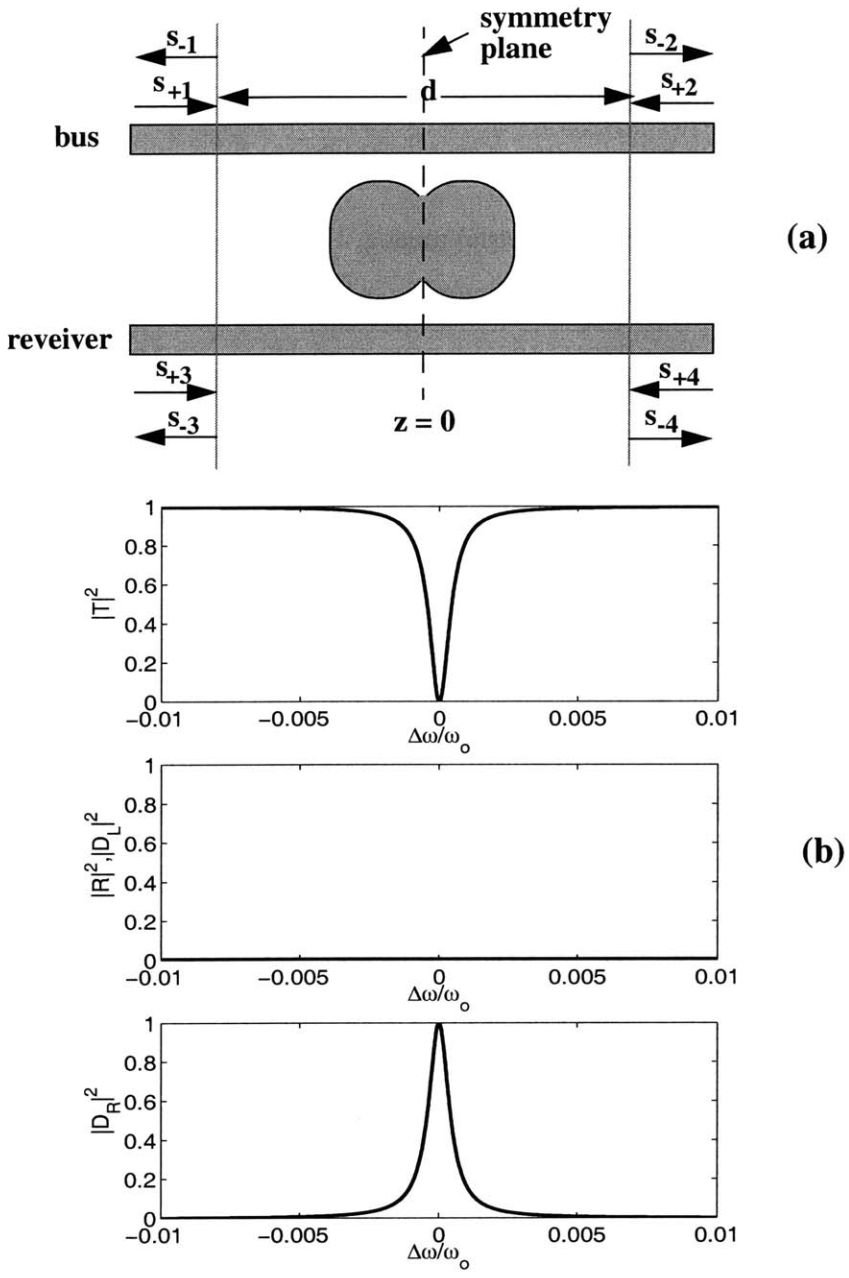

Figure 4.3: (a) Schematic of a channel dropping filter using a resonant structure with a symmetry plane perpendicular to the waveguides. (b) Filter response when a pair of degenerate symmetric and anti-symmetric standing-wave modes is excited with $Q_e = Q'_e = 2000$ and negligible loss.

With s_{+1} as the input signal at frequency ω, we find the filter response at the four ports of the system, at steady state.

$$R = e^{-j\beta d}\left(-\frac{\frac{1}{\tau_{e_s}}}{j(\omega-\omega_s)+\frac{1}{\tau_{o_s}}+\frac{1}{\tau_{e_s}}+\frac{1}{\tau'_{e_s}}} + \frac{\frac{1}{\tau_{e_a}}}{j(\omega-\omega_a)+\frac{1}{\tau_{o_a}}+\frac{1}{\tau_{e_a}}+\frac{1}{\tau'_{e_a}}} \right) \tag{4.23}$$

$$T = e^{-j\beta d}\left(1-\frac{\frac{1}{\tau_{e_s}}}{j(\omega-\omega_s)+\frac{1}{\tau_{o_s}}+\frac{1}{\tau_{e_s}}+\frac{1}{\tau'_{e_s}}} - \frac{\frac{1}{\tau_{e_a}}}{j(\omega-\omega_a)+\frac{1}{\tau_{o_a}}+\frac{1}{\tau_{e_a}}+\frac{1}{\tau'_{e_a}}} \right) \tag{4.24}$$

$$D_L = e^{-j\beta' d}\left(-\frac{\sqrt{\frac{1}{\tau_{e_s}\tau'_{e_s}}}e^{j(\theta_s-\theta'_s)}}{j(\omega-\omega_s)+\frac{1}{\tau_{o_s}}+\frac{1}{\tau_{e_s}}+\frac{1}{\tau'_{e_s}}} + \frac{\sqrt{\frac{1}{\tau_{e_a}\tau'_{e_a}}}e^{j(\theta_a-\theta'_a)}}{j(\omega-\omega_a)+\frac{1}{\tau_{o_a}}+\frac{1}{\tau_{e_a}}+\frac{1}{\tau'_{e_a}}} \right) \tag{4.25}$$

$$D_R = e^{-j\beta' d}\left(-\frac{\sqrt{\frac{1}{\tau_{e_s}\tau'_{e_s}}}e^{j(\theta_s-\theta'_s)}}{j(\omega-\omega_s)+\frac{1}{\tau_{o_s}}+\frac{1}{\tau_{e_s}}+\frac{1}{\tau'_{e_s}}} - \frac{\sqrt{\frac{1}{\tau_{e_a}\tau'_{e_a}}}e^{j(\theta_a-\theta'_a)}}{j(\omega-\omega_a)+\frac{1}{\tau_{o_a}}+\frac{1}{\tau_{e_a}}+\frac{1}{\tau'_{e_a}}} \right) \tag{4.26}$$

The two modes are degenerate if they have equal frequencies and equal decay rates:

$$\omega_s = \omega_a = \omega_o \tag{4.27}$$

$$\tau_{e_s} = \tau_{e_a} = \tau_e \tag{4.28}$$

$$\tau'_{e_s} = \tau'_{e_a} = \tau'_e \tag{4.29}$$

$$\tau_{o_s} = \tau_{o_a} = \tau_o \tag{4.30}$$

Under these conditions,(4.23) gives $R = 0$ over the entire bandwidth of the resonator and equations (4.24)-(4.26) become:

$$T = e^{-j\beta d}\left(1 - \frac{\frac{2}{\tau_e}}{j(\omega-\omega_o)+\frac{1}{\tau_o}+\frac{1}{\tau_e}+\frac{1}{\tau'_e}}\right) \tag{4.31}$$

$$D_L = -je^{j\left(\frac{(\theta_s+\theta_s)-(\theta'_s+\theta'_a)}{2}-\beta' d\right)}\frac{\frac{2}{\sqrt{\tau_e\tau'_e}}}{j(\omega-\omega_o)+\frac{1}{\tau_o}+\frac{1}{\tau_e}+\frac{1}{\tau'_e}}\sin\left(\frac{\Delta\theta}{2}\right) \tag{4.32}$$

$$D_R = -e^{j\left(\frac{(\theta_s+\theta_a)-(\theta'_s+\theta'_a)}{2}-\beta' d\right)}\frac{\frac{2}{\sqrt{\tau_e\tau'_e}}}{j(\omega-\omega_o)+\frac{1}{\tau_o}+\frac{1}{\tau_e}+\frac{1}{\tau'_e}}\cos\left(\frac{\Delta\theta}{2}\right) \tag{4.33}$$

where: $\Delta\theta = (\theta_s - \theta'_s) - (\theta_a - \theta'_a)$. At the resonance frequency the transmission through the bus is:

$$T = e^{-j\beta l}\frac{\frac{1}{\tau_o}+\frac{1}{\tau'_e}-\frac{1}{\tau_e}}{\frac{1}{\tau_o}+\frac{1}{\tau'_e}+\frac{1}{\tau_e}} \tag{4.34}$$

This expression shows that, as in the case of a travelling wave resonator, if the decay rates satisfy (4.14), the input signal power is completely removed from the bus and transferred to the receiver reduced by a fraction τ_e/τ_o due to loss. Under this condition, the bandwidth of the Lorentzian response is determined entirely by the coupling to the bus waveguide and its peak is set by the ratio τ_e/τ_o. The distribution of the dropped signal power between the two receiver ports is determined by the phase difference $\Delta\theta$ as follows:

i) If $\Delta\theta = 2n\pi$, where n is an integer, then $D_L = 0$ for all frequencies and we have forward drop. This condition implies that if the resonant structure has a horizontal symmetry plane as well, i.e. parallel to the waveguides, the symmetric and anti-symmetric modes have the same symmetry (even, if $\theta_{s,a} - \theta'_{s,a} = 0$ or odd, if $\theta_{s,a} - \theta'_{s,a} = \pi$) with

respect to this plane. This is illustrated in Figure 4.4 and typical response is shown in Figure 4.3(b). An example for this case is a composite system made up of two identical standing wave resonators [47], as we shall see in the next section

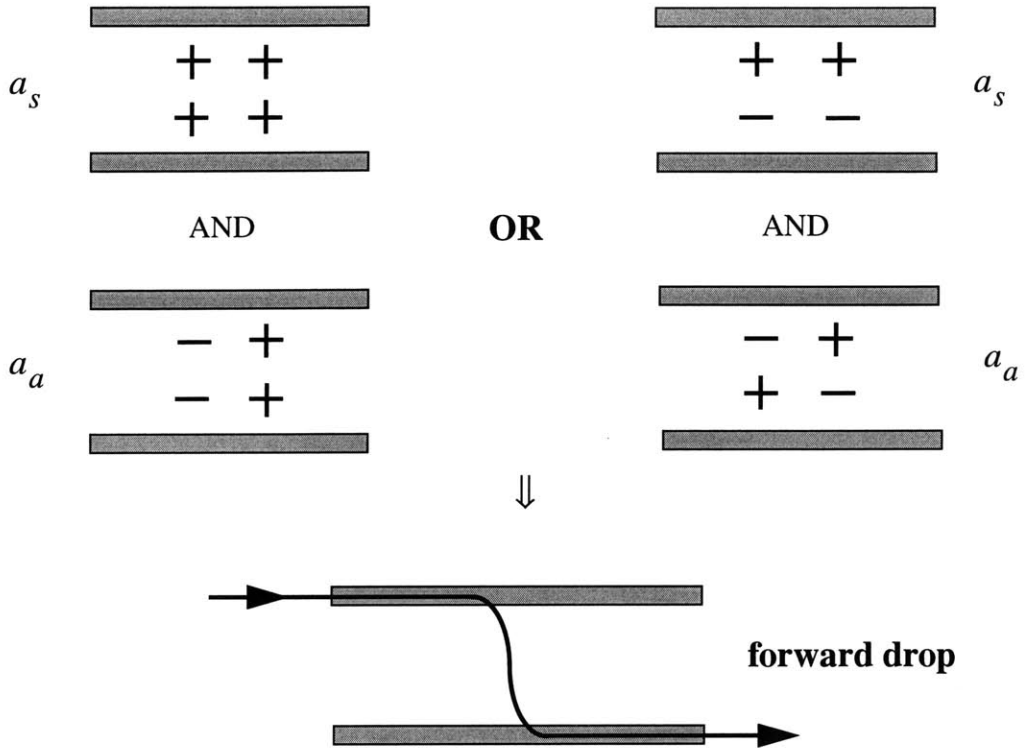

Figure 4.4: Illustration of mode symmetries required for forward drop (case i).

ii) If $\Delta\theta = (2n+1)\pi$, then $D_R = 0$ for all frequencies and we have backward drop. This condition implies that if the resonant structure has a horizontal symmetry plane as well, the symmetric mode has even (odd) symmetry, i.e. $\theta_s - \theta'_s = 0(\pi)$, and the anti-symmetric mode has odd (even) symmetry, i.e. $\theta_a - \theta'_a = \pi(0)$ with respect to this plane. This is illustrated in Figure 4.5. An example for this case is a ring resonator [36], if we consider its traveling-wave modes as superpositions of degenerate symmetric and anti-symmetric standing-wave modes that are excited with a $\pi/2$-phase difference

iii) In any other case both D_L and D_R are nonzero.

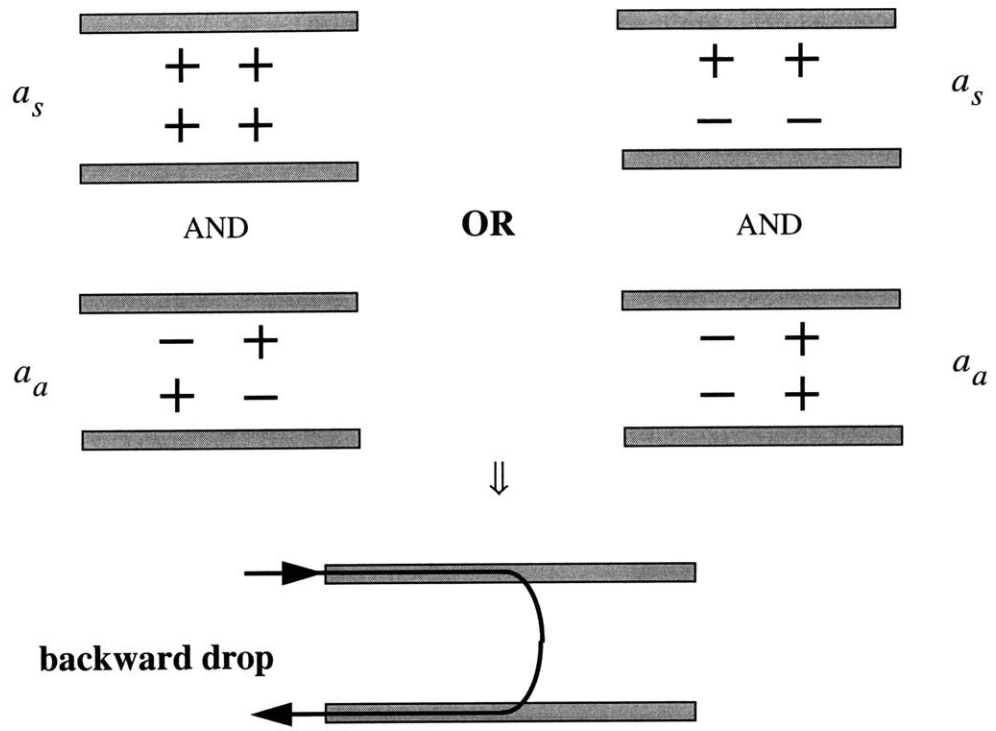

Figure 4.5: Illustration of mode symmetries required for backward drop (case ii)

4.3.2 Symmetric add/drop filter with two identical standing-wave cavities

The symmetric resonant system analyzed in the previous section can be implemented using two identical coupled resonators, each supporting only one standing-wave mode in the frequency range of interest. The resonator pair is placed between the bus and the receiver waveguides, so that the total system has a symmetry plane at $z = 0$. A schematic is shown in Figure 4.6. Normally, the mutual coupling of the two resonators would split the resonant frequencies (Section 2.5.1), lifting the degeneracy. In this section, we show that the coupling to the waveguides can be designed to cancel the effect of frequency splitting caused by the mutual coupling and to reestablish the degeneracy.

The mode amplitudes of the resonator on the left and on the right of the symmetry plane are denoted by a_L and a_R, respectively. The resonant frequency, decay rates, and coupling constants for the left resonator are defined as in Section 4.2, and for the right resonator are found by mirror symmetry. The resonator on the left is excited from the left by s_{+1} and s_{+3}, and from the right by the outputs of the right resonator. The resonator on the right is excited from the right by s_{+2} and s_{+4} and from the left by the outputs of the left resonator. The distance from the left (right) reference plane of the resonator on the left of the symmetry plane to the left (right) reference plane of the resonator on the right of the symmetry plane is denoted by l, as shown in Figure 4.6, and for simplicity is the same in both waveguides. The equations for the mode amplitudes for the two resonators are:

$$\begin{aligned}\frac{da_L}{dt} &= \left(j\omega_o - \frac{1}{\tau_o} - \frac{1}{\tau_e} - \frac{1}{\tau'_e}\right)a_L - j\mu a_R \\ &+ \sqrt{\frac{1}{\tau_e}}e^{j\theta_1}s_{+1} + \sqrt{\frac{1}{\tau_e}}e^{j\theta_2}e^{-j\beta l}\left(s_{+2} - \sqrt{\frac{1}{\tau_e}}e^{-j\theta_1}a_R\right) \\ &+ \sqrt{\frac{1}{\tau'_e}}e^{j\theta_3}s_{+3} + \sqrt{\frac{1}{\tau'_e}}e^{j\theta_4}e^{-j\beta' l}\left(s_{+4} - \sqrt{\frac{1}{\tau'_e}}e^{-j\theta_3}a_R\right)\end{aligned} \tag{4.35}$$

$$\begin{aligned}\frac{da_R}{dt} &= \left(j\omega_o - \frac{1}{\tau_o} - \frac{1}{\tau_e} - \frac{1}{\tau'_e}\right)a_R - j\mu a_L \\ &+ \sqrt{\frac{1}{\tau_e}}e^{j\theta_1}s_{+2} + \sqrt{\frac{1}{\tau_e}}e^{j\theta_2}e^{-j\beta l}\left(s_{+1} - \sqrt{\frac{1}{\tau_e}}e^{-j\theta_1}a_L\right) \\ &+ \sqrt{\frac{1}{\tau'_e}}e^{j\theta_3}s_{+4} + \sqrt{\frac{1}{\tau'_e}}e^{j\theta_4}e^{-j\beta' l}\left(s_{+3} - \sqrt{\frac{1}{\tau'_e}}e^{-j\theta_3}a_L\right)\end{aligned} \tag{4.36}$$

where μ is the mutual coupling coefficient between the resonators and is real by power conservation. For the decay rates, we have used the fact that a standing-wave mode decays equally into both directions.

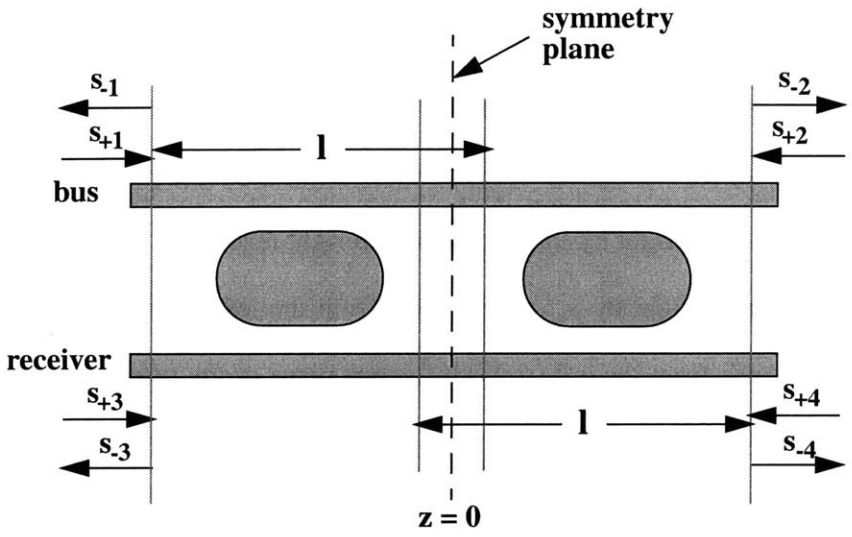

Figure 4.6: Schematic of a symmetric channel dropping filter employing two identical standing wave resonators

Expressions analogous to (4.2)-(4.5) have been used for the outgoing waves of the left (right) resonator that appear as inputs to the right (left) resonator. In (4.35),(4.36) we can see that, in addition to the direct coupling expressed by, the two resonators are also indirectly coupled through the waveguides. We define the amplitude of the symmetric and antisymmetric modes of the total system as

$$a_s = \frac{a_L + a_R}{\sqrt{2}} \qquad a_a = \frac{a_L - a_R}{\sqrt{2}} \tag{4.37}$$

which, due to (4.35) and (4.36), satisfy the following relations:

$$\frac{d}{dt}\begin{Bmatrix} a_s \\ a_a \end{Bmatrix} = \left[j\omega_o \mp \left(\mu - \frac{1}{\tau_e}\sin\phi - \frac{1}{\tau'_e}\sin\phi' \right) \right] \begin{Bmatrix} a_s \\ a_a \end{Bmatrix}$$

$$- \left[\frac{1}{\tau_o} + \frac{1}{\tau_e}(1 \pm \cos\phi) + \frac{1}{\tau'_e}(1 \pm \cos\phi') \right] \begin{Bmatrix} a_s \\ a_a \end{Bmatrix}$$

$$+ \sqrt{\frac{2}{\tau_e}} e^{j\left(\frac{\theta_1 + \theta_2 - \beta l}{2}\right)} \begin{Bmatrix} \cos\frac{\phi}{2} \\ j\sin\frac{\phi}{2} \end{Bmatrix} (s_{+1} \pm s_{+2}) \tag{4.38}$$

$$+ \sqrt{\frac{2}{\tau'_e}} e^{j\left(\frac{\theta_3 + \theta_4 - \beta' l}{2}\right)} \begin{Bmatrix} \cos\frac{\phi'}{2} \\ j\sin\frac{\phi'}{2} \end{Bmatrix} (s_{+3} \pm s_{+4})$$

where:

$$\begin{aligned} \phi &= \beta l + \theta_1 - \theta_2 \\ \phi' &= \beta' l + \theta_3 - \theta_4 \end{aligned} \tag{4.39}$$

Comparing (4.38) with (4.16) and (4.17) we have

$$\begin{Bmatrix} \omega_s \\ \omega_a \end{Bmatrix} = \omega_o \mp \left(\mu - \frac{1}{\tau_e}\sin\phi - \frac{1}{\tau'_e}\sin\phi' \right) \tag{4.40}$$

$$\begin{Bmatrix} \kappa_s \\ \kappa_a \end{Bmatrix} = \sqrt{\frac{2}{\tau_e}} e^{j\left(\frac{\theta_1 + \theta_2 - \beta l}{2}\right)} \begin{Bmatrix} \cos\frac{\phi}{2} \\ j\sin\frac{\phi}{2} \end{Bmatrix} \tag{4.41}$$

$$\begin{Bmatrix} \kappa_s \\ \kappa_a \end{Bmatrix} = \sqrt{\frac{2}{\tau'_e}} e^{j\left(\frac{\theta_3 + \theta_4 - \beta' l}{2}\right)} \begin{Bmatrix} \cos\frac{\phi'}{2} \\ j\sin\frac{\phi'}{2} \end{Bmatrix} \tag{4.42}$$

$$\frac{1}{\tau_{o_s}} = \frac{1}{\tau_{o_a}} = \frac{1}{\tau_o} \tag{4.43}$$

$$\frac{1}{\tau_{es}} = |\kappa_s|^2 \qquad \frac{1}{\tau_{ea}} = |\kappa_a|^2 \tag{4.44}$$

$$\frac{1}{\tau'_{es}} = |\kappa'_s|^2 \qquad \frac{1}{\tau'_{ea}} = |\kappa'_a|^2 \tag{4.45}$$

From (4.41) and (4.42), we can see that the symmetric and the antisymmetric excitations couple into the system with a $\pi/2$ phase difference. In the special case that φ and φ' are even (odd) multiples of π, only the symmetric (antisymmetric) mode is excited, leading to the behavior of the standing wave resonant system described in, with decay rates $2/\tau_e$ and $2/\tau'_e$ into the bus and the receiver, respectively, and $1/\tau_o$ due to loss. The conclusions derived for the filter response of the symmetric system shown in apply to this system as well: the system can operate as a channel add drop filter if its symmetric and antisymmetric modes satisfy the degeneracy conditions (4.27)-(4.29). The decay rates due to loss are already equal, as seen in (4.43). From (4.40), the condition degenerate frequencies is satisfied if:

$$\mu - \frac{1}{\tau_e}\sin\phi - \frac{1}{\tau'_e}\sin\phi' = 0 \tag{4.46}$$

and from (4.41)-(4.42) the conditions for equal decay rates are satisfied if:

$$\begin{aligned} \cos\phi &= 0 \\ \cos\phi' &= 0 \end{aligned} \tag{4.47}$$

Therefore, there are two degrees of freedom in designing this system: knowing the propagation constants β, β' and the phase differences $\theta_1 - \theta_2$ and $\theta_3 - \theta_4$, we must choose the distance l so that the symmetric and antisymmetric modes have decay rates equal to those of the individual resonators $1/\tau_e$ and $1/\tau'_e$. Then, by varying the coupling between the waveguides and the resonators, we must make $1/\tau_e$ and $1/\tau'_e$. such that the splitting of the resonance frequencies due to direct coupling between the two resonators is cancelled.

The signal power at resonance is completely removed from the bus if the degenerate decay rates satisfy the maximum power transfer condition (4.14). In this special case, the bandwidth of the Lorentzian response is then set by τ_e and the peak power at the output ports of the receiver by the ratio τ_e/τ_o. However the symmetry of the response between add and drop functions is lost.

The direction of channel drop is determined by the phase difference $\Delta\theta$ as explained in 4.3.1. From (4.41)-(4.42) we can see that:

$$\theta_s - \theta_a = \begin{cases} -\frac{\pi}{2} & \text{if } \sin\phi > 0 \\ \frac{\pi}{2} & \text{if } \sin\phi < 0 \end{cases} \tag{4.48}$$

$$\theta'_s - \theta'_a = \begin{cases} -\frac{\pi}{2} & \text{if } \sin\phi' > 0 \\ \frac{\pi}{2} & \text{if } \sin\phi' < 0 \end{cases} \tag{4.49}$$

Therefore $\Delta\theta = 0$, if the degeneracy conditions are satisfied with $\phi - \phi' = 2n\pi$, where n is an integer, and we have forward drop. If $\phi - \phi' = 2(n+1)\pi$, then $\Delta\theta = \pm\pi$ and we have backward drop. In this particular case it is possible to satisfy (4.46) even if the resonators are not directly coupled $\mu = 0$ provided that $1/\tau_e = 1/\tau'_e$.

The design of the filter is simplified when each resonator also has a plane of symmetry perpendicular to the waveguides. Then the distance l is equal to the distance between the individual symmetry planes. In addition, the mode supported by each waveguide is symmetric or antisymmetric with respect to this individual symmetry plane. Thus, the phases of the coupling coefficients κ_i, $i = 1...4$, that were defined in (4.6) for the general resonant system, satisfy:

$$\theta_1 - \theta_2 = \theta_3 - \theta_4 = 0 \tag{4.50}$$

for symmetric individual modes, and:

$$\theta_1 - \theta_2 = \theta_3 - \theta_4 = \pm\pi \tag{4.51}$$

for antisymmetric individual modes. Using (4.50) and (4.51) in (4.39) and substituting the latter in the degeneracy conditions (4.46)-(4.47) we get:

$$\mu \mp \frac{1}{\tau_e}\sin(\beta l) \mp \frac{1}{\tau'_e}\sin(\beta' l) = 0 \tag{4.52}$$

$$\cos(\beta l) = \cos(\beta' l) = 0 \tag{4.53}$$

These relations show that the choice of l depends on the symmetry of the individual modes that make up the symmetric and antisymmetric modes of the total system. For example, if $\tau_e = \tau'_e$ and $\beta = \beta'$ then as we can see from equation (4.52), the resonance frequencies are degenerate only if $l = (n + 1/4)\lambda_g$ for symmetric individual modes and only if $l = (n + 3/4)\lambda_g$ for antisymmetric individual modes, where $\lambda_g = 2\pi/\beta$ id the guided wavelength.

In the above analysis the frequency dependence of β has been ignored. Strictly speaking the degeneracy conditions can be exactly satisfied only at the resonant frequency and, depending on the waveguide dispersion there is a deviation from these conditions away

from resonance as the optical length of l changes. If we modify the coupling of modes analysis to include a linear approximation for β of the form:

$$\beta(\omega) = \beta(\omega_o) + \frac{1}{\upsilon_g}(\omega - \omega_o) \tag{4.54}$$

where υ_g is the group velocity, or for the effective index:

$$n_e(\lambda) = n_e(\lambda_o) + \left.\frac{\partial n_e}{\partial \lambda}\right|_{\lambda_o} (\lambda - \lambda_o) \tag{4.55}$$

it turns out that the response at the throughput and receiver ports is not affected but the reflection response is slightly modified. Specifically the reflection is zero at resonance and very small but nonzero symmetrically around the resonance. This will be shown later in an example.

As building blocks for this type of filter we can use a variety of standing wave resonators, such as polygon resonators, photonic crystal microcavities, quarter-wave-shifted DFB resonators etc., provided that their FSR and loss are within acceptable limits.

4.4 FDTD simulations

The concepts presented in the previous sections are now demonstrated with 2D FDTD simulations.

4.4.1 Polygon resonators

Although high-Q standing-wave resonances can be achieved by grating-based cavities we choose to consider high index-contrast cavities of polygon shape, due to their simplicity and small size. In spite of the presence of corners such cavities can support high-Q modes with the nulls of their electric field along the diagonals. We have investigated such resonators by 2D FDTD simulations using the approach explained in Section 3.6. The structures are viewed as infinite in the third dimension greatly simplifying the problem and the electric field polarization was taken perpendicular to the plane. Some representative examples

in $3 \div 1$ index contrast are shown below:

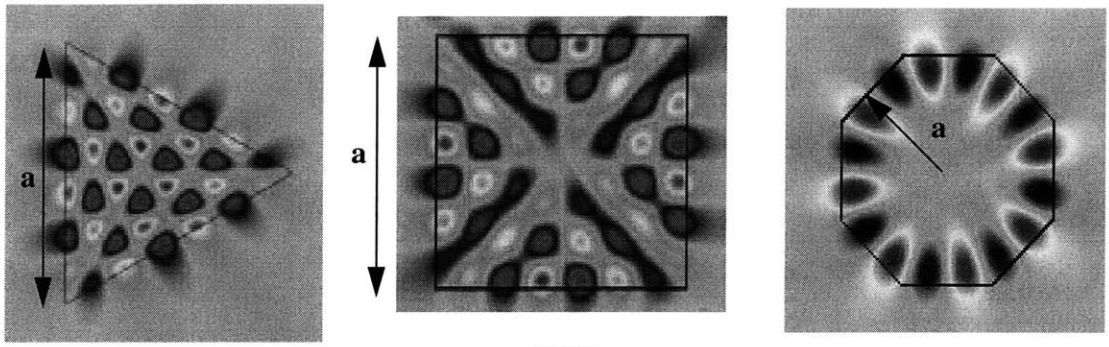

a = 3μm
Q_0 = 5300

a = 2.25μm
Q_0 = 25000

a = 0.88 μm
Q_0 = 42500

Figure 4.7: Examples of high-Q modes in polygon resonators. Electric field patterns and Q's found by 2D FDTD for 3/1 index contrast

Next, we demonstrate the concepts presented in the theory by performing 2D FDTD simulations on a system consisting of two high index-contrast waveguides and square resonators. The electric field polarization is chosen again perpendicular to the paper. The computational domain is discretized into a uniform orthogonal mesh with a cell size of 20 nm. In the examples presented here we use waveguides and resonators with core index $n_i = 3$ surrounded by air $n_o = 1$. The waveguides are 0.26 μm wide with effective index $n_e = 2.45022$ at $\lambda = 1550\,\text{nm}$ and the square resonators are $1.66\,\mu\text{m}$ each side with radiation Q significantly lower than that of Figure 4.7. The resonance characteristics of the uncoupled square resonator are summarized in Figure 4.8.

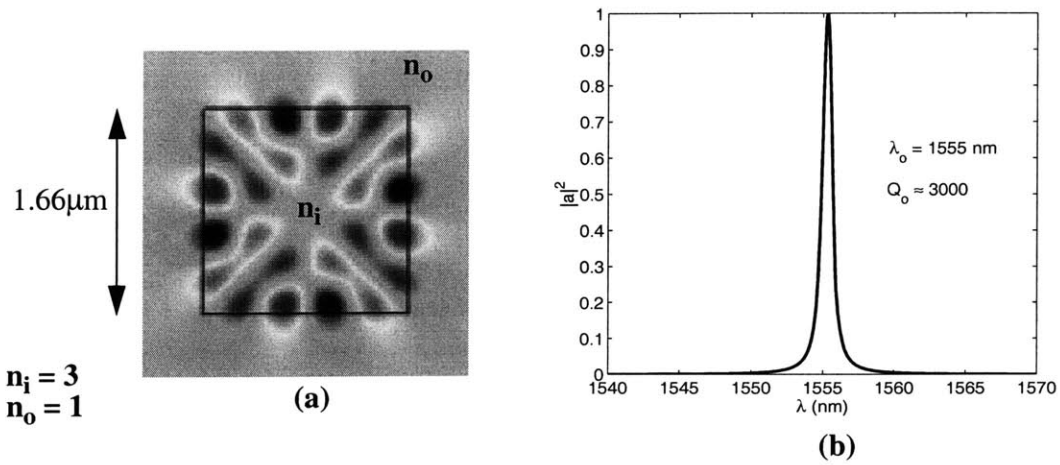

Figure 4.8: Electric field and spectrum of the square resonator used in the numerical examples.

In the following simulations we use a wideband source located at the bus waveguide, with spectrum centered at λ = 1550 nm, and the spatial profile of the fundamental waveguide mode at the center wavelength. The frequency response is obtained by DFT as explained in detail in section 3.5.

4.4.2 Single square resonator coupled with two waveguides

We start with a single square resonator placed symmetrically between two waveguides as shown in Figure 4.9(a). The edge-to-edge separation between waveguide and resonator, g, is varied between 0.2 and 0.26 μm. From the spectral response of this system we obtain the resonant wavelength and the quality factors associated with loss Q_o and external coupling Q_e. Because the evanescent coupling is mainly determined by the overlap of exponentially decaying fields in (2.54)-(2.55), we find that Q_e varies roughly exponentially as shown in the plot of Figure 4.9(b).

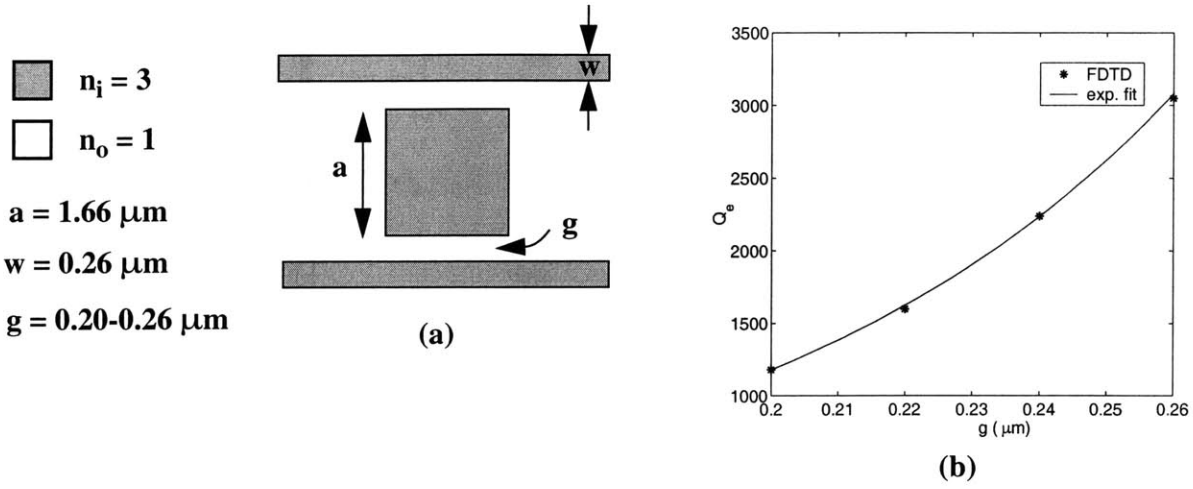

Figure 4.9: (a) Schematic of a square resonator evanescently coupled between two waveguides and (b) dependence of external Q on resonator-waveguide separation.

In Figure 4.10 we show the complete numerical results for g=0.24μm. From the electric field in (a) we can see that the cavity mode decays into the waveguides in all directions as expected for a standing wave mode. In (b) we show the spectral response obtained by FDTD and by CMT. For the latter we use (4.9)-(4.12) with $\lambda_o = \omega_o/2\pi = 1552\,\text{nm}$, $Q_e = Q'_e = 2240$ (extracted from the numerical data using (3.45)) and $Q_o = 3000$. In agreement with the theory presented in section 4.2 the output at all four ports is below 25%.

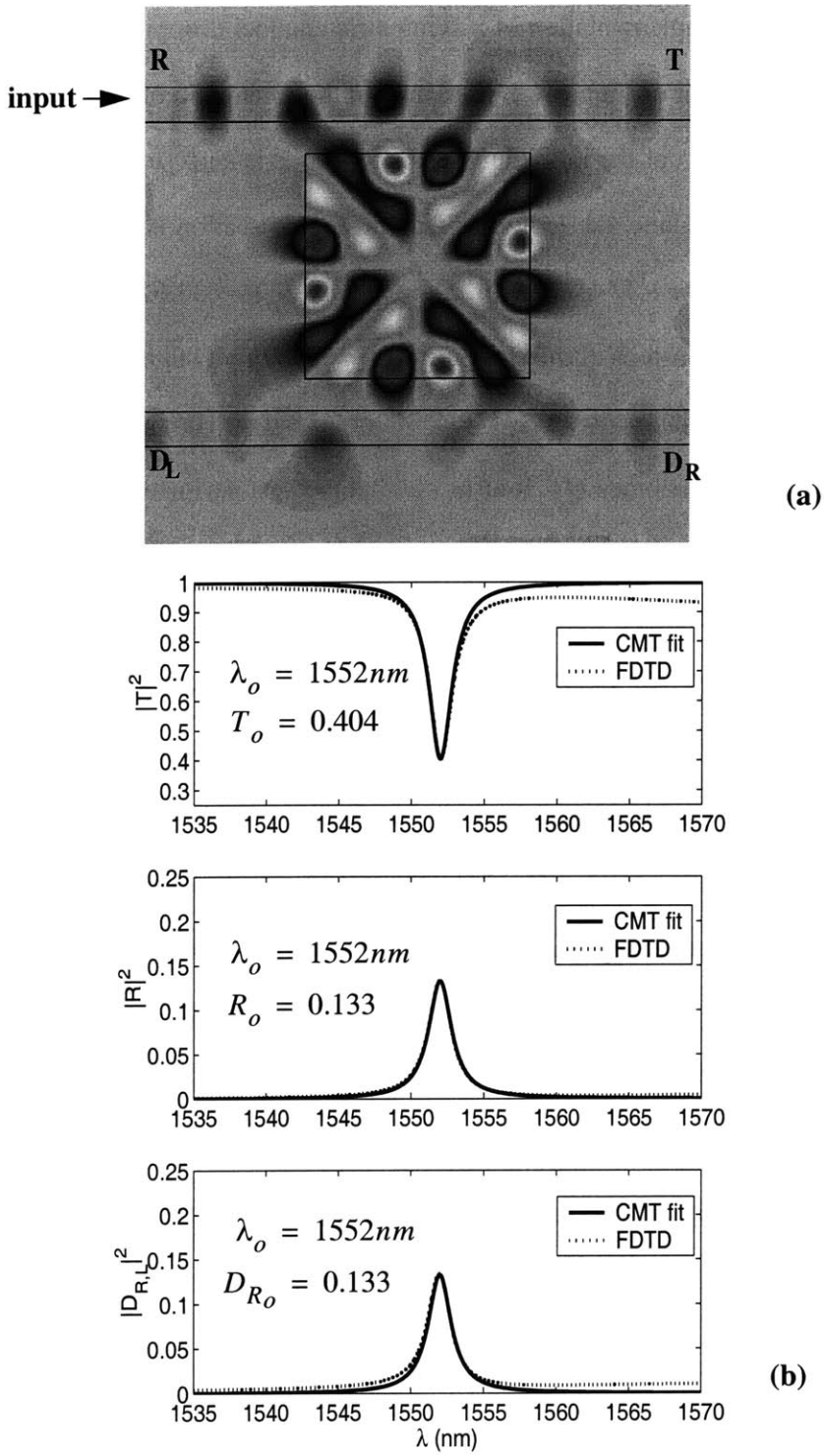

Figure 4.10(a) Electric field amplitude distribution in a four-port system consisting of a square resonator side-coupled to two waveguides. (b) Filter response calculated by FDTD (dotted line) and fitted by CMT.

4.4.3 Add/drop filter with a pair of square resonators

The next step is the implementation of a symmetric channel dropping filter with a pair of squares identical to that of Figure 4.8, as shown in the schematic of Figure 4.11(a). Since the electric field pattern of the individual resonator mode is antisymmetric with respect to its vertical symmetry plane, the length of the waveguide section between the two square centers must be $l = (m + 3/4)\lambda_g$ with $\lambda_g = \lambda_o / n_e(\lambda_o) \approx 633.62\,\text{nm}$. We choose m=3 as dictated by the dimensions of the structure so $l = 2.376\mu\text{m}$ but due to the 20nm spatial resolution in our simulations we use $l = 2.36$ or $2.38\ \mu\text{m}$. Having fixed l we vary the separation g which determines Q_e. It turns out that the best performance is achieved when $l = 2.36\mu\text{m}$ and g = 0.24μm which corresponds to $Q_e = Q'_e = 2240$. The filter response obtained by CMT under the assumption of perfect degeneracy when we set $Q_e = Q'_e = 2240$, $Q_o = 3000$ and $\lambda_o = 1552\,\text{nm}$ in (4.22)-(4.26) is shown in Figure 4.11(b).The coupling can be conveniently expressed by $Q_\mu \equiv \omega_o / 2\mu$ and for degenerate resonant frequencies in this example it is $Q_\mu = Q_e/2 = 1120$. The expected received at resonance dropped power is $(1 + Q_e/2Q_o)^{-2} = 0.53$ which corresponds to an insertion loss of 2.75dB, and the throughput is $[1 - (1 + Q_e/2Q_o)^{-1}]^2 = 0.074$. The total quality factor of the spectral response is $Q = (1/Q_o + 2/Q_e)^{-1} = 815.55$ which corresponds to a FHWM $\Delta f \approx 237$ GHz or $\Delta\lambda \approx 1.9\,\text{nm}$. This filter is too broad for realistic WDM systems, and its insertion loss is high because the resonator loss is comparable with the coupling to the waveguides. Better first-order responses can be obtained with low-loss resonators such as those of Figure 4.7; here the intend is to simply illustrate the ideas presented in the theory.

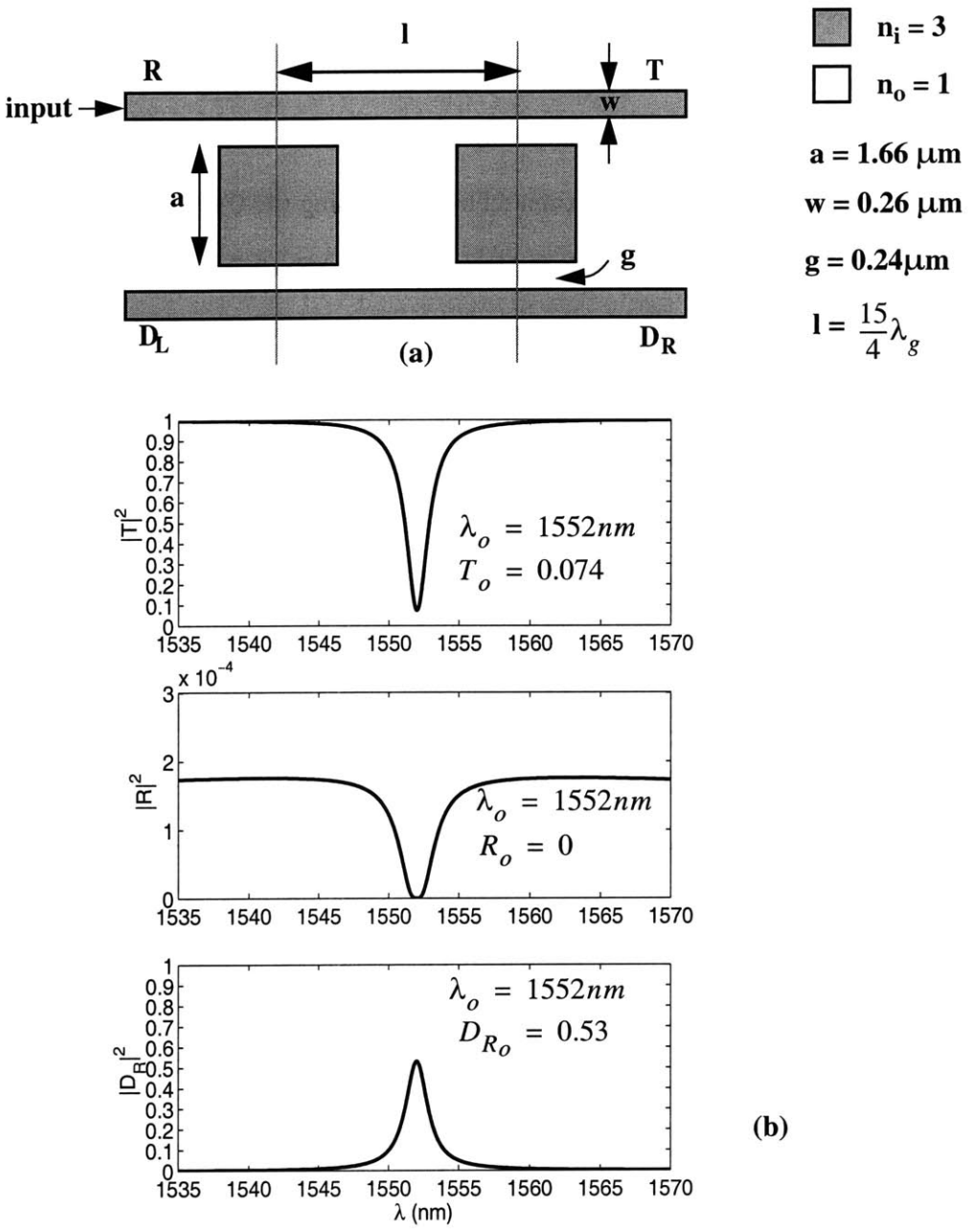

Figure 4.11: (a) Schematic of a symmetric channel dropping filter consisting of two identical square resonators (b) Theoretical response found by CMT.

The simulation results of Figure 4.12, suggest a deviation from the degeneracy conditions since there is a non-negligible residual reflection and back-drop visible in the field pattern in (a). In addition, the peak received power is slightly reduced and the throughput on resonance slightly increased relative to the expected values. In Figure 4.12(b) the numerical response has been approximated by CMT using (4.40)-(4.42) in (4.23)-(4.26). We used $l = 2.36\mu\text{m}$, which already is 16nm smaller than needed for a $\pi/4$-phase shift, Q's and λ_o as above, and the remaining splitting of the resonance frequencies was best matched by $Q_\mu = Q_e/2 + 325 = 1445$. Any remaining discrepancies may be due to possibly different radiation losses for the symmetric and antisymmetric modes.

It is clear that this type of filter is very sensitive to fabrication errors as small as our FDTD mesh resolution. This is true especially when the filters are implemented with conventional high index-contrast waveguides and resonators, evanescently coupled to one another, because of their high dispersion and the exponential dependence of the external coupling on the distance between them. Photonic crystal add/drops have more degrees of freedom for tuning the frequencies and the couplings [43],[44] and possibly better tolerance to fabrication errors [46].

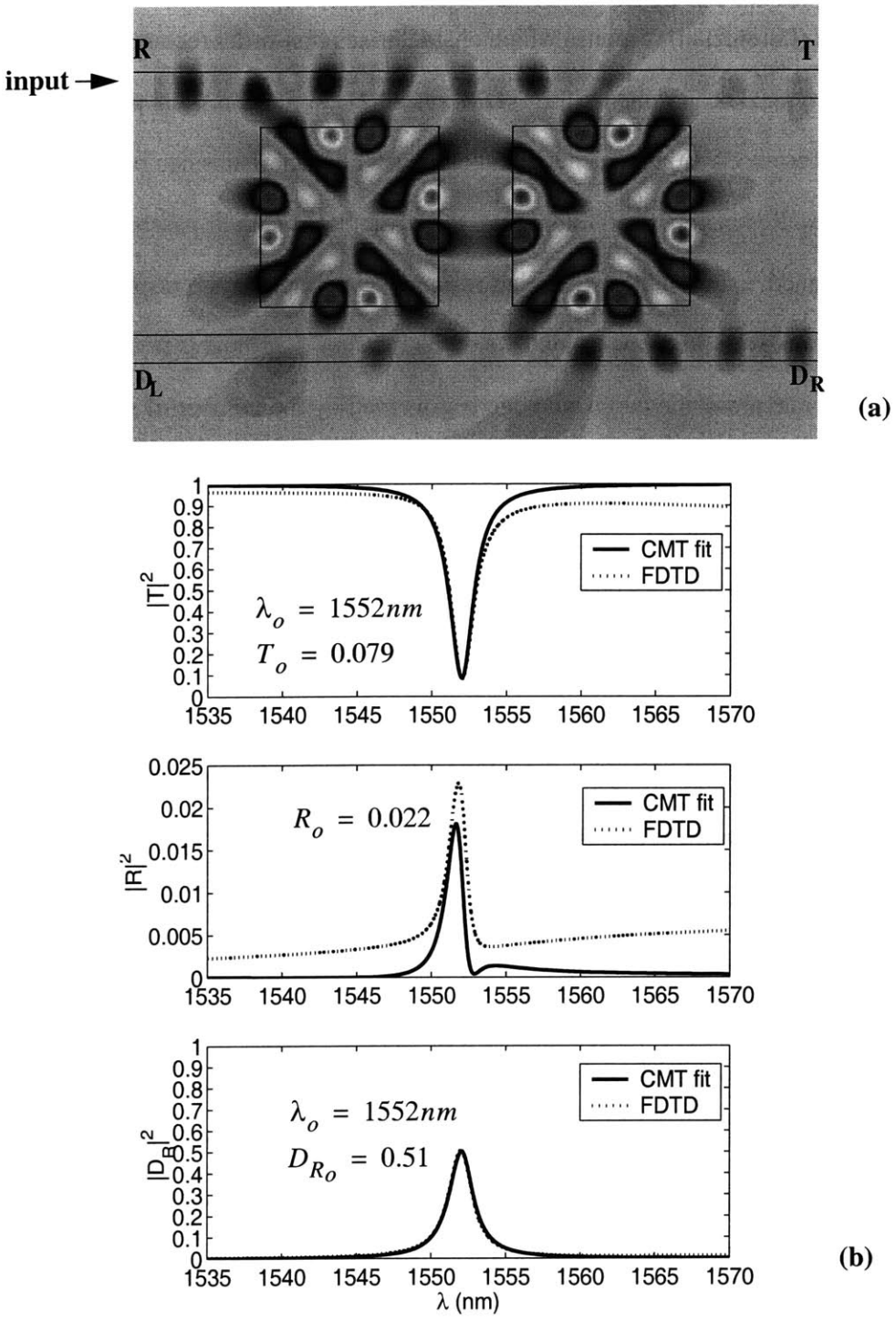

Figure 4.12: (a) Electric field amplitude distribution in a symmetric channel dropping filter using a pair of square resonators (b) Filter response calculated by FDTD and fitted by CMT.

4.5 High-order symmetric add/drop filters

The single-pole (Lorentzian) response which characterizes first-order resonant filters, cannot satisfy the typical requirements for WDM systems, i.e. flat-top filter passbands and less than -25dB crosstalk from adjacent channels. Such characteristics can be achieved by high-order filters. Resonator-based filters have the advantage that their passband shape can be custom designed, using multiply coupled resonators, to improve the response of a single resonator. Moreover, the response outside of the resonant passband is free of sidelobes, and the roll-off rate along the passband edge is governed by the number of mutually coupled resonators. The passband shape depends sensitively on the relative interactions among all resonators, and on their interactions with the waveguides. The coupling of modes in time can be simply extended to the case of higher order filters resulting in continued fraction expressions that provide a one-to-one correspondence with standard filter design parameters [34],[36],[48]. An equivalent circuit can thus be derived and a rough layout of the structure can be based on handbook filter designs of circuit theory.

An N-th order symmetric add/drop filter of the type described in section 4.3 can be implemented using N coupled pairs of identical resonators as shown in the schematic of Figure 4.13. This filter is again conveniently described in terms of the symmetric and anti-symmetric modes of the resonator pairs [48]. The degeneracy of these modes is required for channel add/drop operation. For the outermost pairs this is ensured again by mutual cancellation of the two coupling mechanisms: the mutual coupling between the resonators and their coupling through the bus (for pair 1) and through the receiver (for pair N). The For the i-th pair $i = 2, \ldots, N-1$, the degeneracy is ensured by placing the resonators far apart so they do not interact.

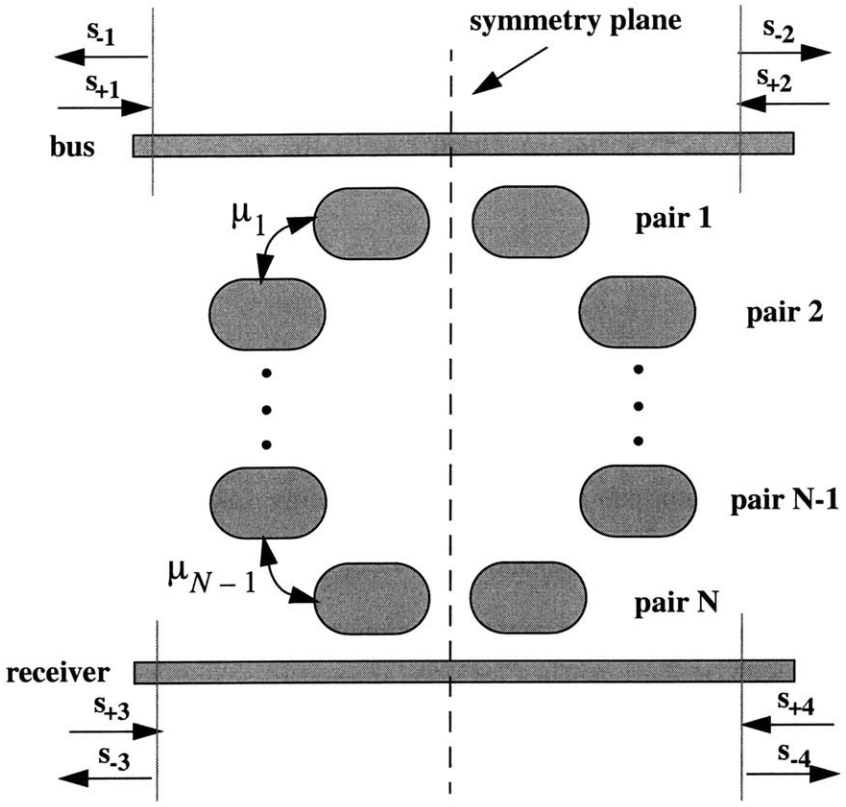

Figure 4.13: Schematic of an N-th order filter consisting of n pairs of identical standing wave resonators

The CMT equations for the symmetric and anti-symmetric modes of each resonator pair are:

$$\frac{da_{1s}}{dt} = \left(j\omega_{1s} - \frac{1}{\tau_{es}}\right)a_{1s} + \kappa_s(s_{+1} + s_{+2}) - j\mu_{1s}a_{2s} \tag{4.56}$$

$$\frac{da_{2s}}{dt} = j\omega_{2s}a_{2s} - j\mu_{1s}a_{2s} - j\mu_{2s}a_{3s} \tag{4.57}$$

$$\vdots$$

$$\frac{da_{Ns}}{dt} = \left(j\omega_{Ns} - \frac{1}{\tau'_{es}}\right)a_{Ns} + \kappa'_s(s_{+3} + s_{+4}) - j\mu_{(N-1)s}a_{(N-1)s} \tag{4.58}$$

$$\frac{da_{1a}}{dt} = \left(j\omega_{1a} - \frac{1}{\tau_{ea}}\right)a_{1a} + \kappa_a(s_{+1} - s_{+2}) - j\mu_{1a}a_{2a} \tag{4.59}$$

$$\frac{da_{2a}}{dt} = j\omega_{2a}a_{2a} - j\mu_{1a}a_{2a} - j\mu_{2a}a_{3a} \tag{4.60}$$

$$\vdots$$

$$\frac{da_{Na}}{dt} = \left(j\omega_{Na} - \frac{1}{\tau'_{ea}}\right)a_{Na} + \kappa'_a(s_{+3} - s_{+4}) - j\mu_{(N-1)a}a_{(N-1)a} \tag{4.61}$$

where a_{is}, a_{ia} represent the symmetric and anti-symmetric mode amplitudes, respectively, of the i-th resonator pair normalized to unit energy. Likewise, $\omega_{is,\,a}$ represent the resonance frequency of the i-th resonator pair, $1/\tau_{es,\,a}$, $1/\tau'_{es,\,a}$ are the associated decay rates and $\mu_{is,\,a}$ is the coupling between the symmetric and anti-symmetric modes, respectively of the i-th and i-th+1 resonator pair, real by power conservation. The symmetric modes do not couple to the anti-symmetric modes and vice versa. The coupling coefficients $\kappa_{s,\,a}$, $\kappa'_{s,\,a}$ have the form of equation (4.22). The outgoing waves are given by:

$$s_{-1} = e^{-j\beta d}(s_{+2} - \kappa^*_s a_{1s} + \kappa^*_a a_{1a}) \tag{4.62}$$

$$s_{-2} = e^{-j\beta d}(s_{+1} - \kappa^*_s a_{1s} - \kappa^*_a a_{1a}) \tag{4.63}$$

$$s_{-3} = e^{-j\beta' d}(s_{+4} - \kappa'^*_s a_{Ns} + \kappa'^*_a a_{Na}) \tag{4.64}$$

$$s_{-4} = e^{-j\beta' d}(s_{+3} - \kappa'^*_s a_{Ns} - \kappa'^*_a a_{Na}) \tag{4.65}$$

In this section we assume for simplicity that the coupling coefficients are real and we neglect the phase factors $e^{-j\beta d}, e^{-j\beta' d}$.With excitation $s_{+1} \sim e^{j\omega t}$ and $s_{+i} = 0,\ i = 2, \ldots, 4$ the mode amplitudes can be found as continued fractions from (4.56)-(4.61):

$$a_{Ns,\,a} = \frac{-j\mu_{(N-1)s,\,a}\,a_{(N-1)s,\,a}}{F_{Ns,\,a}} \tag{4.66}$$

$$a_{(N-1)s,\,a} = \frac{-j\mu_{(N-2)s,\,a}\,a_{(N-2)s,\,a}}{F_{(N-1)s,\,a}} \tag{4.67}$$

$$\vdots$$

$$a_{1s,\,a} = \frac{\kappa_{s,\,a}\,s_{+1}}{F_{1s,\,a}} \tag{4.68}$$

where $F_{is,\,a}$ are continuous fractions defined recursively as:

$$\begin{aligned}
F_{Ns,\,a} &= j(\omega - \omega_{Ns,\,a}) + \frac{1}{\tau'_{es,\,a}} \\
F_{(N-1)s,\,a} &= j(\omega - \omega_{(N-1)s,\,a}) + \frac{\mu^2_{(N-1)s,\,a}}{F_{Ns,\,a}} \\
F_{(N-2)s,\,a} &= j(\omega - \omega_{(N-2)s,\,a}) + \frac{\mu^2_{(N-2)s,\,a}}{F_{(N-1)s,\,a}} \\
&\vdots \\
F_{1s,\,a} &= j(\omega - \omega_{1s,\,a}) + \frac{1}{\tau_{es,\,a}} + \frac{\mu^2_{1s,\,a}}{F_{2s,\,a}}
\end{aligned} \tag{4.69}$$

Solving for $a_{Ns,\,a}$ we find:

$$a_{Ns,\,a} = \left(\frac{-j\mu_{(N-1)s,\,a}}{F_{Ns,\,a}}\right)\left(\frac{-j\mu_{(N-2)s,\,a}}{F_{(N-1)s,\,a}}\right)\cdots\left(\frac{-j\mu_{1s,\,a}}{F_{2s,\,a}}\right)\left(\frac{\sqrt{\frac{1}{\tau_{es,\,a}}}\,s_{+1}}{F_{1s,\,a}}\right) \tag{4.70}$$

We substitute the expressions for $a_{is,\,a}$ in (4.62)-(4.65) and the use definitions of the outputs $R \equiv s_{-1}/s_{+1}$, $T \equiv s_{-2}/s_{+1}$, $D_L \equiv s_{-3}/s_{+1}$, $D_R \equiv s_{-4}/s_{+1}$ to get:

$$R = -\frac{1}{F_{1s}\tau_{es}} + \frac{1}{F_{1a}\tau_{ea}} \tag{4.71}$$

$$T = 1 - \frac{1}{F_{1s}\tau_{es}} - \frac{1}{F_{1a}\tau_{ea}} \tag{4.72}$$

$$\begin{aligned} D_L = &-\left(\frac{-j\mu_{(N-1)s}}{F_{Ns}}\right)\left(\frac{-j\mu_{(N-2)s}}{F_{(N-1)s}}\right)\cdots\left(\frac{-j\mu_{1s}}{F_{2s}}\right)\left(\frac{\sqrt{\frac{1}{\tau_{es}\tau'_{es}}}}{F_{1s}}\right) \\ &+\left(\frac{-j\mu_{(N-1)a}}{F_{Na}}\right)\left(\frac{-j\mu_{(N-2)a}}{F_{(N-1)a}}\right)\cdots\left(\frac{-j\mu_{1a}}{F_{2a}}\right)\left(\frac{\sqrt{\frac{1}{\tau_{ea}\tau'_{ea}}}}{F_{1a}}\right) \end{aligned} \tag{4.73}$$

$$\begin{aligned} D_R = &-\left(\frac{-j\mu_{(N-1)s}}{F_{Ns}}\right)\left(\frac{-j\mu_{(N-2)s}}{F_{(N-1)s}}\right)\cdots\left(\frac{-j\mu_{1s}}{F_{2s}}\right)\left(\frac{\sqrt{\frac{1}{\tau_{es}\tau'_{es}}}}{F_{1s}}\right) \\ &-\left(\frac{-j\mu_{(N-1)a}}{F_{Na}}\right)\left(\frac{-j\mu_{(N-2)a}}{F_{(N-1)a}}\right)\cdots\left(\frac{-j\mu_{1a}}{F_{2a}}\right)\left(\frac{\sqrt{\frac{1}{\tau_{ea}\tau'_{ea}}}}{F_{1a}}\right) \end{aligned} \tag{4.74}$$

We next assume that the degeneracy of the resonant frequencies and decay rates for the two sets of modes is achieved by proper design and that all the cavities are identical, i.e.

$$\omega_{is} = \omega_{ia} \equiv \omega_o , \qquad i = 1, 2, \ldots, N \tag{4.75}$$

$$\begin{aligned} \tau_{es} &= \tau_{ea} \equiv \tau_e \\ \tau'_{es} &= \tau'_{ea} \equiv \tau'_e \end{aligned} \tag{4.76}$$

The vertical couplings between the resonator pairs can also be made degenerate, i.e.

$$\mu_{is} = \mu_{ia} \equiv \mu_i , \qquad i = 1, 2, \ldots, N-1 \tag{4.77}$$

It can be shown that this is possible only if there is no cross-coupling between resonators on either side of the symmetry plane that belong to different pairs. If (4.75)-(4.77) hold then from (4.69) we have $F_{is} = F_{ia} \equiv F_i$, $i = 1, 2, \ldots, N$ and equations (4.71)-(4.74) become:

$$R = D_L = 0 \tag{4.78}$$

$$T = 1 - \frac{2}{F_1 \tau_e} \tag{4.79}$$

$$D_R = -2\left(\frac{-j\mu_{(N-1)}}{F_N}\right)\left(\frac{-j\mu_{(N-2)}}{F_{(N-1)}}\right)\cdots\left(\frac{-j\mu_1}{F_2}\right)\left(\frac{\sqrt{\frac{1}{\tau_e \tau'_e}}}{F_1}\right) \tag{4.80}$$

The leading frequency term in the denominator is $(j)^N(\omega - \omega_o)^N$. Thus at high frequencies the transmission rolls off approximately as

$$|D_R| \approx \frac{\mu_1 \mu_2 \cdots \mu_{(N-1)} \sqrt{1/\tau_e \tau'_e}}{|\omega - \omega_o|^N} \tag{4.81}$$

as expected for an Nth-order filter. On resonance:

$$|D_R|^2 = \begin{cases} \dfrac{\mu_2^2}{\mu_1^2}\dfrac{\mu_4^2}{\mu_3^2}\cdots\dfrac{1}{\mu_{N-1}^2}\dfrac{1}{\tau_e \tau'_e} & \text{for } N \text{ even} \\ \dfrac{\mu_2^2}{\mu_1^2}\dfrac{\mu_4^2}{\mu_3^2}\cdots\dfrac{\mu_{N-1}^2}{\mu_{N-2}^2}\dfrac{\tau'_e}{\tau_e} & \text{for } N \text{ odd} \end{cases} \tag{4.82}$$

From (4.82) we can see that complete transfer of the channel power from the bus to the receiver is possible if

$$\frac{\mu_2^2}{\mu_1^2}\frac{\mu_4^2}{\mu_3^2}\cdots\frac{1}{\mu_{N-1}^2} = \tau_e \tau'_e \quad \text{for } N \text{ even} \tag{4.83}$$

$$\frac{\mu_2^2}{\mu_1^2}\frac{\mu_4^2}{\mu_3^2}\cdots\frac{\mu_{N-1}^2}{\mu_{N-2}^2} = \frac{\tau_e}{\tau'_e} \quad \text{for } N \text{ odd} \tag{4.84}$$

Moreover, it is possible to shape the frequency response e.g. to get a flat-top passband, by proper choice of τ_e, τ'_e and $\mu_i, i = 1, \ldots, N-1$. This task can get increasingly tedious as the filter order increases unless we are somehow able to map the coupled resonator system to a standard LC circuit. Then, the choice of design parameters is reduced to looking up tabulated impedance values in a standard filter design handbook. The detailed analysis can be found in [48]. Butterworth filter responses, characterized by maximally flat tops are of particular interest. The general form of the response at the receiver of an Nth order Butterworth filter is:

$$|D_R|^2 = \frac{1}{1 + A(\omega - \omega_o)^{2N}} \tag{4.85}$$

From this expression we find that in addition to (4.83)-(4.84) the following conditions must be satisfied:

$$\tau_e = \tau'_e \tag{4.86}$$

$$\sum_{i=1}^{N-1} \mu_i^2 = \frac{1}{\tau_e^2} \tag{4.87}$$

$$\mu_1 = \mu_N \quad \mu_2 = \mu_{N-1} \cdots \mu_{N/2-1} = \mu_{N/2+1} \quad \text{for } N \text{ even} \tag{4.88}$$

$$\mu_1 = \mu_N \quad \mu_2 = \mu_{N-1} \cdots \mu_{(N-1)/2} = \mu_{(N+1)/2} \quad \text{for } N \text{ odd} \tag{4.89}$$

N	μ_i
2	$\mu_1^2 = \frac{1}{\tau_e^2}$
3	$\mu_1^2 = \mu_2^2 = \frac{1}{2\tau_e^2}$
4	$\mu_1^2 = \mu_3^2 = \frac{-1+\sqrt{2}}{\tau_e^2}$ $\mu_2^2 = \frac{3-2\sqrt{2}}{\tau_e^2}$
5	$\mu_1^2 = \mu_4^2 = \frac{3-\sqrt{5}}{2\tau_e^2}$ $\mu_2^2 = \mu_3^2 = \frac{-2+\sqrt{5}}{2\tau_e^2}$

Table 4.1coupling coefficients for Butterworth filters

The coupling coefficients for flat-top response in the first few orders are shown in Table 4.1. The respective flat-top responses at the drop and throughput ports for a lossless filter with $Q_e = Q'_e = 2000$ are shown in Figure 4.14 where we can see that by increasing the filter order the passband edges become steeper reducing the crosstalk from adjacent channels. This is more clearly shown in dB scale. For this particular example the fourth-order filter leads to less than -25dB crosstalk 100GHz away from the center as required for 100GHz channel spacing. By contrast, the corresponding first-order filter has poor crosstalk performance even for 10 times the standard channel spacing.

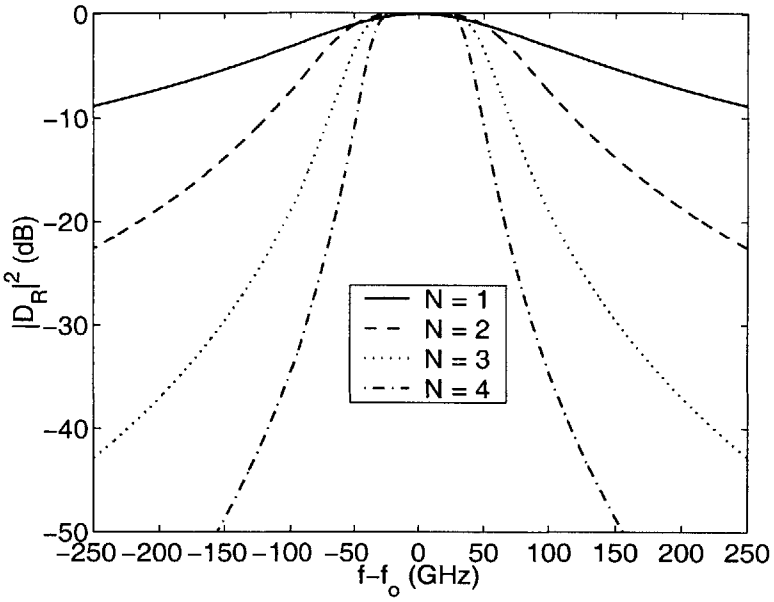

Figure 4.14: Example of drop response in dB calculated by CMT for different filter orders with $Q_e = Q'_e = 2000$ and negligible loss.

FDTD simulation

A numerical example of a second order filter using the same square resonators as before, is shown next. The filter is made up of four square cavities arranged in two pairs as shown in the schematic of Figure 4.15(a). The distance between the cavities in each pair is kept the same as in the first order filter to ensure that mutual coupling μ and the waveguide section length l remain the same. The additional design parameter is now the vertical distance l' which determines that vertical coupling μ_1. Now each resonator pair is evanescently coupled to only one waveguide therefore, twice the external coupling of the first order filter is required to cancel out the mutual couplings. This is most closely approached by reducing the resonator-square gap to $g = 0.2\mu$m. For this separation we have found $Q_e = 1185$ (Figure 4.9(b)). We plug this value into equations (4.71)-(4.74) along with the parameters of the first order filter, i.e. $l = 2.36\mu$m, $\lambda_o = 1552$nm, $Q_o = 3000$, and $Q_\mu = \omega_o/2\mu = 1445$ which again deviates from the exact value required for degener-

acy. For the vertical coupling we define $Q_{\mu_1} = \omega_o/2\mu_1$ and we set $Q_{\mu_1} = Q_e = 1185$ as required for $N = 2$. The resulting CMT prediction for the filter response is shown in Figure 4.15(b).

In the FDTD simulation the best response was obtained for $l' = 2.38\mu$m. The electric field and the filter response are shown in Figure 4.16. The numerical data agree mostly qualitatively with the CMT prediction with the greatest discrepancy in the received power, which is higher by 20% than expected. This suggests that at least some of the composite modes of the four squares have higher radiation Q's. The slight shift to longer resonant wavelength may be due to the presence of more dielectric. Note that because we chose to go from the first- to the second-order filter without changing l and μ we had to reduce Q_e by almost half to satisfy the degeneracy conditions, thus broadening the filter. Obviously for a narrower filter an entirely new design is required.

The difficulty of designing this type of filters using index guided structures as opposed to photonic crystal was even more pronounced in the high-order filters. For example in [45] much better responses were obtained when the same type of filter was implemented using photonic crystal microcavities. On the other hand we have basically demonstrated the validity of the theory.

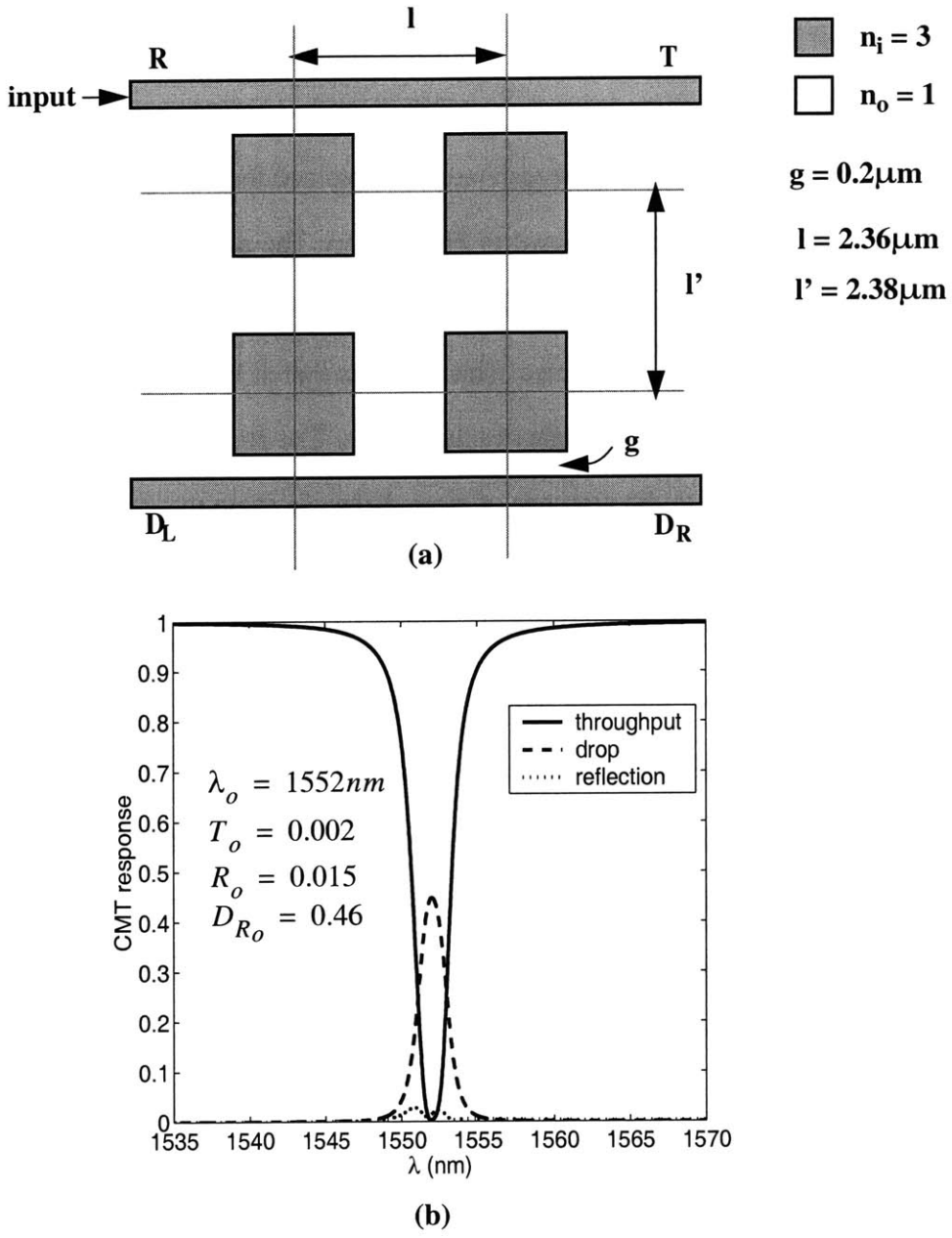

Figure 4.15: (a) Schematic of a second-order filter made up of square resonators (b) Filter response predicted by CMT.

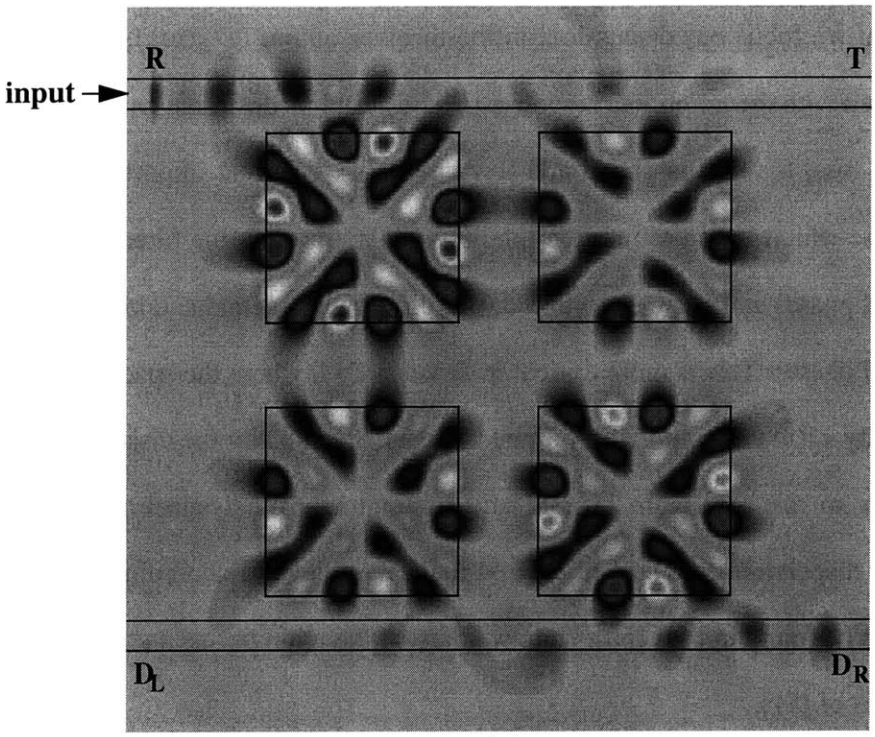

(a)

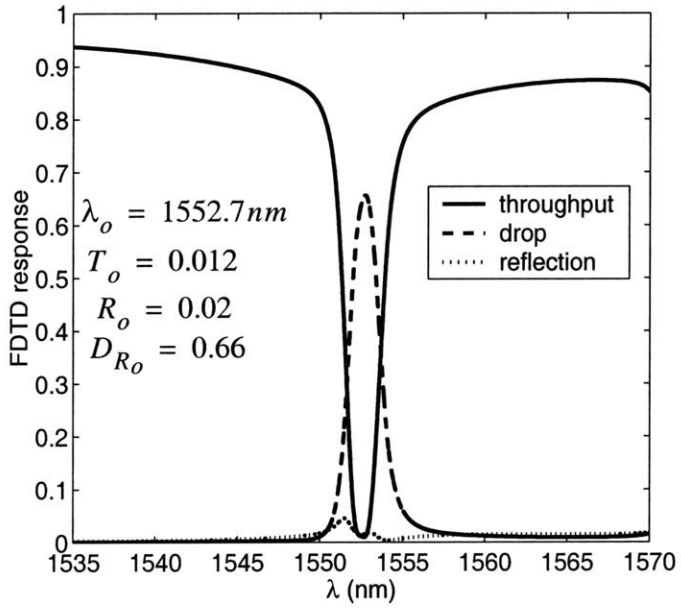

(b)

Figure 4.16: (a) Electric field amplitude in a 2nd-order filter consisting of two pairs of square resonators (c) filter response obtained by FDTD

4.6 Phase response and dispersion

In this section we focus our discussion on the receiver output ($D_R(\omega)$). So far we have been concerned with the amplitude response $|D_R(\omega)|$ and its desirable characteristics (i.e. low insertion loss, flat-top passband and low crosstalk). Of great importance is also the phase response which is determines the total time delay through the filter (first derivative of the spectral phase) and pulse distortion due to dispersion (second and higher derivatives of the spectral phase). This is more critical in dense WDM, where the spacing of the channels is typically <100 GHz, and high-bit rate systems. Specifically the dispersion of the filter sets limits to the maximum bit-rate and minimum channel spacing. An extensive discussion of dispersion in WDM filters and their classification according to their phase properties can be found in [49],[50]. Here we present the main points and examples based on the analysis of [51].

Resonator-based add/drop filters fall in the category of minimum-phase filters (MPF). In MPFs the amplitude response uniquely determines the phase response and vice versa, through a linear transformation, known as the Hilbert transform (also known as Kramers-Kronig relations). By contrast, in non-MPFs (such as WGRs and other MZI-based filters) this transform cannot be applied and the phase can be shaped independently of the amplitude. The main consequence of the unique relation between amplitude and phase in MPFs is that squaring the amplitude response to meet the flat-top and roll-off requirements comes at the price of increased phase distortion. In particular, it has been shown that the phase response is related to the slope of the amplitude response: the phase is approximately linear with frequency when the amplitude in constant whereas when the amplitude response changes radically (e.g., near the passband edges of a squared response), the phase will change correspondingly going from the approximately linear phase to one containing higher order terms leading to dispersion. This behavior can be avoided in non-

MPFs where the ideal amplitude response can be achieved while maintaining a linear phase.

The system function $H(s)$ of a MPF (in our filters $H(s) \equiv D_R(s)$) from which the frequency response is obtained for $s = j\omega$, has poles and no zeros in the right half s-plane. The presence of poles destroys the linearity of the spectral phase leading to dispersion. The filters of this chapter have an all-pole response, the number of poles being equal to the number of cavity pairs. Thus, increasing the number of cavities to steepen the amplitude spectrum, leads to increased dispersion at the filter edges.

The group delay is given by:

$$\tau_g(\Delta\omega) = \frac{\partial}{\partial(\Delta\omega)}\phi(\Delta\omega) \tag{4.90}$$

where $\phi(\Delta\omega)$ is the phase of the receiver response and $\Delta\omega = \omega - \omega_o$.

We illustrate the effects of quadratic dispersion of resonant CDFs to channels located close to the passband edge. We assume that the data stream in the bus is made up of Gaussian pulses with time dependence:

$$U(t) = \exp\left[-\frac{1}{2}\left(\frac{t}{\tau_o}\right)^2\right] \tag{4.91}$$

where τ_o is the half-width at the $1/e^2$ intensity point, related to the FWHM intensity by $\tau_{FWHM} = 2\sqrt{\ln 2}\tau_o$. A good measure of the dispersion is the critical pulse width:

$$\tau_c(\Delta\omega) = \left|\frac{\partial^2}{\partial(\Delta\omega)^2}\phi(\Delta\omega)\right|^{1/2} \tag{4.92}$$

If the initial pulse width of a transform-limited input Gaussian pulse is $\tau_o = \tau_c$ the pulse will emerge at the filter output broadened by a factor $\sqrt{2}$. For a transform-limited Gaussian pulse passing through the filter, the quadratic dispersion-induced pulse broadening factor is given by [52]:

$$\sigma = \left[1 + \left(\frac{\tau_c}{\tau_o}\right)^4\right]^{1/2} \tag{4.93}$$

From this relation, we see that τ_c should be made as small as possible and also that for $\tau_o > 2\tau_c$ the broadening is negligible (less than 3%). A small τ_c can be obtained by reducing the sharpness of the band-edge i.e. using a lower-order filter, which is in conflict with the requirement for a flat-top spectrum and low-crosstalk which is achieved by increasing the filter order. A constraint on the minimum initial pulse width translates into an upper limit for the bit rate B due to the relation $B \approx q/\tau_{FWHM}$ where q is the duty cycle of the pulse train. For an initial pulse width $\tau_o \geq 2\tau_c$ we get an upper limit $B \approx q/(4\tau_c)$ for the allowed bit rate. Of course the limit that supersedes all these considerations is that the initial pulse spectral bandwidth has to be smaller than the channel bandwidth Δf. For a transform-limited Gaussian pulse this can be written as [51]:

$$B < \frac{1}{\pi\tau_o} < \Delta f \tag{4.94}$$

In Figure 4.17 we show the amplitude response, the corresponding group delay, and the critical FWHM pulse width for high-order resonant CDFs with the same parameters as in Figure 4.14. In this example the filter with $N = 3$ does not meet the -25dB crosstalk requirement for 100GHz channel-spacing, the filter with $N = 4$ is well within the this requirement, while the filter with $N = 5$ would be better suited for denser channel-spacing e.g. 50GHz. With a bit rate of 10Gb/s per channel achieved using pulses with initial pulse width $\tau_{FWHM} = 25\,\text{ps}$ (well within the limit set by (4.94)) and $q = 25\,\%$ we find from (4.93) that the maximum pulse broadening is about 1.1% for $N = 3$, 9.35% for $N = 4$, 45% for $N = 5$ which is clearly unacceptable. This example clearly illustrates the conflict between the different system requirements when resonant filters are used.

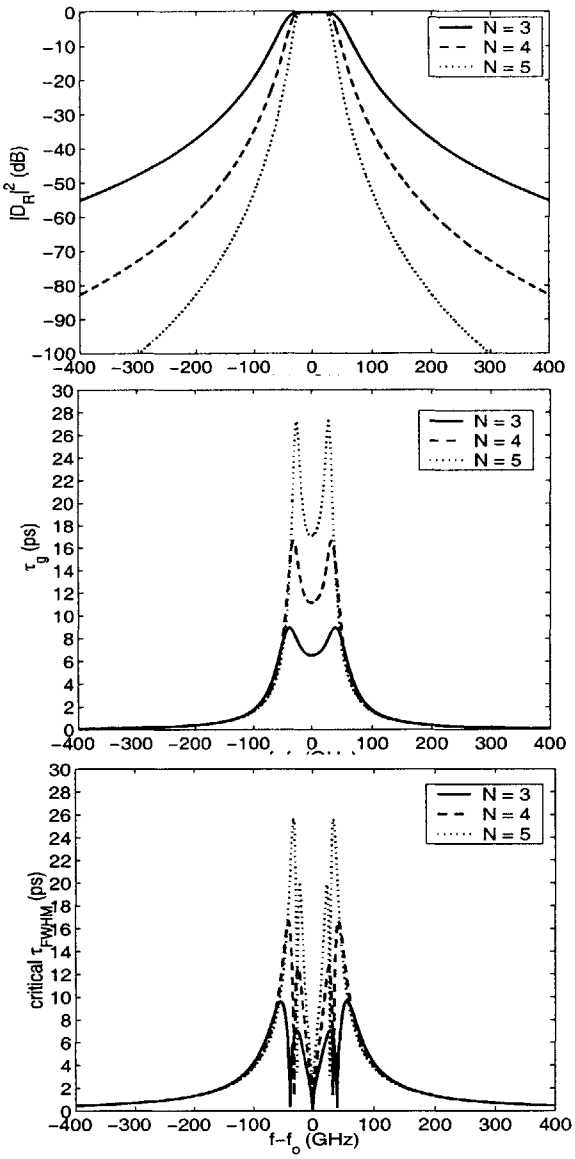

(a)

(b)

(c)

Figure 4.17: (a) Amplitude response (b) group delay (c) critical FWHM pulse width for high-order resonant filters with $Q_e = Q'_e = 2000$ and negligible loss.

The constraints imposed by the dispersion become stricter when we consider super-Gaussian pulses with time-dependence:

$$U(t) = \exp\left[-\frac{1}{2}\left(\frac{t}{\tau_o}\right)^{2m}\right] \tag{4.95}$$

where $m > 1$. For high m the pulse better approximate the almost square pulses of NRZ systems. Now the critical pulse width is given by:

$$\tau_c(\Delta\omega) = \left[m^2 \frac{\Gamma\left(2 - \frac{1}{2m}\right)}{\Gamma\left(\frac{3}{2m}\right)} \right]^{1/4} \left| \frac{\partial^2}{\partial(\Delta\omega)^2} \phi(\Delta\omega) \right|^{1/2} \tag{4.96}$$

where $\Gamma(x)$ is the Gamma function. It is well known that super-Gaussian pulses not only broaden but also get distorted under the influence of quadratic dispersion [52] so now the broadening factor (4.93) refers to the root-mean-square (rms) pulse width. For $m = 1$ (Gaussian pulse) the pre-factor in (4.96) is 1 while for $m = 10$ (very close to square pulse) it is ~2.

In summary, as the channels are more densely spaced in a WDM system, they come closer to the filter band-edge, so the dispersion is higher, diverging as the band edge is approached. Higher dispersion leads to longer critical input pulse-widths and thus lower allowable bit rates. Reducing the critical pulse widths by using a lower order filter leads to slower roll-off at the band edge and thus degradation in crosstalk and flat-top characteristics. Therefore, the design of a high-order resonator-based filter calls for a compromise of conflicting system requirements.

Chapter 5

High density integrated optics

5.1 Introduction

The strong light confinement in high index-contrast structures allows the design of waveguide components that can perform complex waveguide interconnections within a small area. High-performance right-angle bends and waveguide crossings that rely on resonances have been demonstrated in the context of photonic bandgap structures [53],[54]. In this work, it is shown that by modifying the waveguide intersection regions into resonant structures with symmetry, right angle bends, T-junctions and crossings with excellent transmission characteristics are also possible using conventional single-mode high index-contrast waveguides [67]. These structures are viewed as two-, three-, and four-port resonant systems, respectively, connected to waveguides, and their behavior is explained using coupling of modes in time. Although valid only for weak coupling, such a model can still give an intuitive understanding of the operational principles. The basic idea relies on the fact that a lossless resonator with proper symmetry gives zero reflection and complete transmission on resonance. The presence of loss in the resonator causes reflection and lowers the transmission peak. This non ideal response can be improved by optimizing the coupling between the waveguide and the resonator modes. These theoretical predictions are qualitatively verified by numerical simulations.

5.2 Sharp right angle bends

Waveguide bends are basic structures for optical interconnects and therefore very important components in optical integrated circuits. Any abrupt directional change in dielectric waveguides causes a rotation of the phase fronts of the propagating modes. This perturbation causes mode conversion into unguided modes giving rise to radiation loss, mostly at

the outer side of the corner. This happens because at some radius x_R the exponential tail of the unperturbed mode must travel faster than light in the cladding, in order to keep up with the rest of the mode. Since this is impossible it is assumed that the light beyond x_R radiates into the cladding as shown in Figure 5.1 [7].

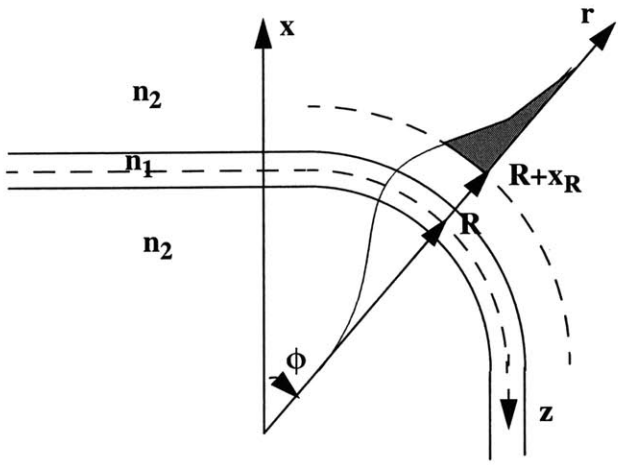

Figure 5.1: Radiation in a waveguide bend

Proposed methods for reducing the radiation loss in waveguide bends include decelerating the phase-front inside the abrupt bend[55], accelerating the phase-front outside an abrupt bend [56], adding a microprism in the bend region [57], replacing a bend with successive bends of smaller angle[58] or using a corner reflector [59]. Most of these studies were concerned with small-angle bends. For bends of larger angles corner reflectors have been proposed. Low-loss round 90^o -bends with small radius of curvature and wide angle splitters made of high index-contrast waveguides (Si/SiO2) have been reported in [60],[61]. Their performance relies on strong confinement in these waveguides.

In this section, we are concerned with ways to improve the performance of sharp bends which may be easier to fabricate than round bends. The performance of sharp 90^o -

bends in high index-contrast single-mode waveguides is greatly enhanced by placing a resonant cavity at the corner. A schematic of a simple waveguide bend is shown in Figure 5.2(a). The electric field in this bend and the transmission and reflection spectra are shown in Figure 5.2(b) and (c), respectively. Due to mode mismatch at the corner a large fraction of the power is lost to radiation or reflected backwards resulting in very poor transmission.

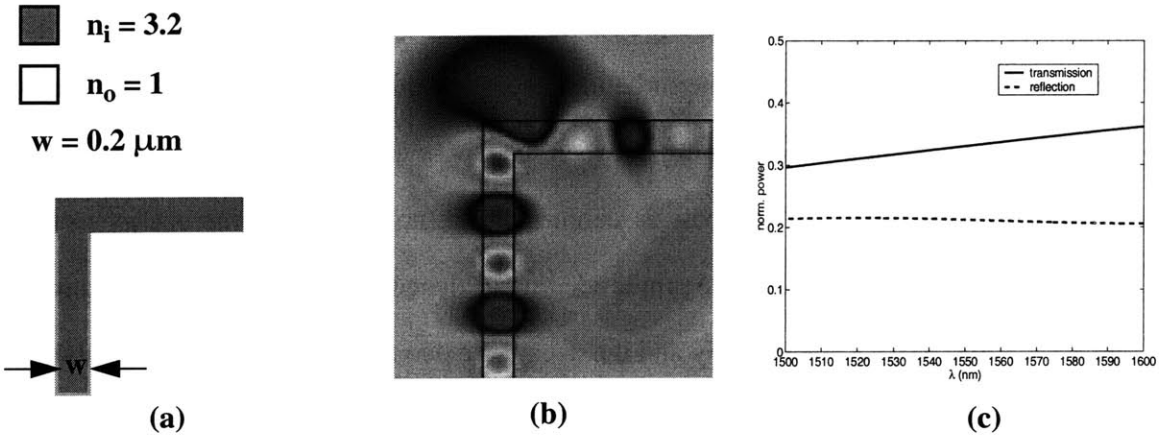

Figure 5.2: (a) Schematic of a sharp 90°-bend (b) electric field amplitude in the bend and (c) transmission and reflection spectra.

To improve the transmission through the bend we modify the corner region into a cavity as shown in the schematic:

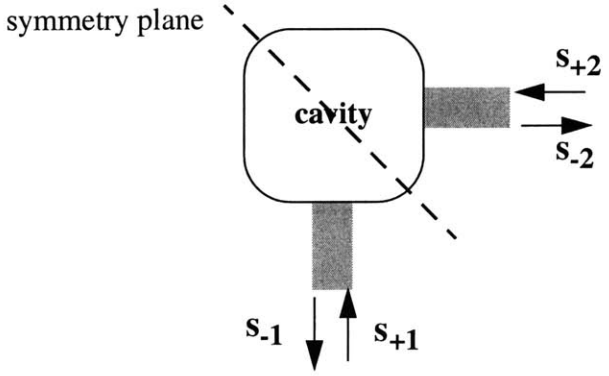

Figure 5.3: Schematic of a waveguide bend modified into a cavity.

The idea is based on the operating principle of a symmetric resonator with two ports[6]. At resonance, the transmission is complete with no reflection if the resonator is lossless. If this idea is applied to index-guided structures, radiation loss is unavoidable leading to nonzero reflection and reduced transmission. The effects of radiation can be counteracted by making the external of the resonator very small. This is achieved by strong coupling of the waveguide modes to the resonator mode. This concept is simply explained using the coupling-of-modes in time approach presented in section 2.5.2. Because this analysis is based on perturbation theory, it can only provide a qualitative prediction in the case of strong coupling between the cavity and the waveguide modes. The amplitude of the mode in the cavity is denoted by a, normalized to the energy in the mode, the decay rates of the mode amplitude due to the coupling to the two waveguides are $1/\tau_{e1}$ and $1/\tau_{e2}$, respectively and the decay rate due to loss is $1/\tau_o$. The incoming (outgoing) waves at the two ports are denoted by $s_{+1}(s_{-1})$ and $s_{+2}(s_{-2})$ and are normalized to the waveguide mode power. The coupling between the incoming waves and the resonator modes.is given by the coefficients κ_1, κ_2 related to the decay rates by

$$\kappa_1 = \sqrt{\frac{2}{\tau_{e1}}}e^{j\theta_1} \qquad |\kappa_2| = \sqrt{\frac{2}{\tau_{e2}}}e^{j\theta_2} \tag{5.1}$$

With inputs $s_{+1} \sim e^{-j\omega t}$ and $s_{+2} = 0$ at steady state we have:

$$a = \frac{\kappa_1}{j(\omega - \omega_o) + \frac{1}{\tau_o} + \frac{1}{\tau_{e1}} + \frac{1}{\tau_{e2}}} s_{+1} \tag{5.2}$$

$$s_{-1} = -s_{+1} + \kappa_1^* a \qquad s_{-2} = \kappa_2^* a \tag{5.3}$$

Using (5.1)-(5.3) we get:

$$\frac{s_{-1}}{s_{+1}} \equiv R = \frac{-j(\omega-\omega_o) - \frac{1}{\tau_o} + \frac{1}{\tau_{e1}} - \frac{1}{\tau_{e2}}}{j(\omega-\omega_o) + \frac{1}{\tau_o} + \frac{1}{\tau_{e1}} + \frac{1}{\tau_{e2}}} \tag{5.4}$$

$$\frac{s_{-2}}{s_{+1}} \equiv T = e^{j(\theta_1-\theta_2)} \frac{\frac{2}{\sqrt{\tau_{e1}\tau_{e2}}}}{j(\omega-\omega_o) + \frac{1}{\tau_o} + \frac{1}{\tau_{e1}} + \frac{1}{\tau_{e2}}} \tag{5.5}$$

At $\omega = \omega_o$ the reflection is zero and the transmission maximized if $1/\tau_{e1} = 1/\tau_{e2} + 1/\tau_o$. Thus, in symmetric, lossless system where $1/\tau_{e1} = 1/\tau_{e1} = 1/\tau_e$, and $1/\tau_o = 0$ we have complete transmission at resonance. The width of the frequency response is determined by $1/\tau_e$. If loss is present then the ratio $\tau_e/\tau_o = Q_e/Q_o$ determines the peak transmission and minimum reflection as:

$$|R|^2 = \frac{\left(\frac{Q_e}{2Q_o}\right)^2}{\left(1+\frac{Q_e}{2Q_o}\right)^2} \qquad |T|^2 = \frac{1}{\left(1+\frac{Q_e}{2Q_o}\right)^2} \tag{5.6}$$

A first attempt to apply this concept is an increase of the volume of dielectric at the corner region to form a square resonator as shown in Figure 5.4(a). The electric field pattern of the modified bend and the associated spectra, obtained by FDTD are shown in Figure 5.4(b),(c) respectively where we can see a marked reduction of the radiation loss compared with the plain bend but still poor transmission.

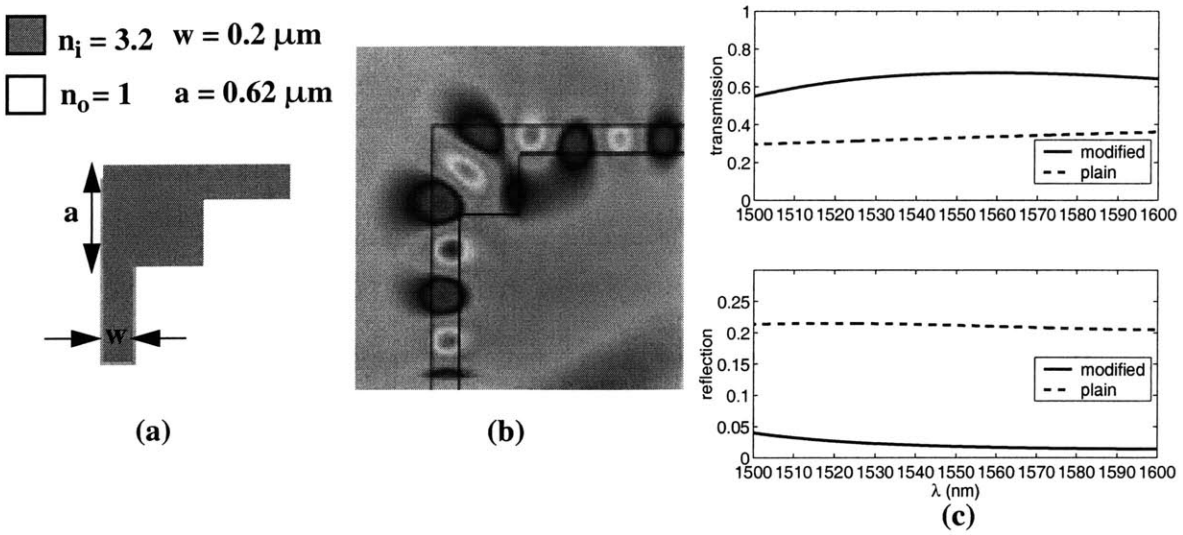

Figure 5.4: (a) Schematic of a modified bends (b) electric field and (c) associated transmission and reflection spectra, obtained by FDTD.

According to our previous discussion and equation (5.6), a further improvement of the performance is expected by increasing the coupling between the cavity and waveguide mode relative to the coupling to radiation. This can be achieved by pushing the cavity mode at the corner region inwards to get better mode matching, e.g. by making a cut as shown in Figure 5.5(a) and simultaneously adding more dielectric. The best response is obtained when the resulting structure is a quarter of an octagonal cavity (or any polygon cavity with fourfold symmetry) with "radius" a defined in the schematic. The simulation results in Figure 5.5(b) and (c) show that the radiation has been almost entirely suppressed and the transmission is close to 99% with negligible reflection. We shall use the name "High Transmission Cavity" (HTC) to describe this type of waveguide bends and other interconnecting components based on the same principle.

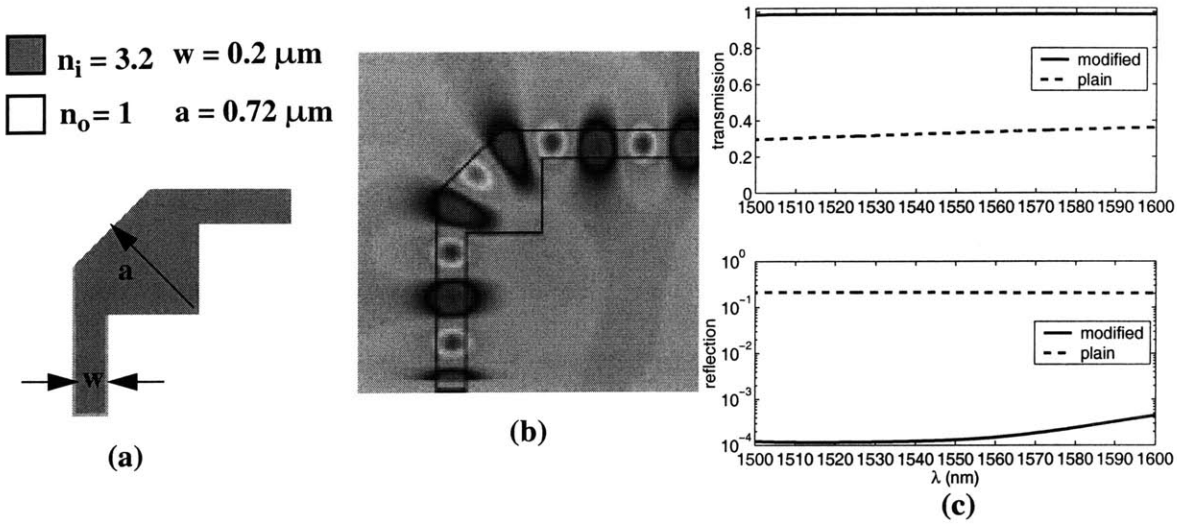

Figure 5.5: (a) Schematic of a bend modified into a quarter-octagon cavity (b),(c) Electric field amplitude and corresponding transmission and reflection spectra obtained by FDTD.

It is interesting to compare the performance of the HTC bend with a curved bend and a double bend of the same dimensions and in the same waveguides. In Figure 5.6 we can see that the of the two types of bends the curve one comes closer to the performance of the HTC bend than the double bend. However the performance if the HTC bend is still superior as this example illustrates.

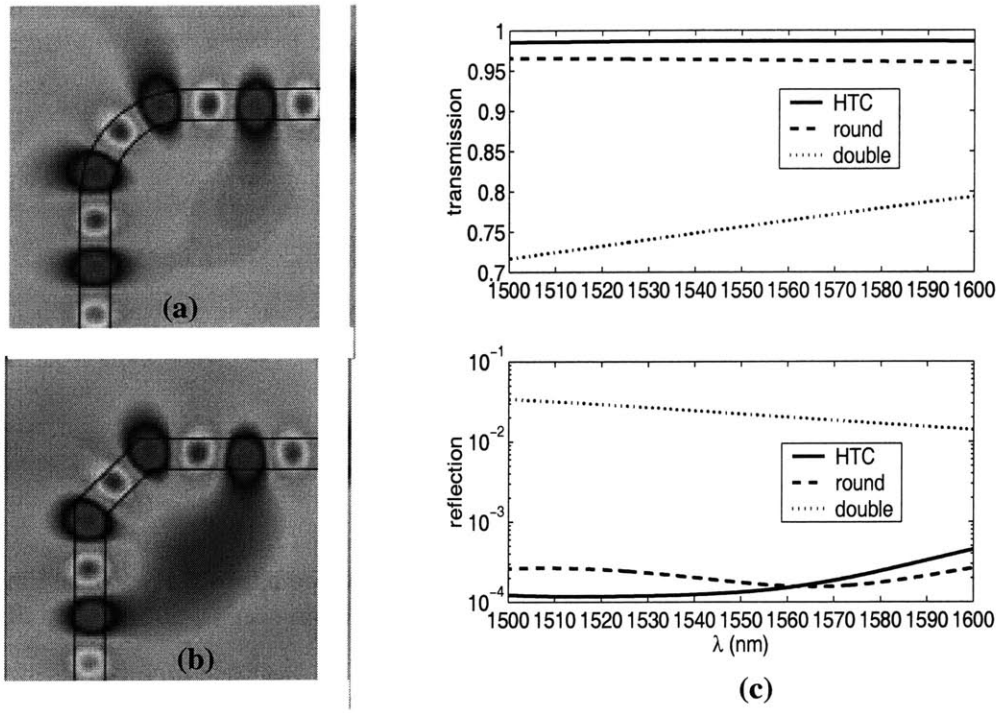

Figure 5.6: Electric field amplitude in (a) a curved bend and (b) a double bend (c) Comparison of the wavelength responses with that of a HTC bend of same dimensions

Next, we present further examples of this concept with different waveguide systems and quarter-polygon cavities, summarized in the schematics of Figure 5.7.

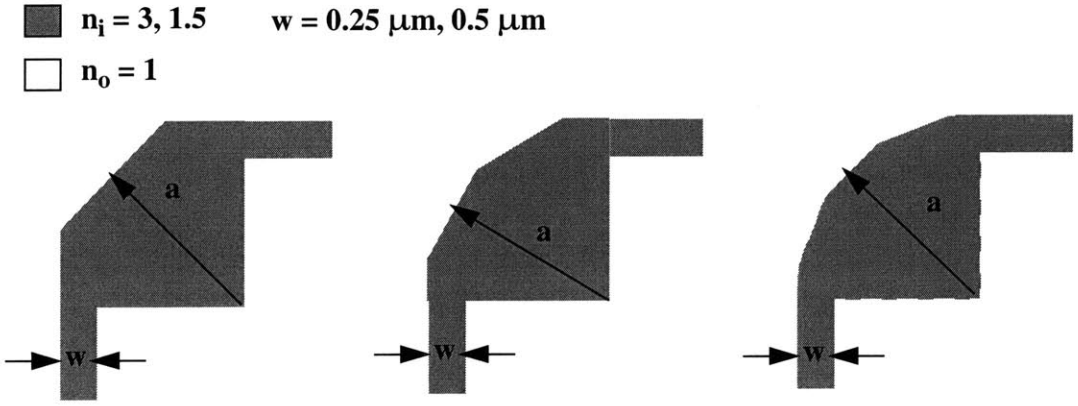

Figure 5.7: Schematic of HTC bends using quarter-polygons.

We examine two systems:

• A $3 \div 1$ index-contrast system that uses waveguides with $n_i = 3$ and $w = 0.25\mu m$. The effective index of the fundamental mode in 2D is $n_e \approx 2.45$ at $\lambda = 1550\,\text{nm}$.

• A $1.5 \div 1$ index-contrast system that uses waveguides with $n_i = 1.5$ and $w = 0.5\mu m$. The effective index of the fundamental mode in 2D is $n_e \approx 1.279$ at $\lambda = 1550\,\text{nm}$.

The electric field is polarized perpendicular to the paper (E_z) in all cases except when otherwise noted. We vary the radius a of the polygon in our FDTD simulations to get the highest possible peak transmission as close to $\lambda = 1550$ nm as our mesh resolution (20nm) allows. A very good initial guess for the radius a can be obtained by assuming that an integer number m of guided wavelengths $\lambda_g = \lambda / n_e$ fits in the polygon cavity with N sides from which the HTC is derived, along the dashed line in Figure 5.8. In this initial guess the effective index n_e of the connecting waveguides is used for better matching between resonator and waveguide mode. The effective index that corresponds to the mode inside the polygon cavity turns out to be slightly smaller as the mode field is displaced slightly outwards resembling a whispering gallery mode of a disk or ring cavity with the difference that here we have standing wave modes.

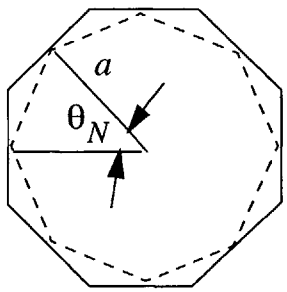

Figure 5.8: Reference for equation (5.7)

Referring to Figure 5.8 the estimated polygon radius is found from:

$$\left.\begin{aligned} N2a\sin\left(\frac{\theta_N}{2}\right) &= m\lambda_g \\ \theta_N &= \frac{2\pi}{N} \end{aligned}\right\} \Rightarrow \quad a = \frac{m\lambda_g}{2N\sin\left(\frac{\pi}{N}\right)} \tag{5.7}$$

3 ÷ 1 index contrast

Figure 5.9 shows the numerical results for examples of HTC bends and the associated polygon resonators obtained by FDTD for the $3 \div 1$ index-contrast system. Having established that the reflection is negligible in such bends, we show only the transmission plots, zooming in at the peak. Due to the very strong coupling between the waveguide the and HTC mode, which results in $Q_e \ll Q_o$ as previously discussed, this peak is very close to 1 and very broad so it is not discernible in a scale from 0 to 1. Similarly high transmissions can be obtained for different combinations of N and m.

As expected, the values for a that result in the best performance for given N and m close to 1550nm, correspond to $n_e < 2.45$, in (5.7).

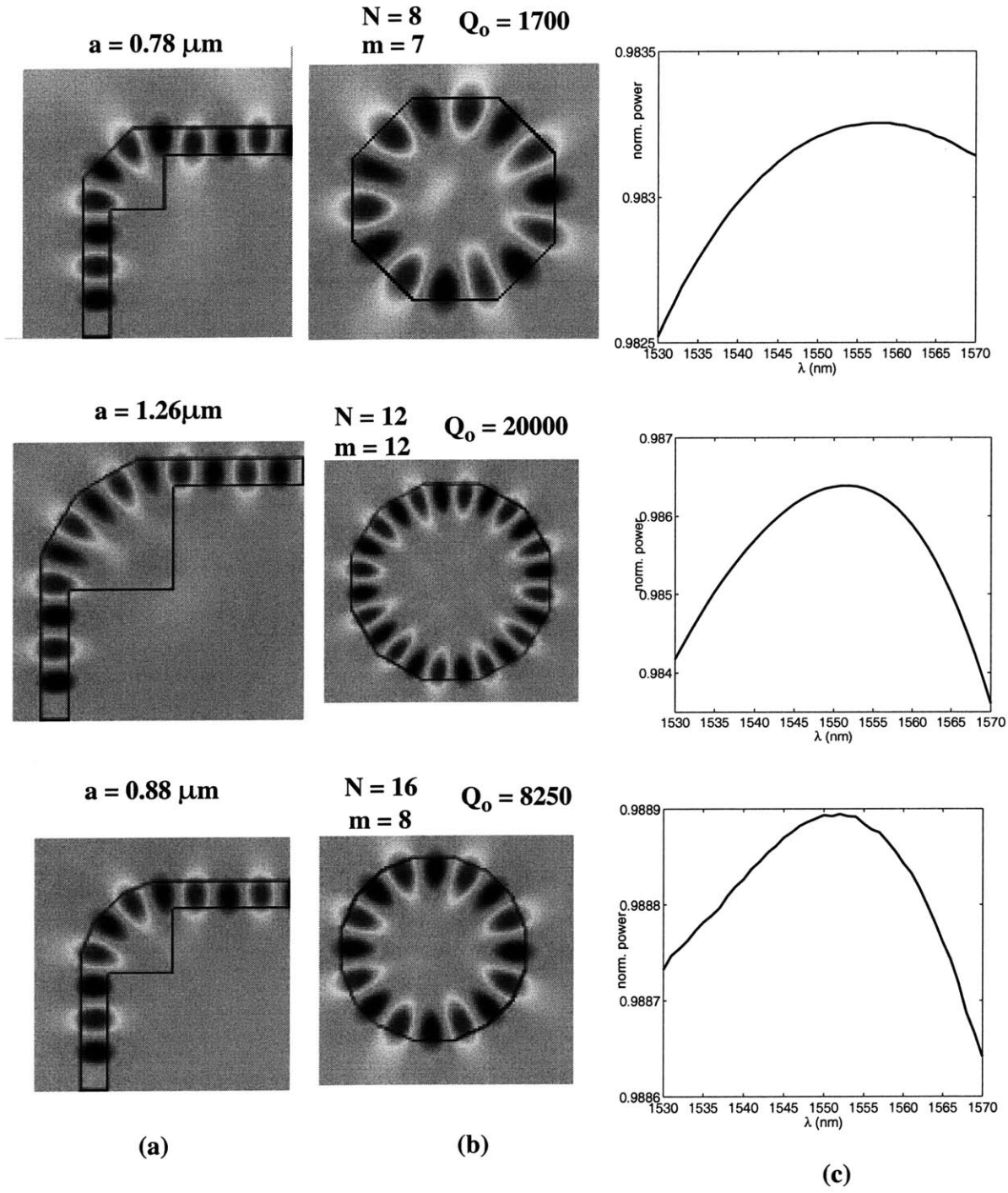

Figure 5.9: (a) Electric field amplitude in different HTCs, (b) the corresponding polygonic resonators, and (c) respective transmission spectra

A characteristic of such high index-contrast waveguide devices is their strong polarization dependence. We illustrate this with a simulation of the bend (a) in the orthogonal polarization H_z (the magnetic field is polarized perpendicular to the figure plane). The results are shown in Figure 5.10 There is a ~12.5% difference in the transmission between the two polarizations.

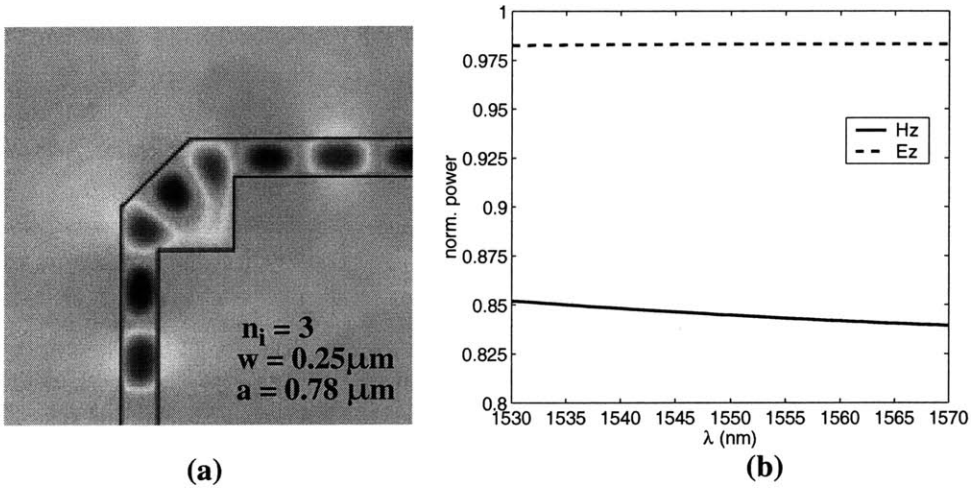

Figure 5.10: Polarization dependence of the first HTC bend of Fig. 5.9: (a) magnetic field (b) transmission response for the two polarizations.

An entirely new design is therefore needed in order to obtain a high performance HTC in this polarization, but the best achievable performance in a given waveguide system is expected to be lower compared with the E_z polarization.

1.5 ÷ 1 index contrast

The HTC concept can be applied to a lower index-contrast as well if the cavity is made large enough. Figure 5.11 shows the electric field and associated transmission spectrum for a quarter-octagon bend with approximately twice the size of that in Figure 5.9(a), i.e. scaled to the new index-contrast. Although the transmission is more than twice that obtained by a plain sharp 90^o bend in the same waveguide system, the transmission is still

very poor with half the power being lost to radiation as seen in (a).

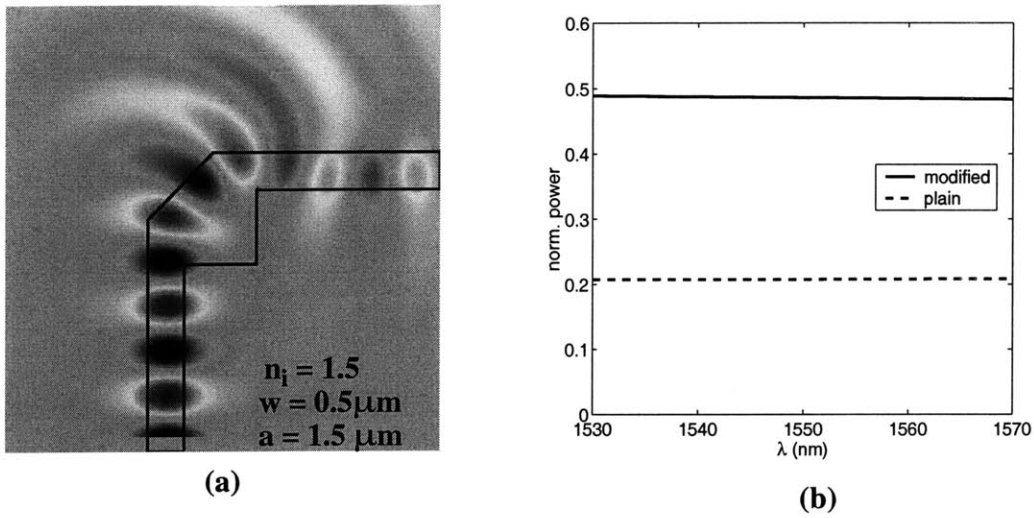

Figure 5.11: (a) Electric field and (b) transmission response in a quarter-octagon bend for 1.5/1 index contrast

More than 90% transmission is achievable in this lower index-contrast system as well using larger cavities derived from polygons with N=12 or 16. Two such examples are shown in Figure 5.12.

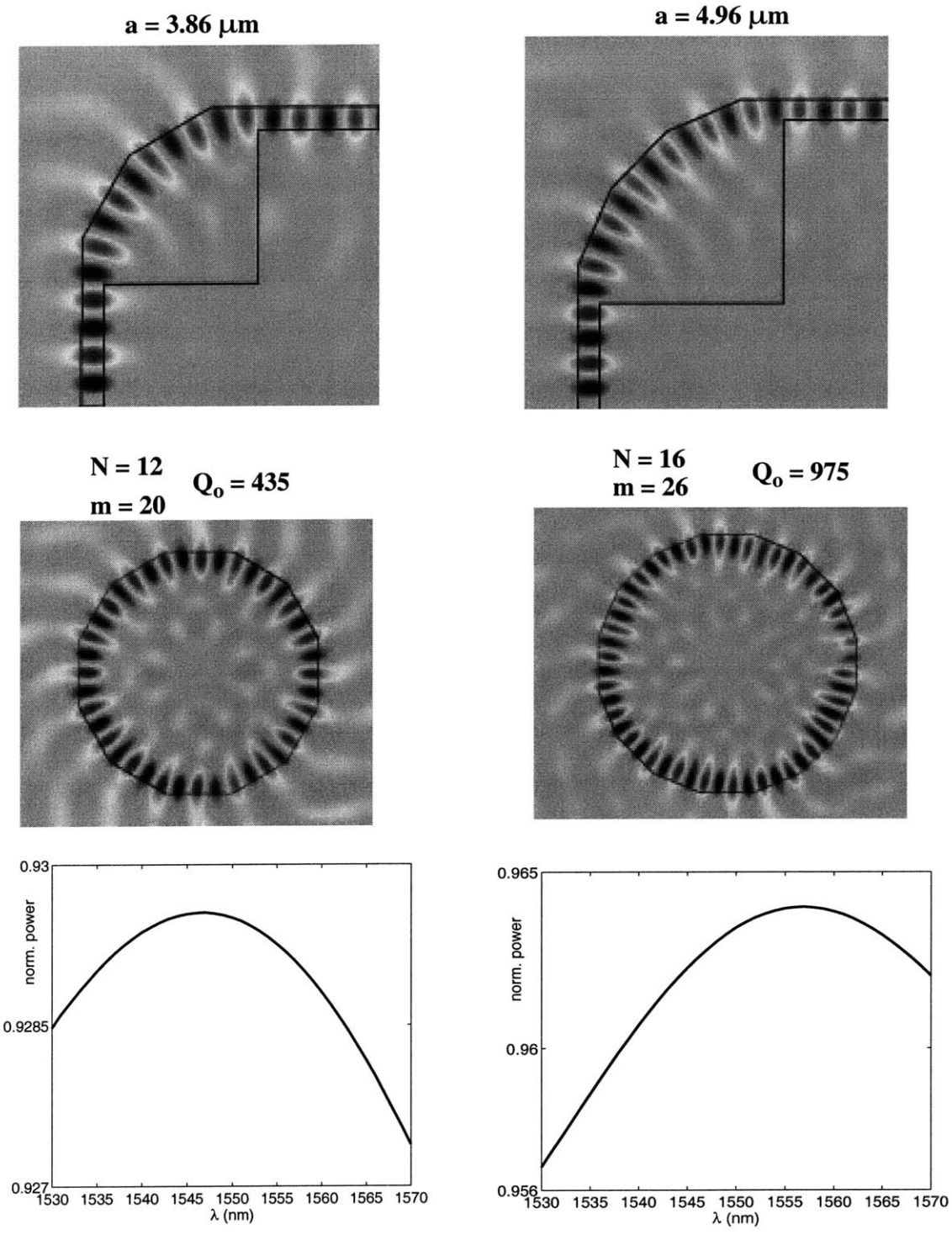

Figure 5.12: Electric field amplitude in two different HTCs, the corresponding polygons and respective transmission spectra

5.3 3D simulations and measurements of HTC bends

The 2D simulations presented so far served to illustrate the concept of the HTC bends and to show the dependence of the performance on cavity size and shape, index contrast and polarization. In a real 3D bend, part of the power may also leak into the substrate depending on the index-contrast. Obviously this is radiation loss cannot be seen in 2D simulations since the variation in the vertical dimension is ignored. In general, 3D FDTD simulations are extremely costly in time and memory for structures that extend by more than 1-2 μm in each direction and/or are highly resonant. HTC bends in high index-contrast are very small and have very broad transmission spectra, so a 3D analysis is possible.

In this section we perform 3D FDTD simulations for some of the bends that were fabricated at Lincoln Labs by Paul Maki and designed and tested by Desmond Lim at MIT [62]. We compare the numerical with the experimental data and with the results obtained combining 2D FDTD and EIM as described in section 2.4. Two material systems were used: polySi (n_i = 3.48) and silicon nitride (n_i = 2.4), both on SiO_2 substrate (n_s = 1.48) with air cladding (n_c = 1). The SEM of one of the polySi bends is shown in Figure 5.13 (a) and the model used as input in the FDTD simulations is shown in (b). The polySi waveguides are single-mode, have dimensions w = 0.5μm and h = 0.2μm and the preferred polarization of the electric field is in the plane of the bend system. The silicon nitride waveguides are single-mode, have dimensions w = 0.5μm and h = 0.8μm and the preferred polarization of the electric field is along the longest dimension, that is perpendicular to the plane of the bend.

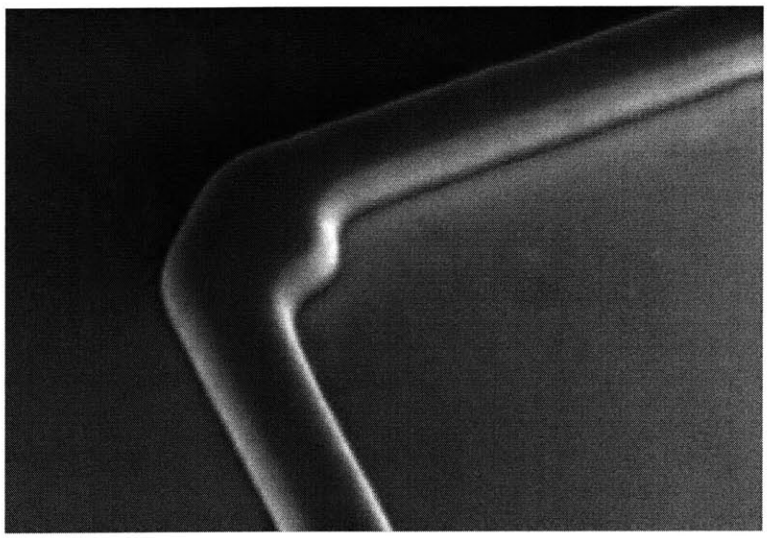

(a)

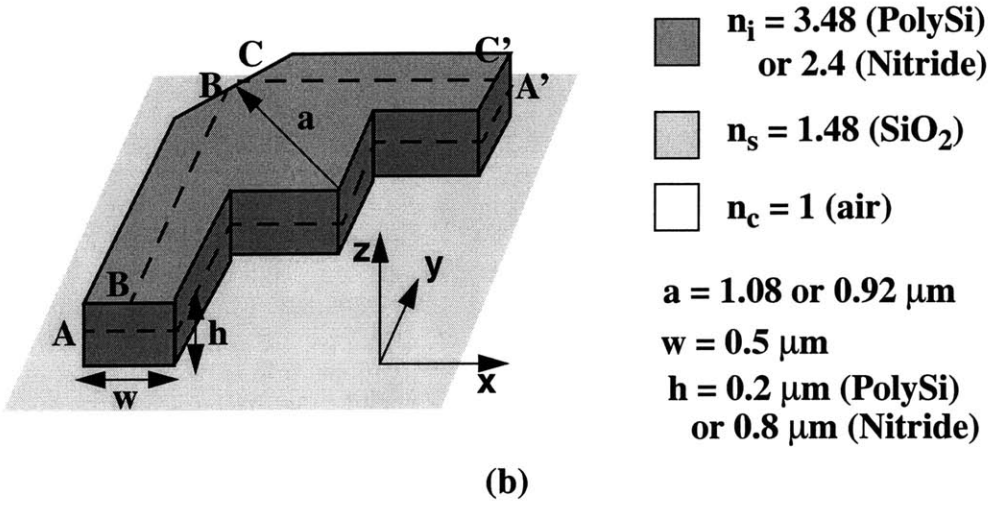

(b)

Figure 5.13: (a) SEM of HTC bend on polySi (from [62]) and (b) model used in 3D FDTD simulations

HTC bends in polySi

Figure 5.14summarizes our calculations for this system with the dimensions used in the fabrication. The best measurement was obtained for a = 1.08μm: The loss per turn found to be 0.38dB/turn corresponding to ~91.7% transmission. For a = 0.92μm the loss per turn

was 0.63dB/turn corresponding to ~86.5% transmission.

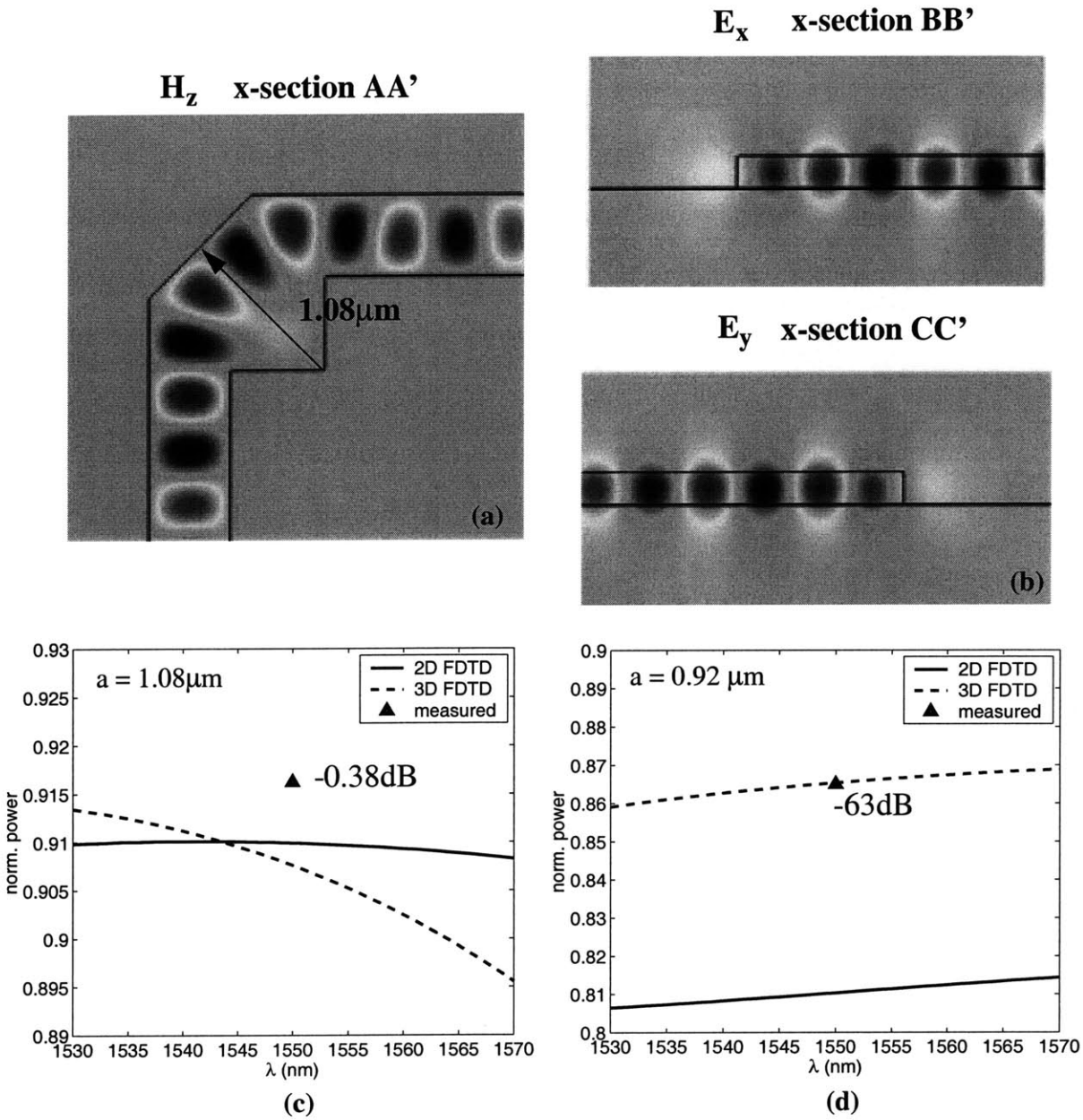

Figure 5.14: FDTD simulation of a polySi HTC bend: (a) magnetic and (b) electric field component along selected cross-sections for a = 1.08μm and (c),(d) transmission spectra for a = 1.08μm and 0.92μm, respectively.

In (a) and (b) we show the field patterns obtained by 3D FDTD, along characteristic cross sections of the best HTC case $a = 1.08\mu m$. In the top view (H_z) we can see that the field is well confined inside the cavity with one wavelength per side. The side views (E_x and E_y) confirm the fact that there is no power leaking into the substrate around the turn. In Figure 5.13(c) the transmission responses obtained by 3D and 2D FDTD are shown in comparison with the measurement. We note an excellent agreement between the numerical and experimental results as well as between the two simulation results. In (d) the same calculation was performed for the case a = 0.92μm. Again the 3D simulation result is in excellent agreement with the measurement but, surprisingly, the 2D simulation yields 5% lower transmission. A possible reason for this discrepancy is that a second mode is supported by the equivalent slab waveguide obtained by EIM for use in the 2D simulation (see discussion in Section 2.4).

We note that due to the high index-contrast and large aspect ratio (w/h) of the waveguide cross-section especially at the bend region (~1/0.2), the use of the opposite polarization results in very poor transmission, well under 80%, in agreement with the result shown in Figure 5.10.

HTC bends in silicon nitride

We first show an example of the significant deterioration of the performance if, while keeping all other design parameters the same as before, we lower the core index to $n_i = 2.4$. We examine the case with a = 1.08μm. In Figure 5.15(a) and (b) we can clearly see that radiation is escaping both sideways and into the substrate, respectively. The latter can only be seen by a 3D simulation. The transmission through the bend now is now in the 40-45% range which is almost 15% lower than the 2D prediction. This discrepancy is expected since the 2D cannot capture the radiation escaping to the substrate.

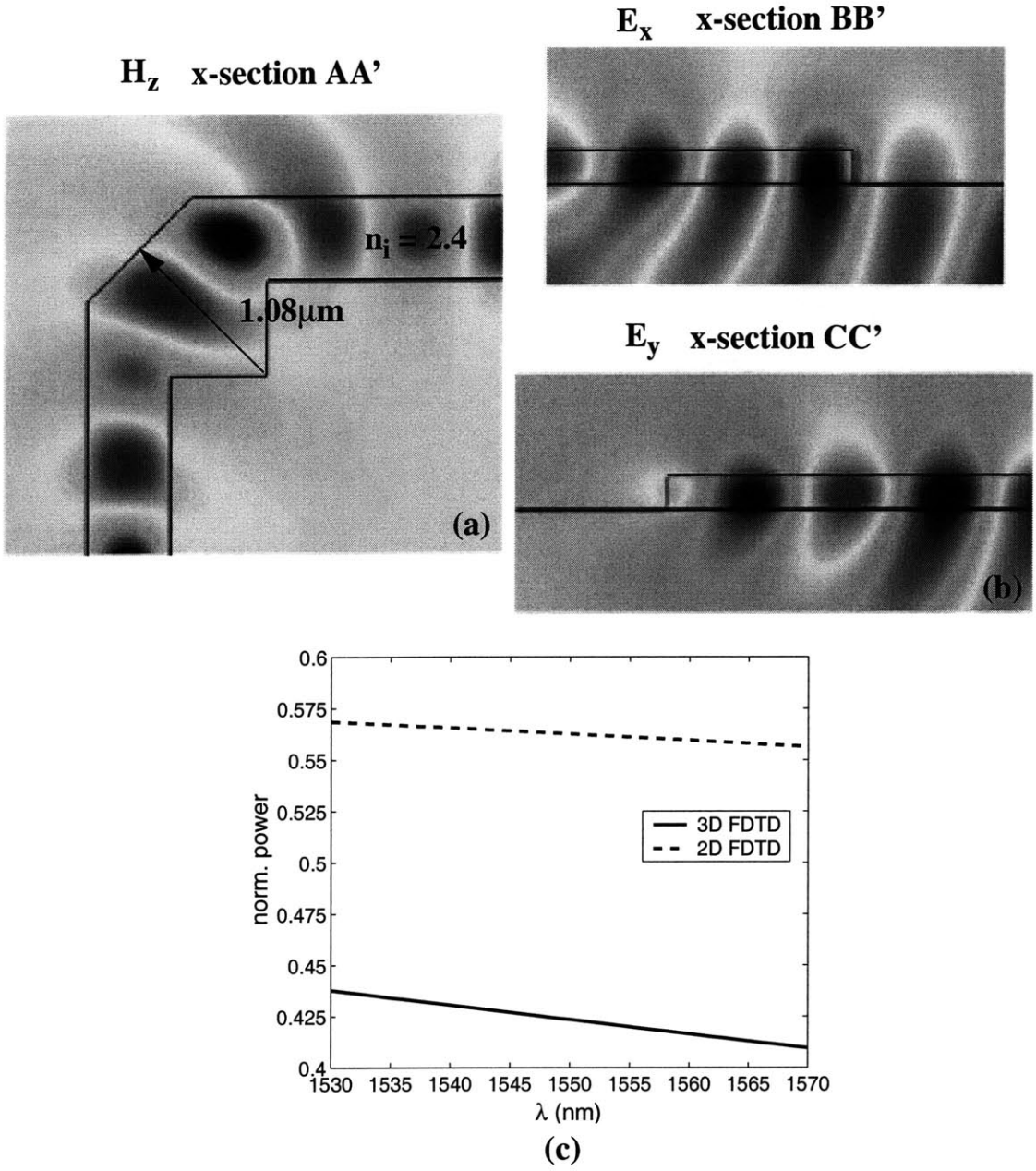

Figure 5.15: Example of a nitride bend with the design parameters of a polySi bend, showing radiation escaping to substrate: (a) magnetic and (b) electric field components along selected cross-sections and (c) transmission spectra obtained by 2D and 3D FDTD.

Figure 5.16 shows the numerical results for the HTC bends with silicon nitride waveguides that were fabricated and tested at MIT. Now the polarization is orthogonal to

that of the previous two cases. The radii these bends are the same as in the Si case, thus the performance is not the best possible with this system since, as we have shown, a change in the index and/or polarization requires an entirely new cavity design.

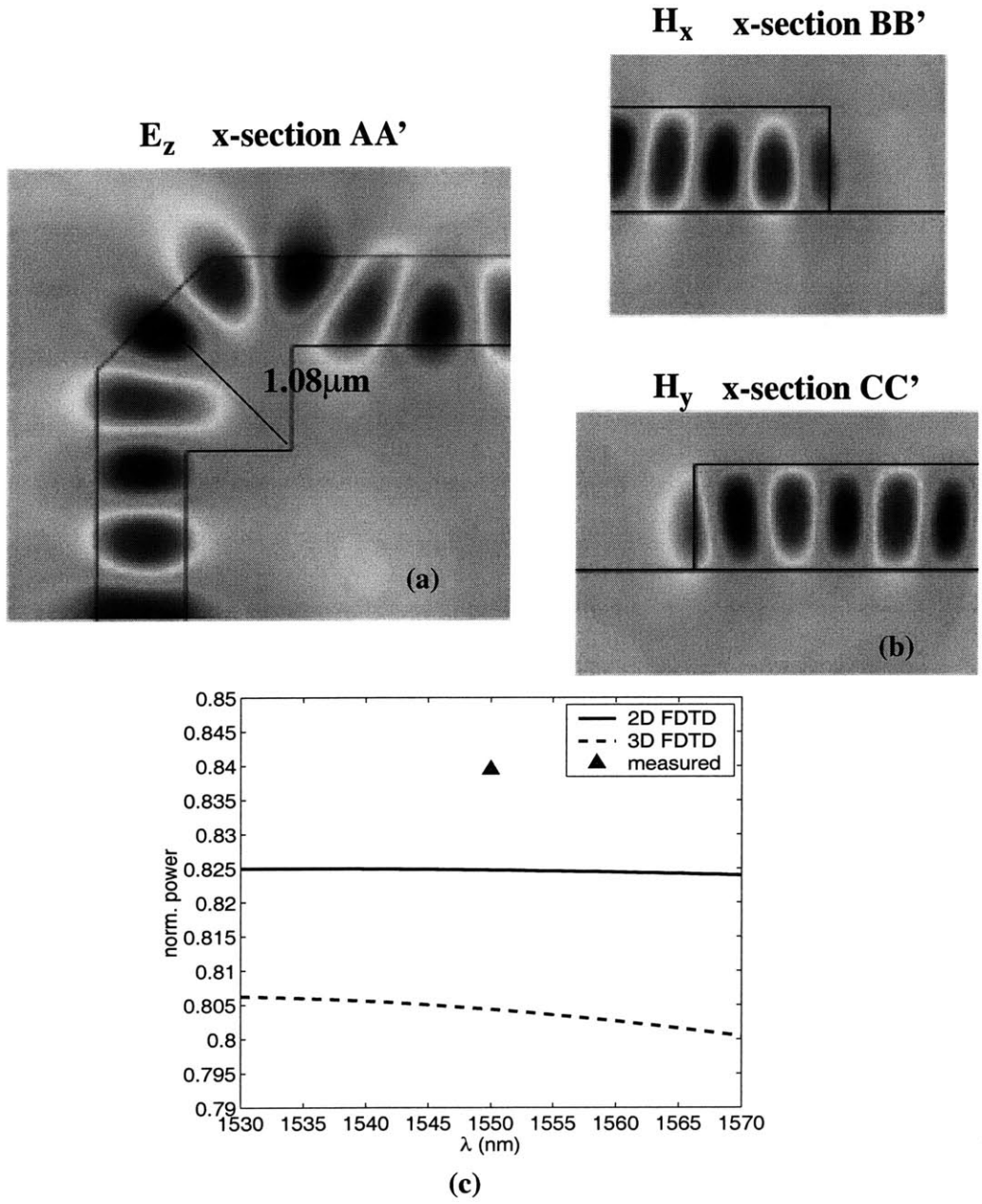

Figure 5.16: FDTD simulation of a nitride HTC bend: (a) electric and (b) magnetic field component along selected cross-sections for a=1.08μm , (c) transmission spectra.

We compare our numerical results with measurements for the case $a = 1.08\mu m$. The measured loss for this bend was 0.76 dB/turn corresponding to a ~84% transmission. The field patterns from the 3D FDTD in (a) and (b) verify that with the new waveguide dimensions and polarization, there is no visible leakage of the fields into the substrate in spite of the lower index-contrast. The transmission spectra are shown in (c) and compared to the measurement. The agreement between numerical and experimental data is fairly good although this time the 3D FDTD simulation has underestimated the transmission by about 3.5%. A possible explanation is that, trying to keep the computational domain as small as possible, the extent of the cross-section over which the transmitted power was calculated (see section 3.5) was not sufficient to capture the entire waveguide mode.

It is interesting to note that, using the orthogonal (TE) polarization in the FDTD simulations, the transmission is less than 3% lower than in the TM case corresponding to ~1dB loss. This is due not only to the lower index-contrast in the nitride system but also to the fact that the aspect ratio (w/h) of the waveguide cross-section (0.5/0.8) especially at the bend region (~1./0.8) is much closer to 1 than in the PoySi system.

5.4 T-splitters

A waveguide component useful for power splitting or combining is a T-splitter which is essentially a Y-branch of 90° half angle. Most studies in the literature have been concerned with the design of small-angle Y-branches that require large device lengths to achieve a low-loss transition to the two arms. Index or height tapering have been used for adiabatic mode evolution [63],[64], and integrated microprisms have been proposed for phase-front compensation in a scheme analogous to that employed for loss reduction in bends [65].

The HTC concept can be extended to the T-splitter using cavities similar shapes. The CMT in time formulation can also be applied to this case by treating the junction as a three-port system shown in Figure 5.17. For the third port we add the definition of the incoming (outgoing) waves $s_{+3}(s_{-3})$, the decay rate $1/\tau_{e3}$ and the associated coupling coefficient $\kappa_3 = \sqrt{2/\tau_{e3}}e^{j\theta_3}$.

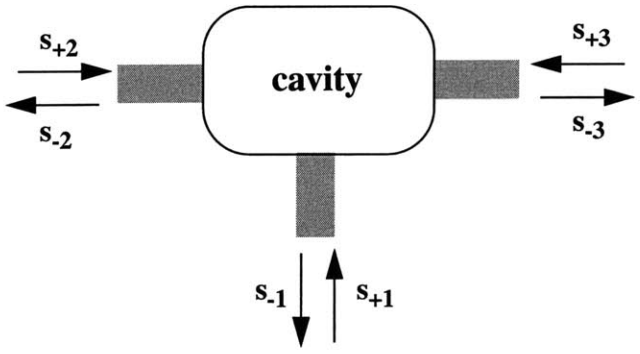

Figure 5.17: Schematic of a T-splitter as a three-port cavity.

With input $s_{+1} \sim e^{j\omega t}$, $s_{+2} = s_{+3}$ we have:

$$a = \frac{\kappa_1}{j(\omega-\omega_o)+\frac{1}{\tau_o}+\frac{1}{\tau_{e1}}+\frac{1}{\tau_{e2}}+\frac{1}{\tau_{e3}}}s_{+1} \tag{5.8}$$

The outgoing waves are given by:

$$s_{-1} = -s_{+1}+\kappa_1{}^*a \quad s_{-2} = \kappa_2{}^*a \quad s_{-3} = \kappa_3{}^*a \tag{5.9}$$

From (5.8)and (5.9) we get:

$$\frac{s_{-1}}{s_{+1}} \equiv R = \frac{-j(\omega-\omega_o)-\frac{1}{\tau_o}+\frac{1}{\tau_{e1}}-\frac{1}{\tau_{e2}}-\frac{1}{\tau_{e3}}}{j(\omega-\omega_o)+\frac{1}{\tau_o}+\frac{1}{\tau_{e1}}+\frac{1}{\tau_{e2}}+\frac{1}{\tau_{e3}}} \tag{5.10}$$

$$\frac{s_{-2}}{s_{+1}} \equiv T_L = e^{j(\theta_1-\theta_2)} \frac{\dfrac{2}{\sqrt{\tau_{e1}\tau_{e2}}}}{j(\omega-\omega_o)+\dfrac{1}{\tau_o}+\dfrac{1}{\tau_{e1}}+\dfrac{1}{\tau_{e2}}+\dfrac{1}{\tau_{e3}}} \tag{5.11}$$

$$\frac{s_{-2}}{s_{+1}} \equiv T_R = e^{j(\theta_1-\theta_3)} \frac{\dfrac{2}{\sqrt{\tau_{e1}\tau_{e3}}}}{j(\omega-\omega_o)+\dfrac{1}{\tau_o}+\dfrac{1}{\tau_{e1}}+\dfrac{1}{\tau_{e2}}+\dfrac{1}{\tau_{e3}}} \tag{5.12}$$

From (5.10) we can see that in order to transfer all the input power into ports 2 and 3 without reflection at resonance, the decay rates must satisfy:

$$\frac{1}{\tau_{e1}} = \frac{1}{\tau_{e2}} + \frac{1}{\tau_{e3}} + \frac{1}{\tau_o} \tag{5.13}$$

The ratio of the power at the two output ports is then $|T_L/T_R|^2 = \tau_{e3}/\tau_{e2}$, therefore if $1/\tau_{e2} = 1/\tau_{e3}$ the power is equally split between the two ports. In the case of negligible loss ($1/\tau_o = 0$) the condition (5.13) is in agreement with scattering matrix theory: That is, it is impossible to construct a lossless, reflectionless three-port system with three-fold symmetry ($1/\tau_{e1} = 1/\tau_{e2} = 1/\tau_{e3}$).

In Figure 5.18 we show a typical example of a HTC junction compared with a plain T. The schematic of the plain and modified junction of this example is shown in (a) and the field patterns obtained by FDTD are shown in (b) and (c). The modified junction was derived directly from the HTC bend of Figure 5.6 and its performance is similarly high. The reflection is negligible and 99% of the input power is equally distributed between the left and right outputs as shown in the transmission plot of Figure 5.18(d).

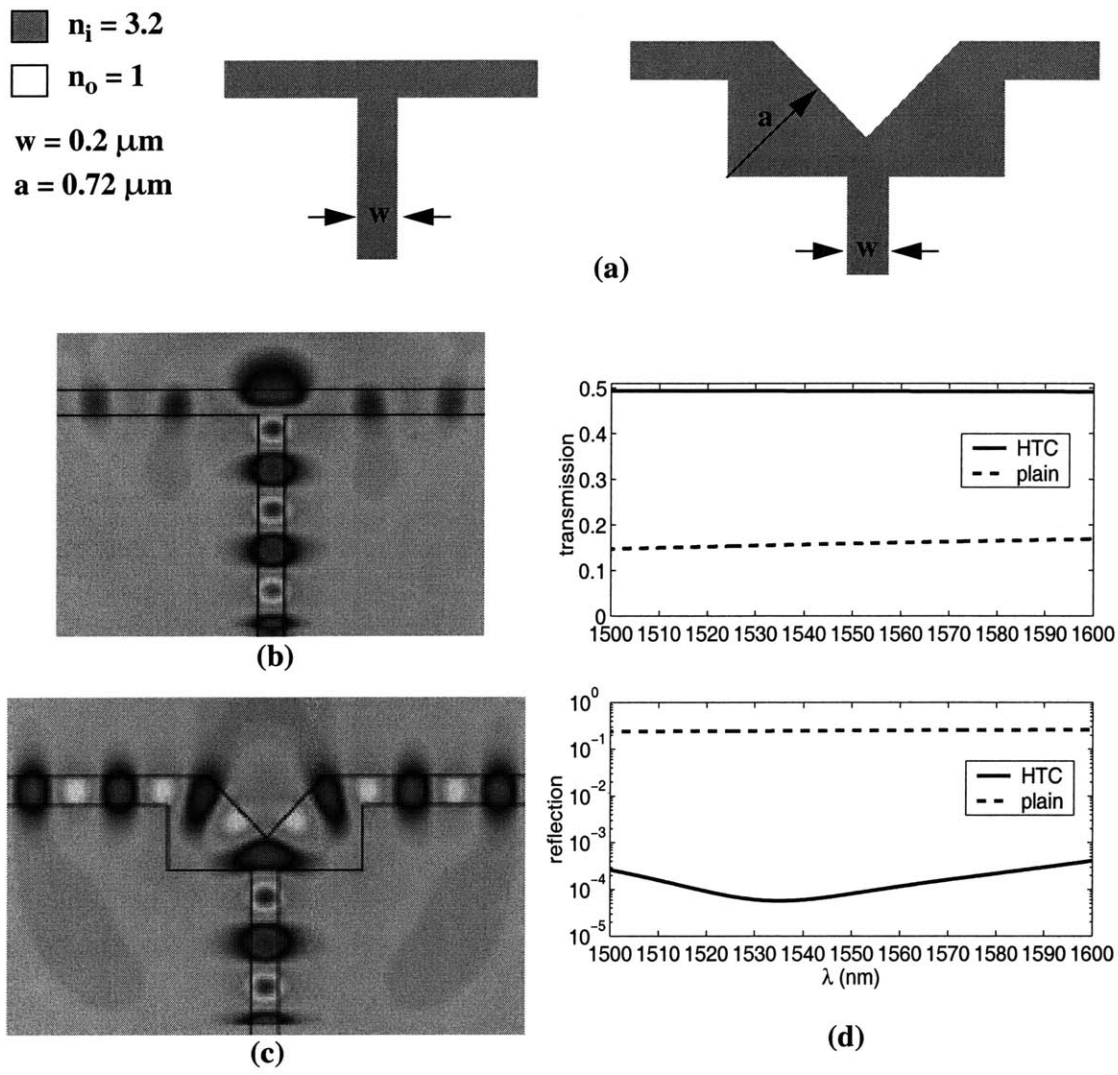

Figure 5.18: (a) Schematic of a plain and a HTC T-junction, (b),(c) respective electric field patterns and (d) transmission and reflection spectra obtained by FDTD.

Note that the performance of the HTC T-junction, in terms of reflection and radiation loss, is not significantly deteriorated by perturbing the symmetry of the structure. Thus it is possible to design junctions of different splitting ratios by moving the input waveguide (port 1) off center by a distance d as shown in Figure 5.19(a). From the field pattern in (b) we can see that a displacement d = 100nm, which is half the waveguide width, does not

cause a significant increase in the radiation compared with the symmetric case. In (c) we show the distribution of power between the two output ports when d is varied from 0 to 100nm

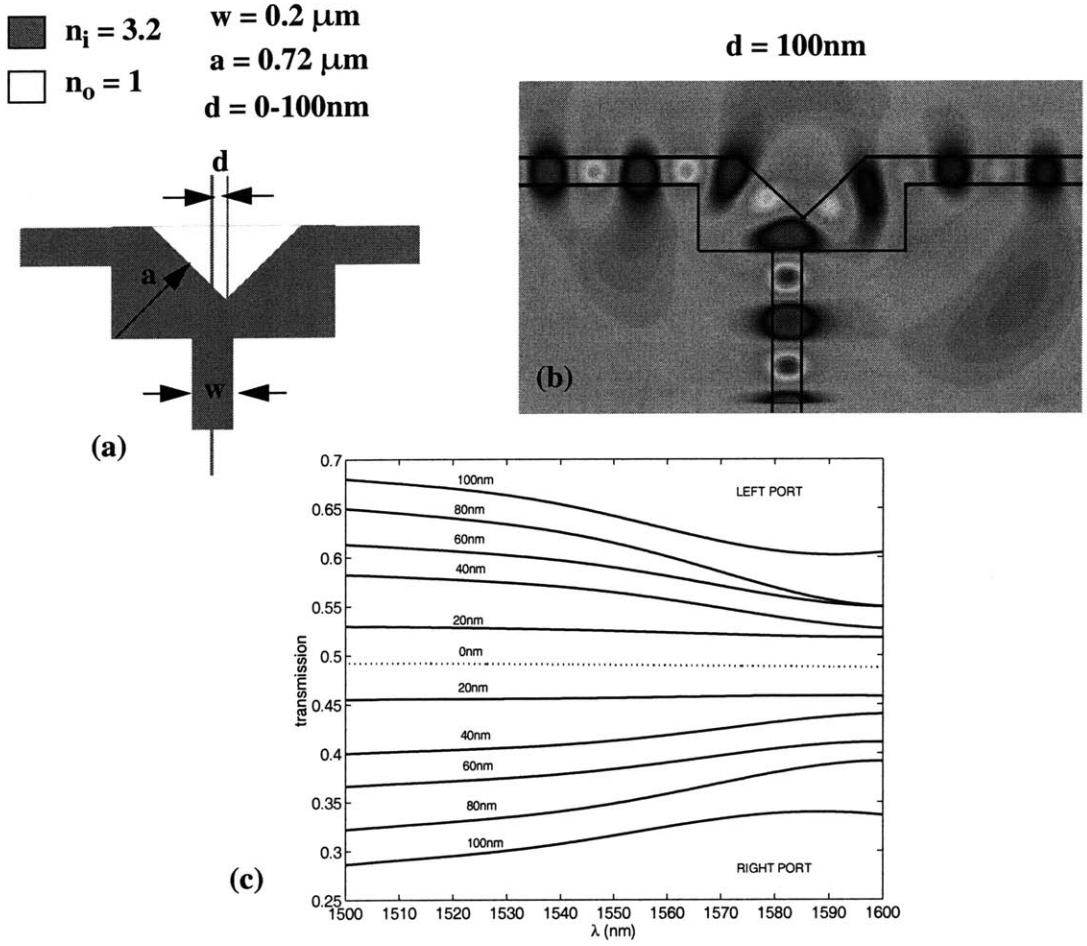

Figure 5.19: (a) Schematic of an asymmetric HTC T-junction (b) electric field pattern when the displacement is half the waveguide width and (c) distribution of the power in the two output ports for different displacements.

5.5 Waveguide crossings

In dense optical integrated circuits, waveguides may often have to intersect one another to ensure optimal placement of the various optical components on the chip and close interaction between waveguides. Ideally the wave launched in one of the intersecting waveguides must be fully transmitted forward without any power escaping sideways (crosstalk) and

with negligible reflection and radiation loss. with negligible reflection and radiation loss. Modification of the waveguide intersection for crosstalk reduction, has been employed elsewhere, e.g. [66], but for shallow-angle crossings and with a penalty in throughput. The crosstalk at right angle crossings is very small for weakly guided modes as in the case of large low index-contrast waveguides because the k-vector of the mode is almost parallel to the propagation axis. But for the high index-contrast sub micron waveguides considered here, close to 10% of the mode power escapes sideways. This is due to the strong inclination of the k-vector of the strongly guided mode with respect to the propagation axis in such waveguides.

It is possible to eliminate the unwanted crosstalk and direct all of the power forward by modifying the intersection region into a cavity with fourfold symmetry. This idea was first proposed and the operating principle explained in [54] in the context of photonic crystal waveguides. The symmetry planes of the cavity must coincide with the waveguide axes and only two degenerate modes must be supported in the frequency range of interest: One mode with odd symmetry with respect to the horizontal waveguide axis and even symmetry with respect to the vertical waveguide axis, and one mode with the opposite symmetries as illustrated in Figure 5.20. Under these conditions, each resonant mode will couple to the mode of just one waveguide and will be orthogonal to the mode of the perpendicular waveguide. Thus, with from one waveguide will leave the other waveguide unexcited leading to full transmission with zero reflection (for lossless cavity), and zero crosstalk.

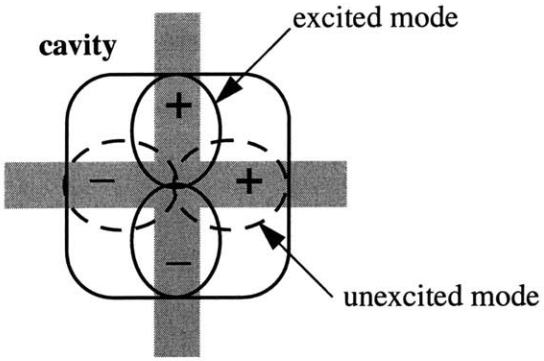

Figure 5.20: Schematic of waveguide crossing as cavity with fourfold symmetry

This idea can be explained using an alternative set of symmetric degenerate modes in a coupling-of-modes- in-time formulation into symmetric modes can be used to explain the idea with coupling of modes in time [67]. The cavity at the intersection is regarded as a four-port system (Figure 5.21) that supports two modes at the same resonant frequency ω_o with amplitudes denoted by a and b.

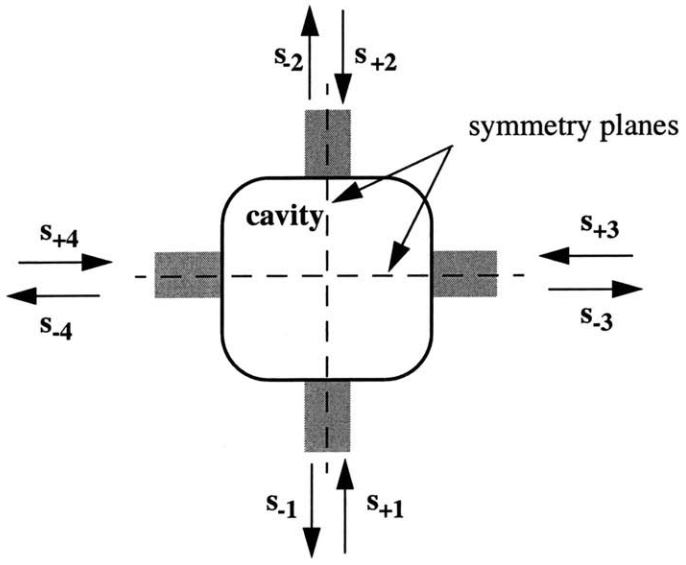

Figure 5.21: Waveguide crossing seen as a four-port system

Due to the fourfold symmetry, each mode can be made to couple equally into all four ports with associated decay rates $1/\tau_a$ and $1/\tau_b$, respectively but with different phases in the coupling coefficients:

$$\kappa_{a,i} = \sqrt{\frac{1}{\tau_a}} e^{j\theta_{ai}} \quad \kappa_{b,i} = \sqrt{\frac{1}{\tau_b}} e^{j\theta_{b,i}} \qquad i = 1, \ldots, 4 \tag{5.14}$$

For simplicity the cavity is assumed lossless. The inputs(outputs) at each port are again denoted by $s_{+i}(s_{-i})$, $i = 1, \ldots, 4$. With input $s_{+1} \sim e^{j\omega t}$, at steady state we have:

$$a = \frac{\kappa_{a,1}}{j(\omega - \omega_o) + \frac{4}{\tau_a}} s_{+1} \qquad b = \frac{\kappa_{a,2}}{j(\omega - \omega_o) + \frac{4}{\tau_b}} s_{+1} \tag{5.15}$$

and the outputs are given by (see section 2.5.2)

$$\begin{aligned} s_{-1} &= -s_{+1} + \kappa_{a,1}{}^* a + \kappa_{b,1}{}^* b \qquad & s_{-3} &= \kappa_{a,3}{}^* a + \kappa_{b,3}{}^* b \\ s_{-2} &= \kappa_{a,2}{}^* a + \kappa_{b,2}{}^* b & s_{-4} &= \kappa_{a,4}{}^* a + \kappa_{b,4}{}^* b \end{aligned} \tag{5.16}$$

From (5.14)-(5.16) we have:

$$\frac{s_{-1}}{s_{+1}} \equiv R = -1 + \frac{\frac{2}{\tau_a}}{j(\omega - \omega_o) + \frac{4}{\tau_a}} + \frac{\frac{2}{\tau_b}}{j(\omega - \omega_o) + \frac{4}{\tau_b}} \tag{5.17}$$

$$\frac{s_{-2}}{s_{+1}} \equiv T = e^{j(\theta_{a,1} - \theta_{a,2})} \frac{\frac{2}{\tau_a}}{j(\omega - \omega_o) + \frac{4}{\tau_a}} + e^{j(\theta_{b,1} - \theta_{b,2})} \frac{\frac{2}{\tau_b}}{j(\omega - \omega_o) + \frac{4}{\tau_b}} \tag{5.18}$$

$$\frac{s_{-3}}{s_{+1}} \equiv X_L = e^{j(\theta_{a,1} - \theta_{a,3})} \frac{\frac{2}{\tau_a}}{j(\omega - \omega_o) + \frac{4}{\tau_a}} + e^{j(\theta_{b,1} - \theta_{b,3})} \frac{\frac{2}{\tau_b}}{j(\omega - \omega_o) + \frac{4}{\tau_b}} \tag{5.19}$$

$$\frac{s_{-4}}{s_{+1}} \equiv X_R = e^{j(\theta_{a,1}-\theta_{a,4})}\frac{\frac{2}{\tau_a}}{j(\omega-\omega_o)+\frac{4}{\tau_a}} + e^{j(\theta_{b,1}-\theta_{b,4})}\frac{\frac{2}{\tau_b}}{j(\omega-\omega_o)+\frac{4}{\tau_b}} \tag{5.20}$$

The desired behavior is achieved if the two modes couple in phase into ports 1 and 2, that is $\theta_{a,1}-\theta_{b,1}=0$, $\theta_{a,2}-\theta_{b,2}=0$, and out of phase into ports 3 and 4, that is $\theta_{a,3}-\theta_{b,3}=\pi$, $\theta_{a,4}-\theta_{b,4}=\pi$. Then (5.17)-(5.20) become:

$$R = -1 + \frac{\frac{2}{\tau_a}}{j(\omega-\omega_o)+\frac{4}{\tau_a}} + \frac{\frac{2}{\tau_b}}{j(\omega-\omega_o)+\frac{4}{\tau_b}} \tag{5.21}$$

$$T = e^{j(\theta_{a,1}-\theta_{a,2})}\left(\frac{\frac{2}{\tau_a}}{j(\omega-\omega_o)+\frac{4}{\tau_a}} + \frac{\frac{2}{\tau_b}}{j(\omega-\omega_o)+\frac{4}{\tau_b}}\right) \tag{5.22}$$

$$X_L = e^{j(\theta_{a,1}-\theta_{a,3})}\left(\frac{\frac{2}{\tau_a}}{j(\omega-\omega_o)+\frac{4}{\tau_a}} - \frac{\frac{2}{\tau_b}}{j(\omega-\omega_o)+\frac{4}{\tau_b}}\right) \tag{5.23}$$

$$X_R = e^{j(\theta_{a,1}-\theta_{a,4})}\left(\frac{\frac{2}{\tau_a}}{j(\omega-\omega_o)+\frac{4}{\tau_a}} - \frac{\frac{2}{\tau_b}}{j(\omega-\omega_o)+\frac{4}{\tau_b}}\right) \tag{5.24}$$

At $\omega = \omega_o$ the reflection and the crosstalk are zero and the incoming signal is fully transmitted forward. If, in addition $\tau_a = \tau_b = \tau_e$, the outputs at ports 3 and 4 remain zero at all frequencies. Note that the set of degenerate modes in this analysis is made up of the sum and the difference respectively of the modes in the analysis of [54].

Next, we illustrate this concept with FDTD simulations, starting with the behavior of a plain waveguide intersection in a high index-contrast single-mode waveguide shown in

Figure 5.22 As previously mentioned close to 10% of the power leaks sideways in either direction as unwanted crosstalk and only ~80% of the input power is transmitted forward.

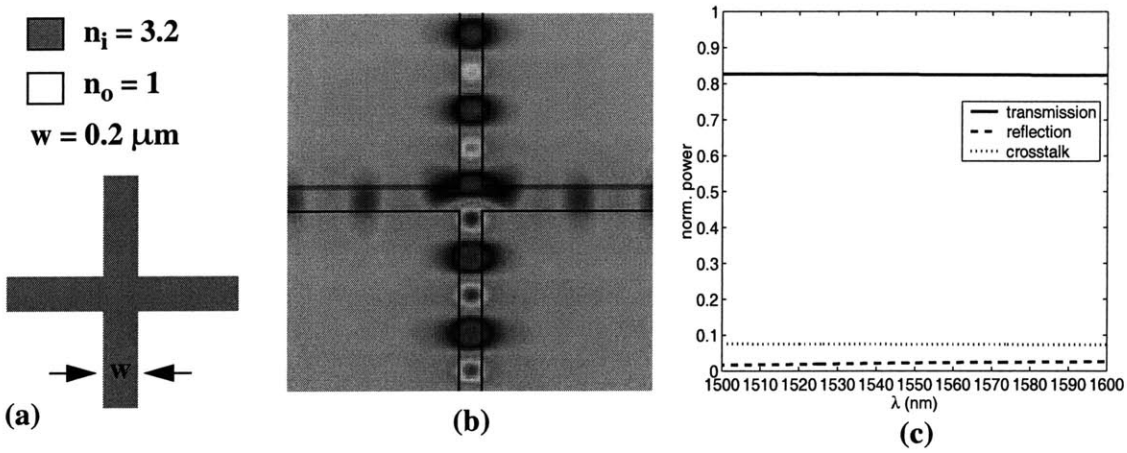

Figure 5.22: Waveguide intersection (a) schematic (b) electric field (c) transmission, reflection and crosstalk spectra

The crosstalk can be drastically reduced by making appropriately spaced slots on the arms of the cross as shown in the schematic of Figure 5.23(a) Adding dielectric at the center as shown in Figure 5.23(b) offers an additional degree of freedom and better light confinement. As an initial guess, the spacing l of the slots away from the center is approximately half a guided wavelength in the arms of the crossing. At the center, their distance d is approximately a quarter guided wavelength longer. This structure can also be viewed as a crossing between two quarter-wave-shifted periodic resonators or two 1D photonic crystal microcavities [54].

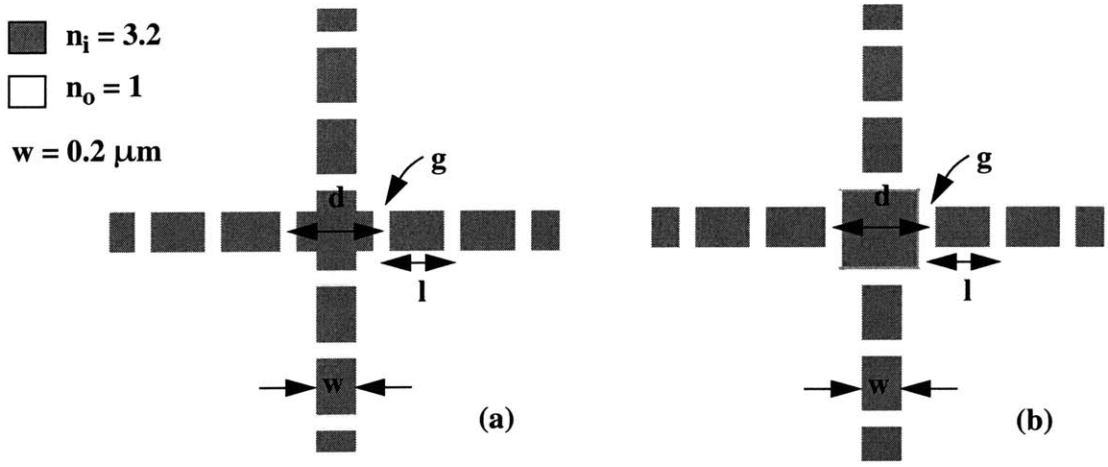

Figure 5.23: Possible implementations of a cavity at the intersection.

The optimal design parameters deviate from the initial guess since the presence of the slots reduces the average dielectric in the crossing waveguides thus increasing guided wavelength and the distance l. The addition of dielectric in the center, in Figure 5.23(b) increases the effective index thus reducing the wavelength in the cavity and the distance d. The best numerical results for this type of waveguide-crossing and the design parameters are shown in Figure 5.24 for (a) one, (b) two and (c) three slots on each arm. The simulations show that in case (a) the resonance frequency is more strongly affected by the size of the square at the center. The width of the slots determines the coupling between cavity and waveguides and in a smaller degree the resonance wavelength: Wider slots result in weaker coupling and therefore narrower resonance while the resonance shifts to shorter wavelengths due to the lowering of the average dielectric. Beyond a certain slot width of about 100nm, however, the performance starts to deteriorate due to increased scattering loss. Increasing the number of slots has similar effects, with a less significant increase in radiation loss. An additional set of slots as in case (b) yields a narrower resonance, and further reduction of the crosstalk. The peak transmission is also increased because the

radiation loss is greatly reduced in the cavity. Further increase of the number of cuts, as in (c), lowers the average dielectric and shifts the resonance to shorter wavelengths. Moreover, assuming same radiation loss as in (b), the weaker coupling leads to a slight decrease of the peak transmission. The best combination of peak transmission, crosstalk and bandwidth characteristics for this particular configuration is obtained with two slots. The peak transmission for this case is 96% and the crosstalk less than 10^{-3}. Similar results can be obtained for the type of Figure 5.23(a) but with slightly increased reflection and radiation loss.

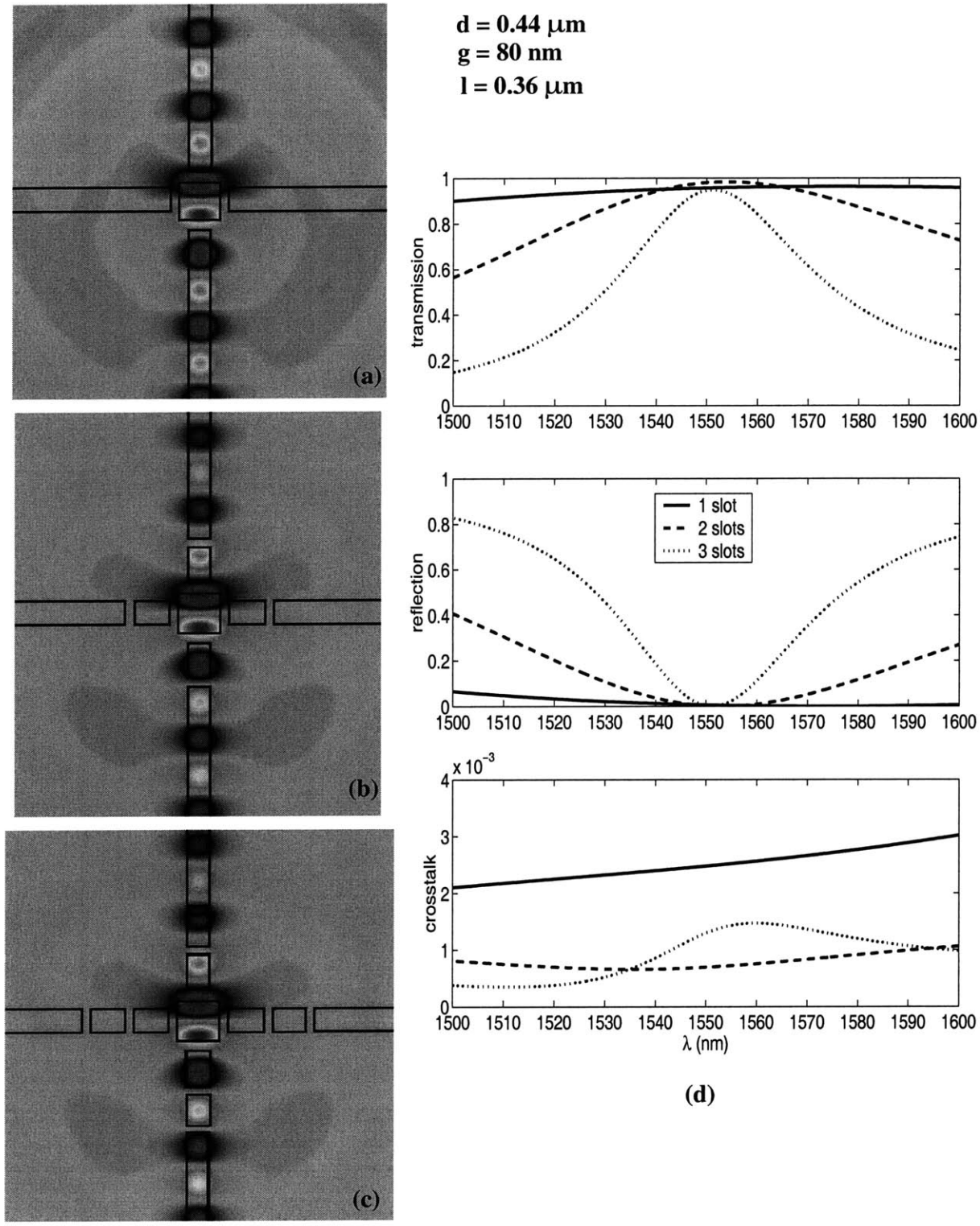

Figure 5.24: Electric field patterns in waveguide crossings with (a) 1 slot, (b) 2 slots, (c) 3 slots and (d) comparison of the respective spectra

Chapter 6

Fiber-PIC coupling

6.1 Introduction

One of the characteristics of the passive devices presented so far is the fact that they are based on single-mode high index-contrast waveguiding which enables the dense integration of many such devices on an optical chip. A major disadvantage of this approach, compared with more conventional low index-contrast (such as silica based) integrated optics, is the difficulty of coupling light to and from an optical fiber. Approximating the fiber mode by a gaussian distribution (see section 2.6.3) the mode field diameter (MFD) of a fiber is defined as the $1/e^2$-diameter of the gaussian power distribution and is approximately 15% larger than the core diameter. For a single-mode fiber (SMF) with flat-end the typical MFD is 8-10 μm and the mode cross-section is ideally circular. A lensed fiber has typical output beam diameter ~50% of the typical MFD and ~20 μm focal length [68]. A high index-contrast waveguide has a fundamental mode in the submicron range and, depending on the aspect ratio of the rectangular waveguide core, the mode cross-section is strongly elliptical. This large mode-mismatch leads to very inefficient fiber-waveguide coupling where most of the power is lost to radiation. The coupling loss between fibers of different MFD, assuming that they are perfectly aligned, is [68]:

$$\text{loss (dB)} = -10\log\left\{\frac{4}{\left(\frac{MFD_1}{MFD_2}+\frac{MFD_2}{MFD_1}\right)^2}\right\} \tag{6.1}$$

If we ignore the ellipticity of a waveguide mode and apply (6.1) to get an estimate for the coupling between a fiber and waveguide with a 5-to-1 MFD ratio we find a 8.3 dB loss,

that is less than 15% coupling efficiency. We illustrate this with a 2D numerical example where a low-index wide waveguide (n = 1.05, w = 4 μm and MFD~4.8 μm) is butt-coupled to a high-index narrow waveguide (n = 3, w = 0.25 μm) and the whole system is surrounded by air (n=1). As Figure 6.1 shows most of the power is lost to radiation and only 17% of the power is coupled into the waveguide mode.

Most approaches to solving this problem, encountered in the literature, can be broadly classified into to two types depending on whether the coupling scheme is on the fiber side or on the chip side. In the first type of coupling the fiber tip is modified by tapering and/or lensing to bring the MFD of the fiber mode closer to that of the integrated waveguide [69],[70]. In the second type the core of the integrated waveguide is adiabatically tapered so that the mode fields spreads out into the cladding to match the fiber mode size [71],[72]. Both types of coupling result in structures up to a few hundreds of μm long.

Mode conversion schemes that work entirely on the fiber side may lead to critical alignment tolerances as the fiber mode size gets very small. Moreover there is still a mismatch due to the different mode-shapes, that of the fiber being circular and that of the waveguide being in general highly elliptical. For these reasons it is preferable to concentrate most or all the mode matching efforts on the chip-side. Better alignment tolerances are thus obtained and we have the added advantage that one kind of fiber can be used to couple light into different PICs.

In this chapter we present two basic ideas that allow efficient coupling within only a few μm. For simplicity we assume that the fiber mode has a MFD of ~5 μm coming from a lensed SMF. Alternatively we can consider that the input mode field is coming from a large low-index waveguide which may be viewed as an intermediate stage between the fiber and the high index-contrast waveguide.

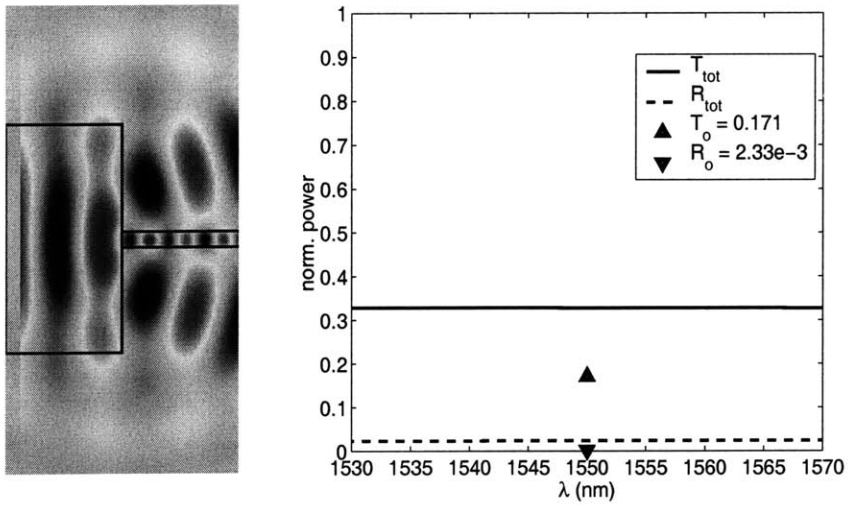

Figure 6.1: Example of coupling from a low index-contrast wide waveguide to a high index-contrast single mode waveguide (a) electric field (b) transmission and reflection response.

6.2 Mode conversion with cascade of square resonators

The first approach is based on resonators. A cascade of high index-contrast square resonators with gradually smaller dimensions are placed between the input fiber or large waveguide and the target high index-contrast waveguide as shown in the schematic of Figure 6.2. The effect of the resonators is to concentrate the mode power in an area of gradually fewer wavelengths in size until the extend of the mode field in the resonator is close to that of the narrow waveguide. The gaps between the squares affect the reflection and the coupling between the squares and they have to be kept narrow enough to avoid excessive scattering. In the examples presented below we have calculated not only the total transmitted and reflected power but also the fraction of power that is coupled specifically into the fundamental mode of the waveguide and of the fiber at $\lambda = 1550\,\text{nm}$. This value is obtained using numerical mode overlaps as explained in Section 3.5 based on the theory of

Section 2.3. This additional calculation is necessary in order to separate out the contribution of the radiation modes which inevitably enters the total power in such in-line arrangements.

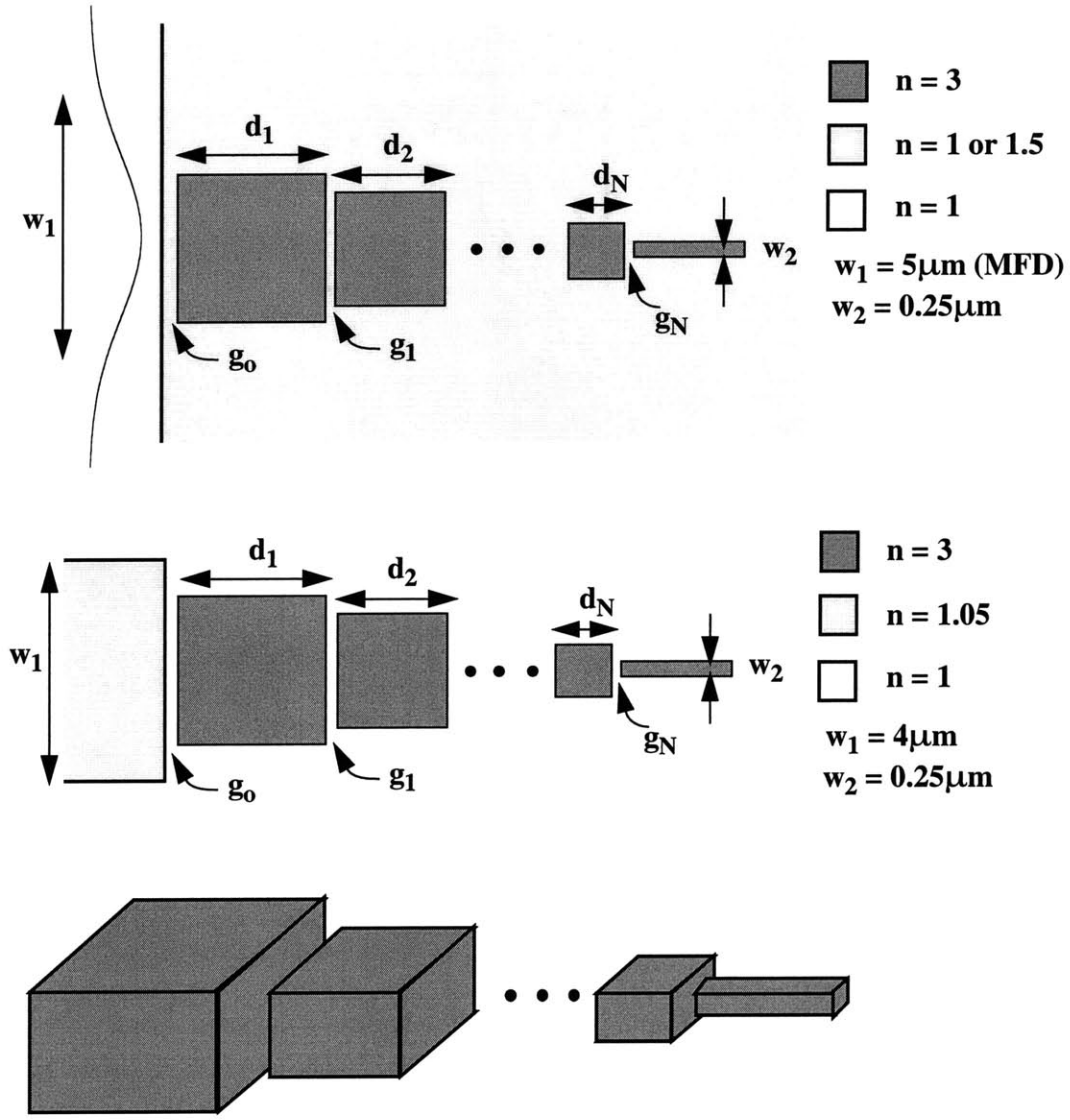

Figure 6.2: Two possible arrangements for a cascade of resonators as a mode-matching structure and a possible 3D implementation.

In Figure 6.3 a cascade of four squares of high-index is used to improve the coupling efficiency. The large mode has a gaussian profile closely approximating that of a lensed fiber and is assumed to impinge on the coupling structure from free space. The narrow waveguide is only 0.25 μm to ensure single-mode operation. The total power and transmission and reflection as well as the fraction coupled into the fundamental modes at $\lambda = 1550$ nm are shown for both directions of coupling, the forward direction taken from the fiber to the chip and the backward direction taken from the chip to the fiber. As we can see in the spectral responses there is a strong wavelength dependence which is expected since we rely on high-order resonances. There is a markedly improved coupling efficiency in comparison with the example of Figure 6.1, with maximum power transfer of about 75%. We note that the total power transfer from one side to the other is clearly lower in the forward direction than in the backward direction, and almost the same as the power transfer between the fundamental modes. However the coupling between the fundamental modes is the same in both directions and this can be explained by scattering matrix theory: We can view the total system as a multi-port system with ports 1 and 2 assigned to the fundamental modes of the fiber and the integrated waveguide, respectively and the rest of the ports assigned to the higher order guided and/or radiation modes. Since the system is reciprocal we have $S_{12} = S_{21}$ but since it is not symmetric we expect $S_{11} \neq S_{22}$. In this example in the forward direction we have $T_o = S_{21}$, $R_o = S_{11}$ and in the backward direction $T_o = S_{12}$, $R_o = S_{22}$.

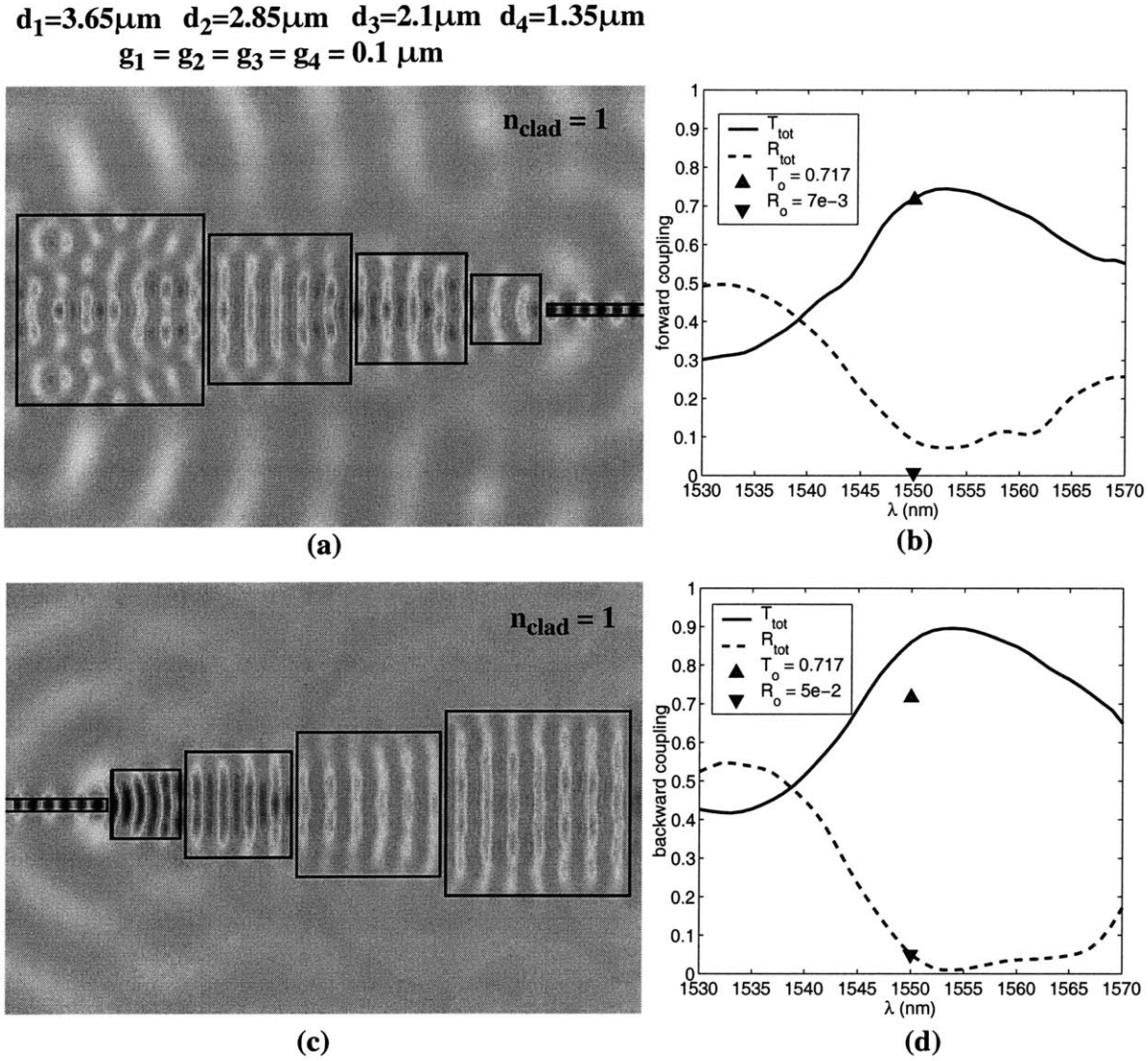

Figure 6.3: Fiber-chip coupling using a cascade of squares surrounded by air, illustrated in both propagation directions (a),(c) Electric field amplitudes (b),(d) corresponding spectra.

Another example is shown in Figure 6.4 where this time the entire system of high-index square resonators and waveguide is considered buried in a material with index n=1.5 e.g. SiO_2 cladding. The resonator dimensions are the same as before except the first one which is 125nm larger in each side. Also, in order to reduce the reflection the cascade is

moved by 0.25 μm inside the n=1.5 area; this length is approximately $\lambda/4$ for this index. We have repeated the same calculations which show that the total power transfer is higher out of the chip than into the chip while the coupling between the fundamental modes is the same in both directions and only slightly lower than in the previous example. If the cascade starts at the edge of the "chip" both T_{tot} and T_o are 1-2% lower.

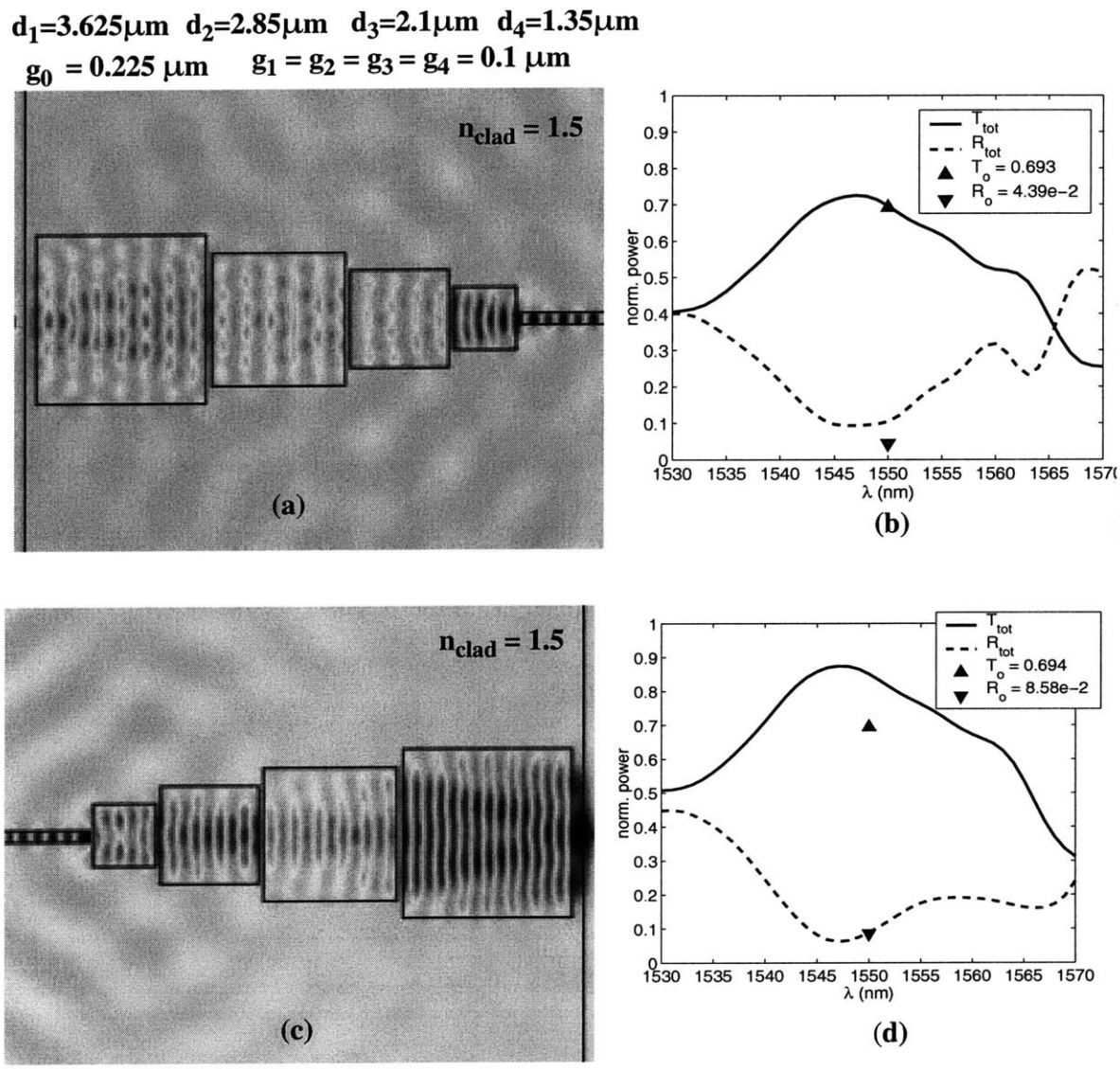

Figure 6.4: Fiber-chip coupling using a cascade of squares surrounded by n = 1.5, illustrated in both propagation directions (a),(c) Electric field amplitudes (b),(d) corresponding spectra.

Finally, a cascade of squares is coupled to a large low-index waveguide which can be considered as an intermediate stage on the chip between the fiber and the coupling structure. The coupling between the fiber and fundamental mode of this waveguide is about 99%. In Figure 6.5(a) and (b) the field pattern and the associated spectra are for the forward direction. In (c) we show how drastically the spectrum changes for the different arrangements of the gaps shown in the adjacent schematics, especially in the last case of (c) where the spectra are almost inverted with the reflection up to almost 80% and the transmission no more than 10%.

The use of a low-index wide waveguide on the chip, with its fundamental mode well matched to the fiber mode, may offer an additional degree of freedom for impedance matching, e.g. by making slots at proper spacings as was done in the waveguide crossing of Chapter 5.

In spite of its simplicity the fiber-chip coupling scheme presented in this section has certain clear disadvantages. None of the cases examined has resulted in more than 70-80% coupling. There are no simple design rules and, due to the strong wavelength dependence, the performance is very sensitive to the size and location of both the gaps and the resonators.

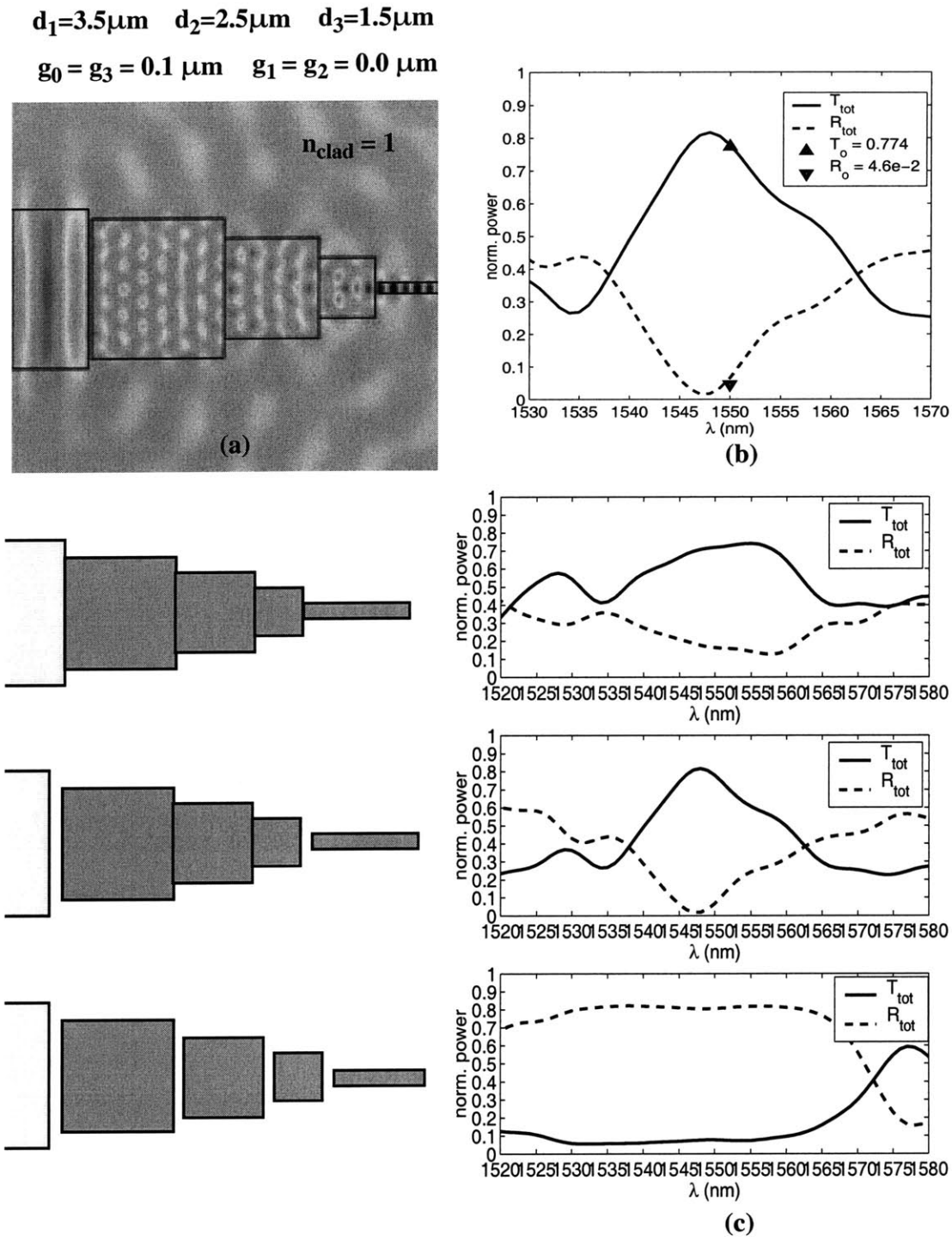

Figure 6.5: Coupling between a low-index wide waveguide and a high-index narrow waveguide using a cascade of squares. (a) Electric field and (b) associated spectrum, (c) dependence of the response on gap location.

6.3 Mode conversion using dielectric planar lenses

Now we present an entirely different approach to the fiber-chip coupling problem, not based on resonance. Since the mode of a fiber can be approximated by a gaussian beam we can consider using gaussian optics to design lens-like structures that can bring the MFD of the fiber down to that of the of the integrated waveguide mode. The analytical part of the design can then be based on the well known transformation laws of gaussian beams using ABCD matrices that were presented in section 2.6.2. A very good first guess for the design parameters can be obtained with this method for known mode widths. Since Gaussian optics are based on the paraxial approximation which in general does not hold in high index-contrast, strongly guided structures, this method is only approximate and FDTD simulations are still necessary for accurate modelling.

As we shall see in the examples of this section efficient coupling is achieved through lensing within a distance of only ~6μm. The schematic of Figure 6.6(a) shows the simplest implementation of this idea. The lens-like structure is of the same index as the high index-contrast waveguide and the system is surrounded by air. A layer of index $n_2 = \sqrt{n_1 n_2} = 1.73$ and thickness $d = \lambda/4n_2 = 0.22\ \mu m$ on the propagation axis is there for impedance matching at the location maximum intensity. The expected beam evolution in Figure 6.6(b) shows that the beam diameter can be reduced to well under 1 μm in less than 5 μm.

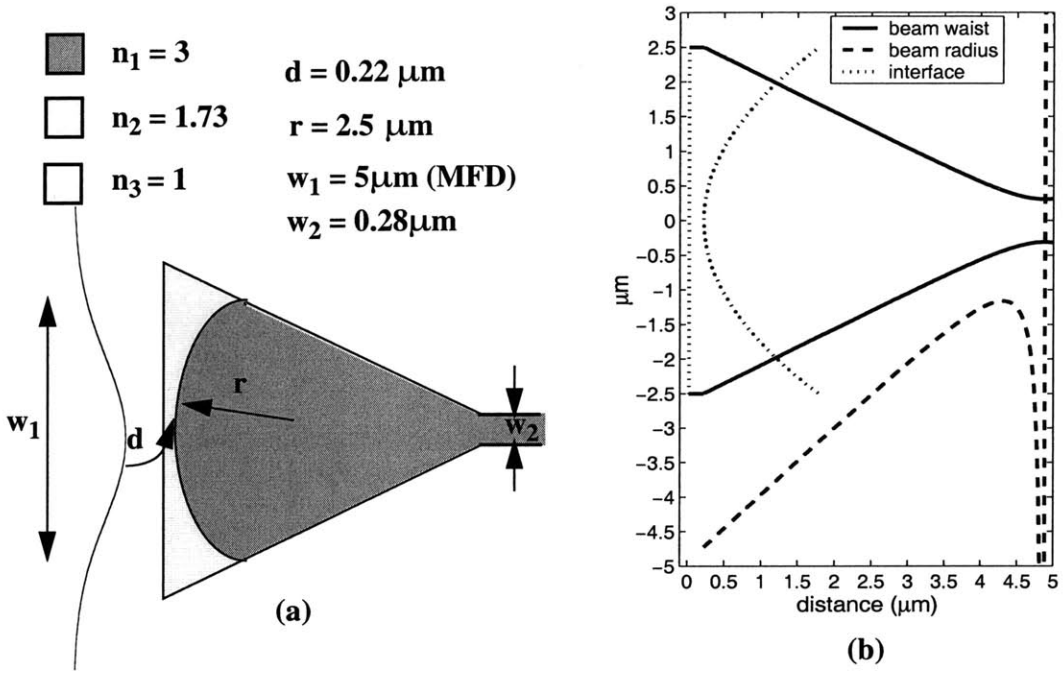

Figure 6.6: (a) Schematic of a planar lens and (b) the expected beam waist and phase-front radius evolution along the device obtained by the ABCD matrix formalism.

The FDTD calculation of the associated spectrum shows that 82% of the input power is transferred from the fiber to the waveguide mode. The simulation is performed in both propagation directions. As argued in the previous section, the coupling between the two modes is equal in both directions whereas the total power is higher in the backward direction. This structure is far from optimal. The radius of curvature is very small and the impedance matching layer greatly deviates from the right thickness away from the center. Moreover as the almost plane wave fronts of the input beam impinge on a strongly curved interface additional reflection is caused due to phase mismatch.

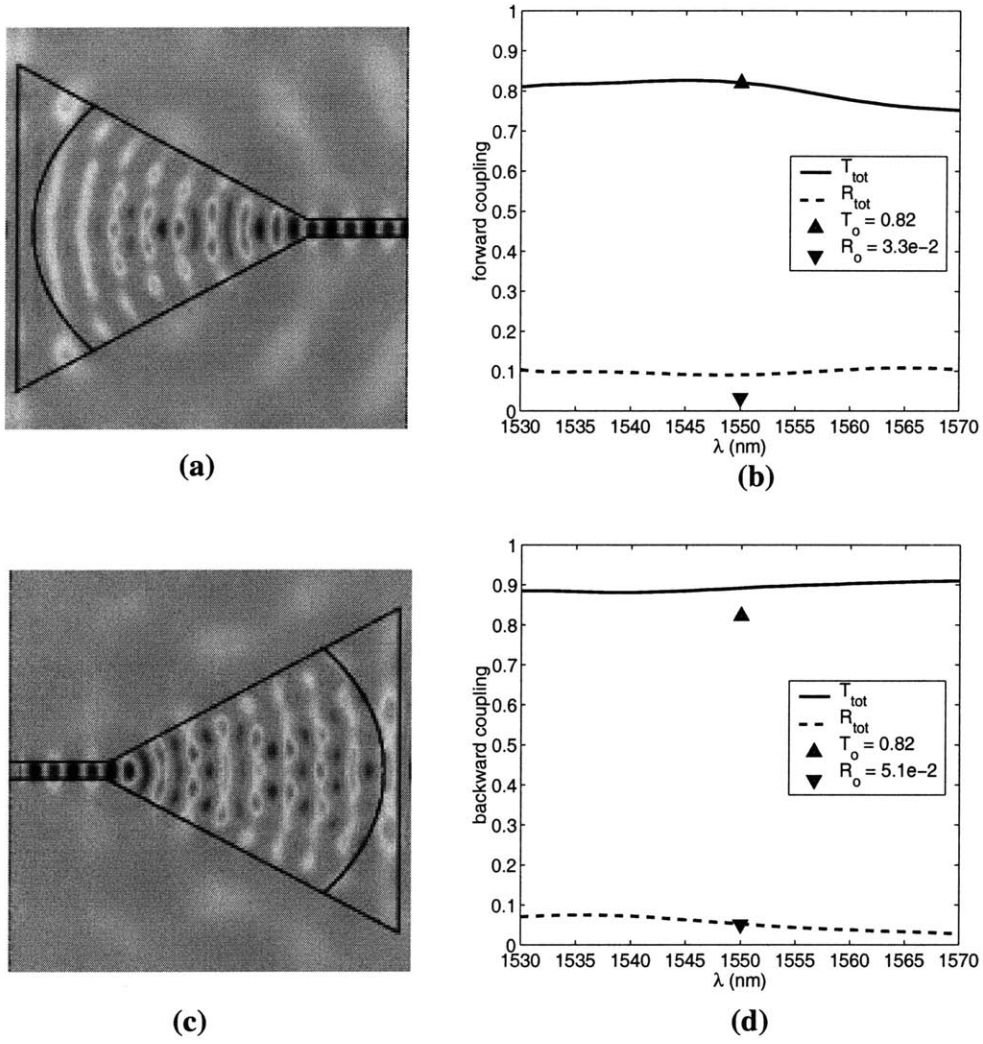

Figure 6.7: (a),(c) Electric field amplitudes for forward and backward propagation in a simple lens like coupler and (b),(d) associated spectra.

An improved version is shown in Figure 6.8 where both interfaces air/matching layer and matching layer/ "lens" are curved the first with a slightly larger radius of curvature. The effect of that is the smoother transition form flat to curved wavefronts and vice versa and the thickness of the impedance matching layer stays approximately the same away from the axis.

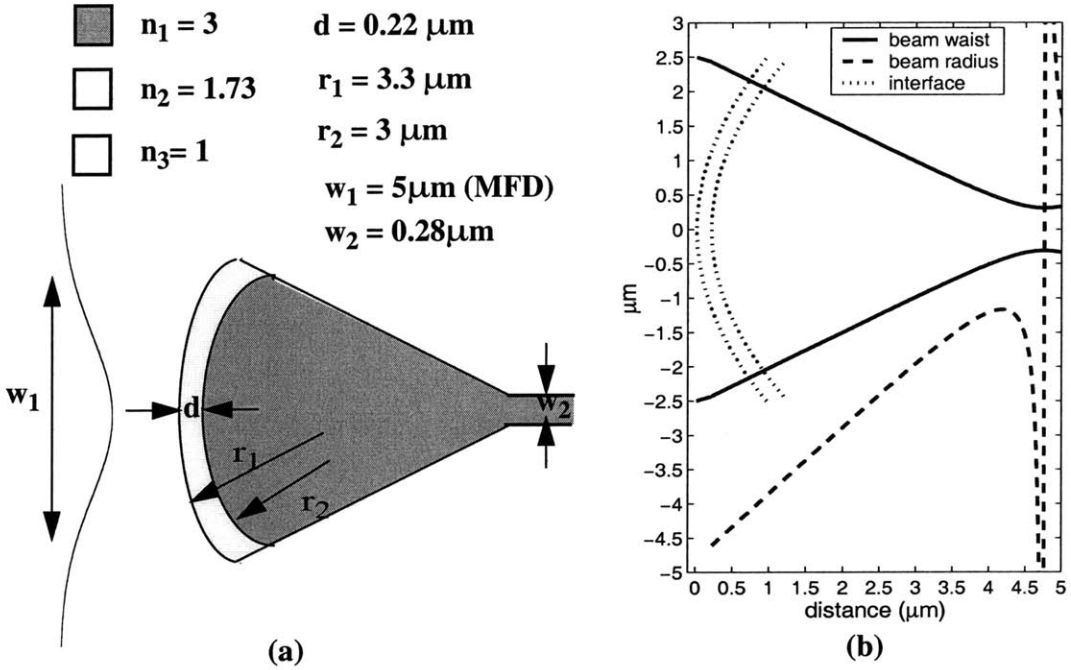

Figure 6.8: (a) Schematic of a planar lens and (b) Expected beam waist and phase-front radius evolution along the device obtained by the ABCD matrix formalism.

The theoretically expected behavior of the beam is very similar with the previous case. The FDTD simulation results in Figure 6.9 show an improved performance in both directions and again verify the reciprocity of the coupling between individual modes.

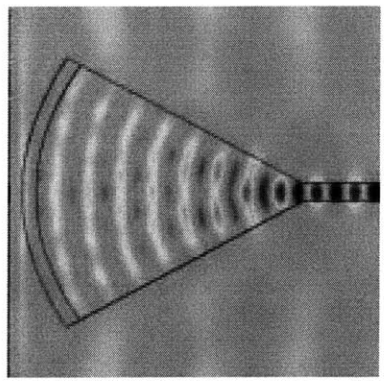

(a)

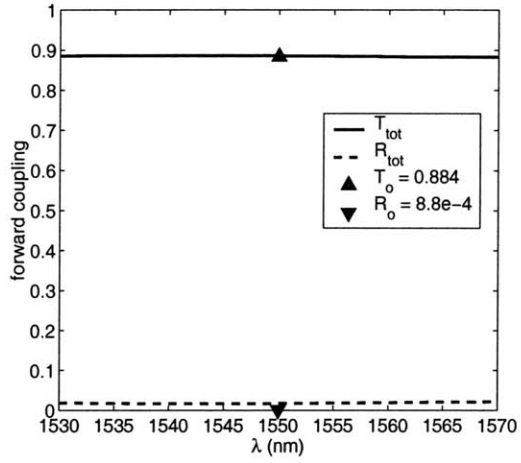

(b)

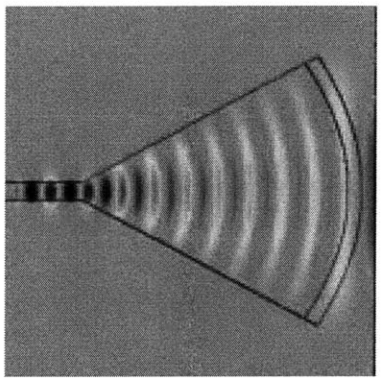

(c)

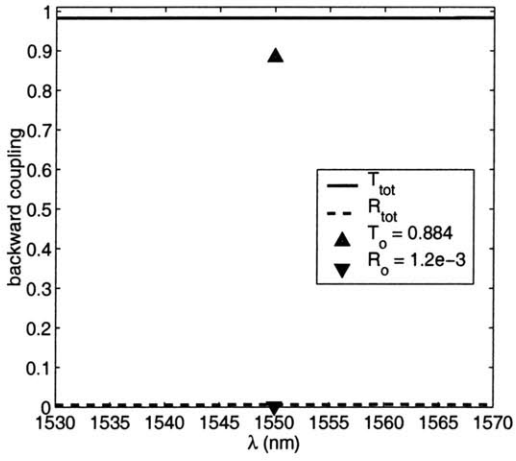

(d)

Figure 6.9: (a),(c) Electric field amplitudes for forward and backward propagation in a simple lens like coupler with curved impedance-matching layer and (b),(d) associated spectra.

This design can be improved by making a gentler curve at the outer interface. The theoretical and numerical results for this case are shown in Figure 6.10

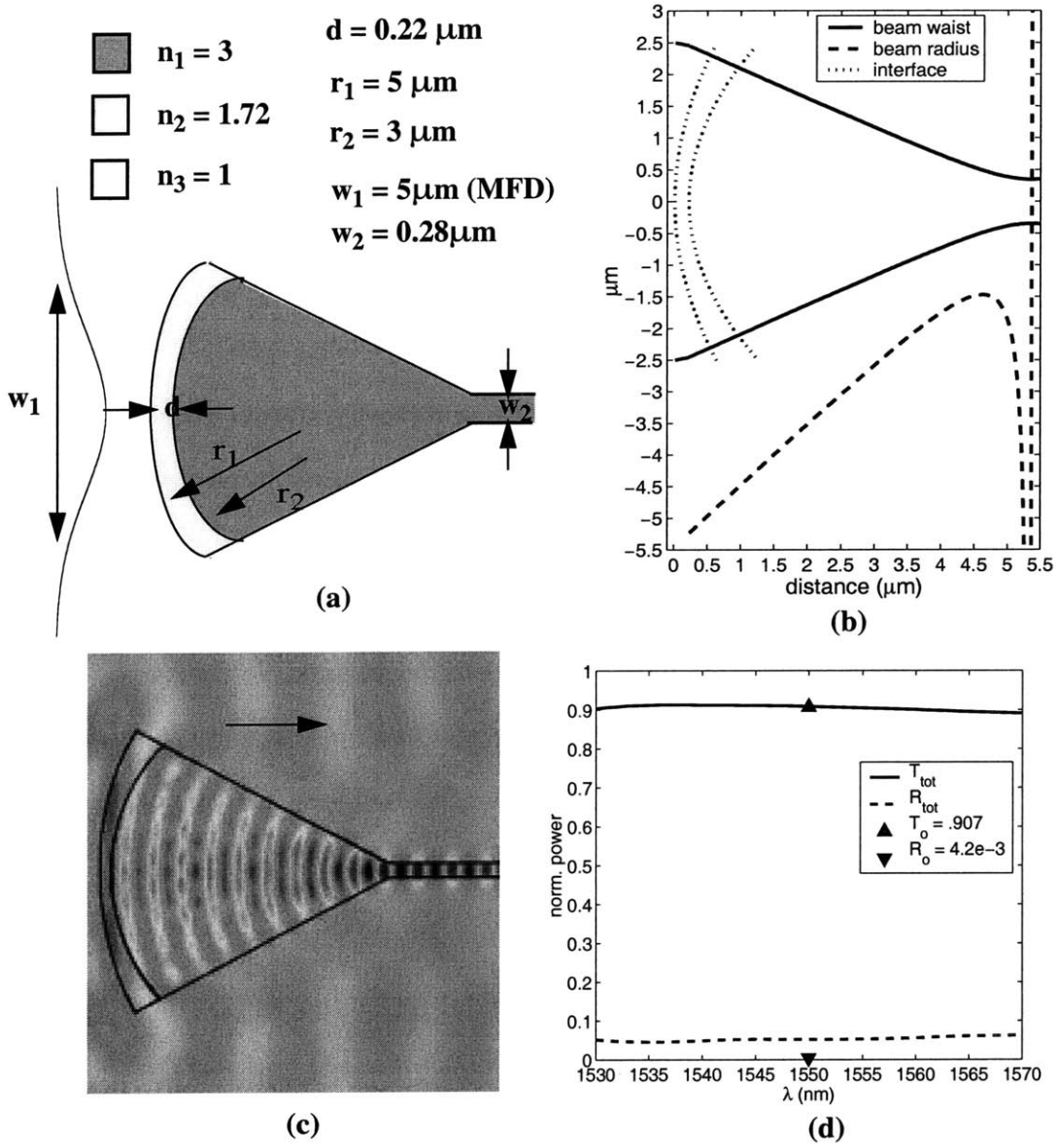

Figure 6.10: (a) Schematic of a planar lens with impedance matching layer (b) Expected beam waist and phase-front radius evolution along the device obtained by ABCD matrix analysis (c) Electric field amplitude for forward propagation in a simple lens like coupler (d) associated spectra.

Finally we consider the case of a coupler-waveguide system surrounded by n = 1.5 (e.g. SiO_2 cladding). We apply the same ideas as before regarding the choice of curvature,

index and thickness of the different layers. One of the best responses was obtained when we used more than one matching layers as shown in the schematic of Figure 6.11(a) with refractive indices chosen to approximately satisfy $n_2 = \sqrt{n_1 n_3}, n_3 = \sqrt{n_2 n_4}$ and $n_4 = \sqrt{n_3 n_5}$ and respective thicknesses approximately $\lambda/4n$. Almost 92% transmission was obtained with very low reflection into the fiber mode.

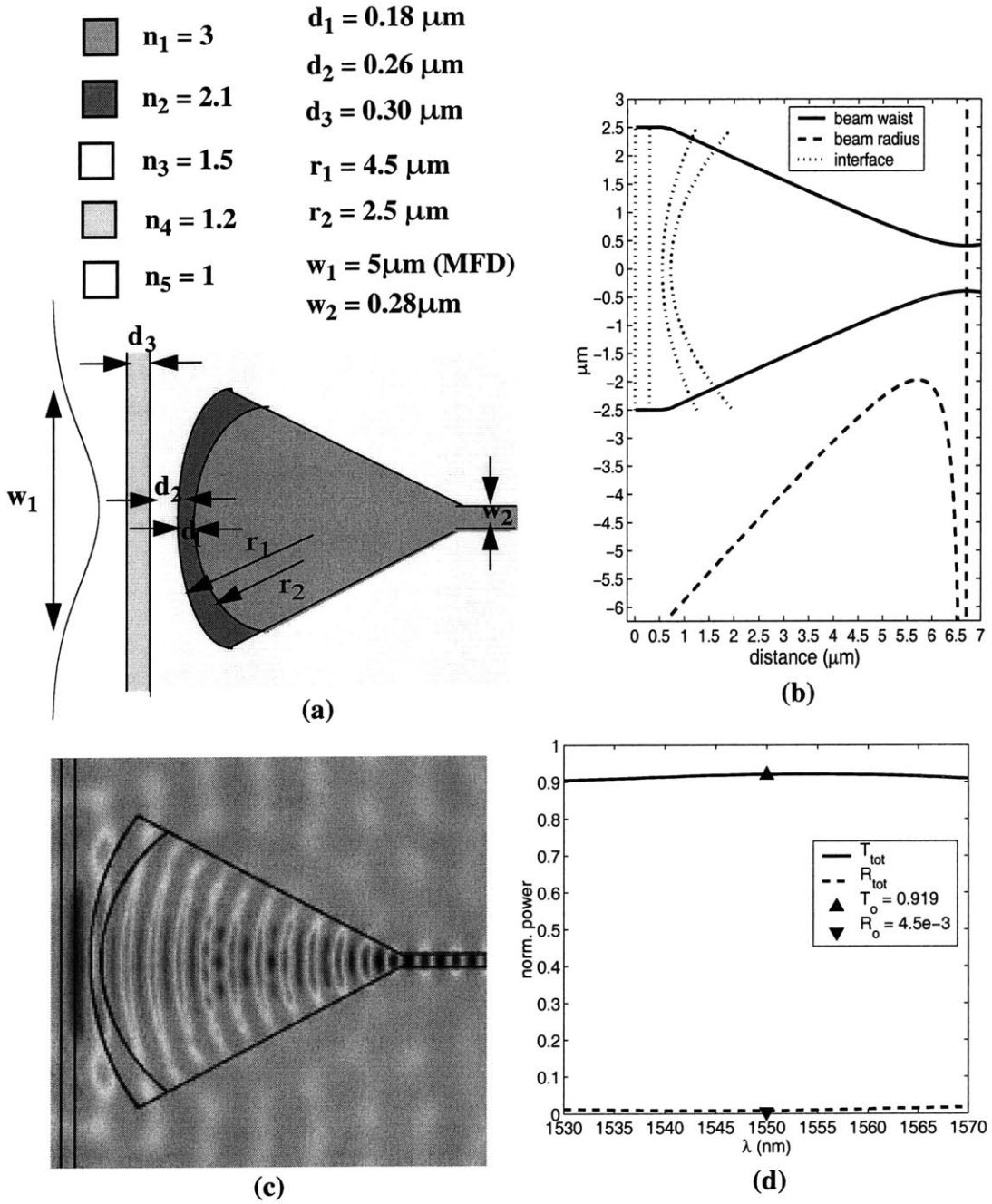

Figure 6.11: (a) Schematic of a planar lens with impedance matching layers (b) Expected beam waist and phase-front radius evolution along the device obtained by the ABCD matrix method (c) Electric field amplitude for forward propagation in a simple lens like coupler (d) associated spectra.

6.4 3D mode-conversion scheme

All the numerical examples presented so far were in two dimensions and addressed the problem of lateral mode-size conversion while ignoring variations in the vertical dimension. The extension to three dimensions may be simpler for the cascade of square resonators, i.e. if we replace the planar square cavities by cubic cavities, as was shown in the schematic of Figure 6.2(c). The treatment of the vertical direction is not obvious in the case of lensing. In theory the same scheme can work in 3D using a spherical or ellipsoidal lens and the theoretical analysis can be performed separately for the two q-parameters of an elliptical gaussian as discussed in sections 2.6.1-2. However, the fabrication of a structure with one or more interfaces with 3D curvature would be a very difficult task. A different approach for vertical focussing must be used, which is suited for fabrication in the vertical direction. According to our discussion of gaussian beam propagation in quadratic index media in section 2.6.1, an obvious choice for vertical lensing would be a layered structure with the index varying quadratically from layer to layer. The schematic of Figure 6.12 shows two possible ways of incorporating the graded index lensing structure in a 3D coupler. In (a) we have two separate stages, a layered one for the vertical focussing followed by a planar "lens" for the lateral focussing. In (b) the two stages are merged into one coupler which combines layering along x and planar lensing along y. The arrangement in Figure 6.12:(b) is preferable since the separation into two stages may introduce additional reflections and beam spreading in the orthogonal directions.

We illustrate the operation of such a coupler in a numerical example. The entire 3D structure to be modeled extends over a volume of $\sim 10^3 \mu m^3$ which is prohibitive for a full 3D FDTD simulation. On the other hand the BPM cannot accurately model the rapid variations along the propagation direction. We therefore decompose the problem into the xz-plane and the yz-plane and use the fact that the evolution of an elliptical Gaussian beam

can be traced separately in the two dimensions. The propagation of the gaussian beam in the layered medium is treated first and the associated effective index (see equation (2.93) in 2.6.1) is used to link the two analyses. In greater detail the modeling is performed as follows:

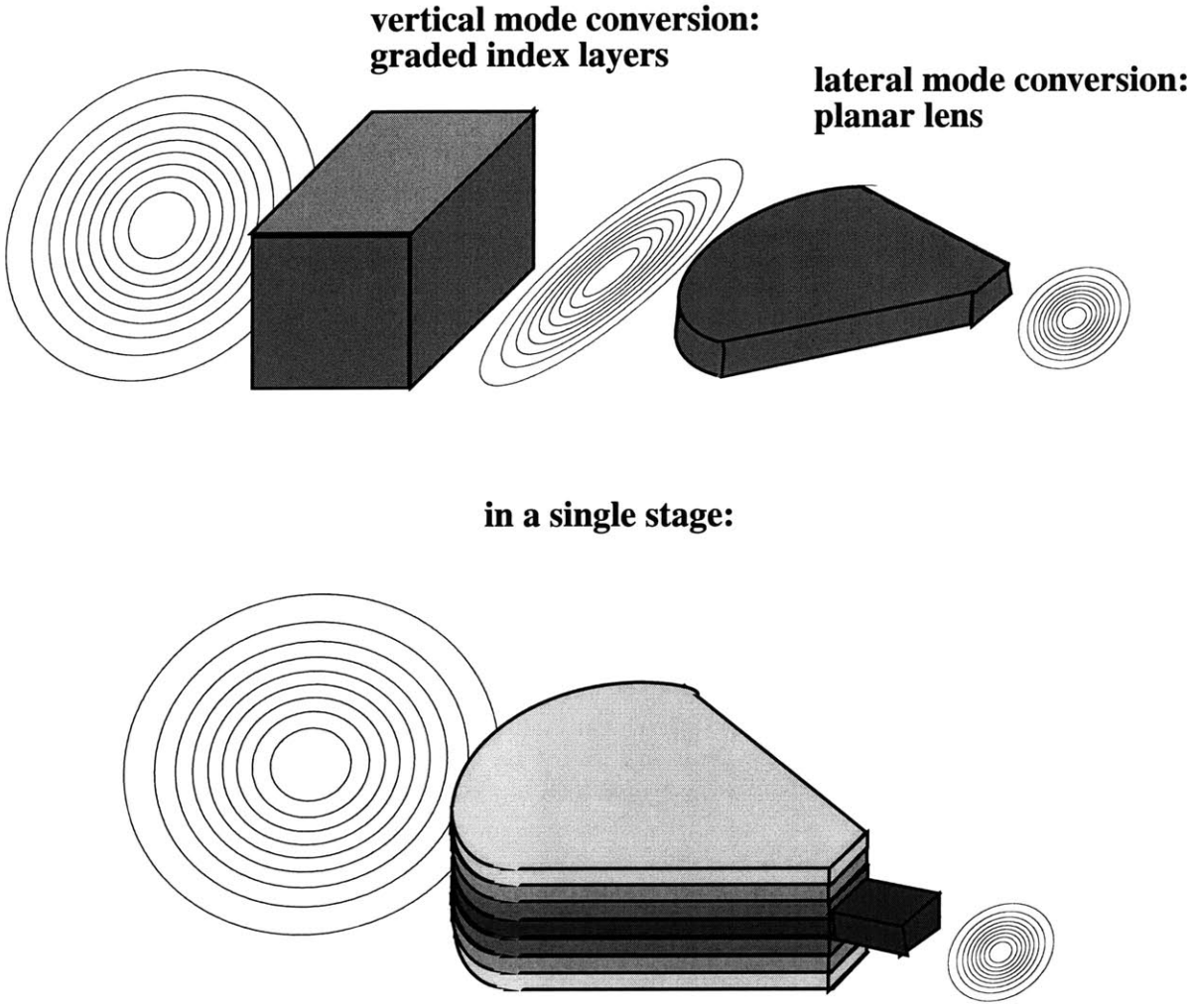

Figure 6.12: Combination of mechanisms for mode-size conversion: graded index in the vertical dimension and planar lens in the lateral dimension

Stage 1: graded index in the xz-plane

The layered structure has an index variation of the form

$$n(x,y) = \begin{cases} n_i\left(1 - \dfrac{x^2}{2h^2}\right) & |x| \le a \\ n_o & |x| > a \end{cases} \tag{6.2}$$

where, for continuity of the index distribution we use $h = a/\sqrt{2(1-n_o/n_i)}$. The length of the layered structure along z is equal to $\pi h/2$ which half the period of variation of the Gaussian beam width in the graded index region to ensure maximum beam width narrowing in the x direction. We find analytically the expected variation of the beam width along z and from it the variation of the associated effective index, given by:

$$n_e(z) = n_i\left[1 - \frac{1}{(k_o n_i w(z))^2}\right] \tag{6.3}$$

Figure 6.13 summarizes our analysis of this stage with $n_i = 2.5$ and $n_o = 1.5$ and $a = 3.2\mu m$. These particular index values were chosen such that the graded index is in the range approximately achievable with silicon nitrides. The additional 0.22 μm thick, $n = 1.5$ layer is for impedance matching (ideally its index should be $\sqrt{n_i} \approx 1.58$). The waveguide also has index $n_i = 2.5$ and cladding $n_o = 1.5$. With $h = 3.577\mu m$ the focal length is $\pi h/2 = f_1 \approx 5.62\mu m$.

Stage 2: planar "lens" in the yz-plane

A planar lensing structure is constructed using a material with the index variation of (6.3) and curved interfaces with radii chosen so that the beam is focused laterally in almost the same distance $\pi h/2$. If a shorter focal distance is obtained through non-optimal choice of lens curvature then, after having reached its minimum width, the beam will start spreading again before coupling to the waveguide. Similarly if the focal distance is larger than $\pi h/2$

the beam will couple into the waveguide before reaching its minimum width. Both cases would result in reduced coupling efficiency.

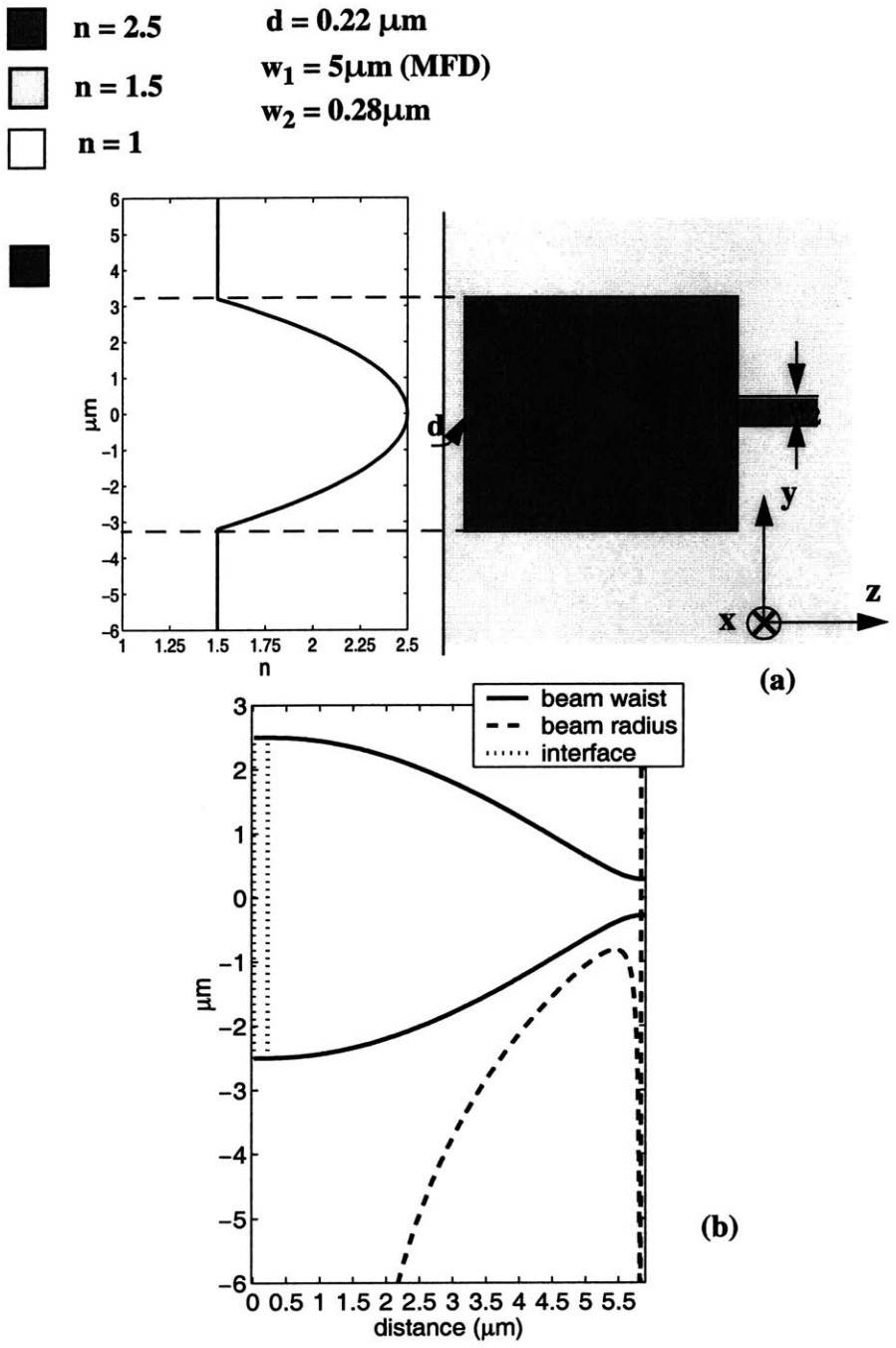

Figure 6.13: (a) Schematic of a lensing structure in the yz-plane based on graded index layers (b) Expected beam-width and phase-front radius evolution

The analytical modeling of this stage is summarized in Figure 6.14 The 0.22 μm thick, $n = 1.5$ layer serves again as a quarter-wave layer for impedance matching, (ideally this index should be $\sqrt{n_i} \approx 1.58$). The particular radii of curvature are chosen to give a focal length $f_2 \approx f_1$ as required for efficient coupling.

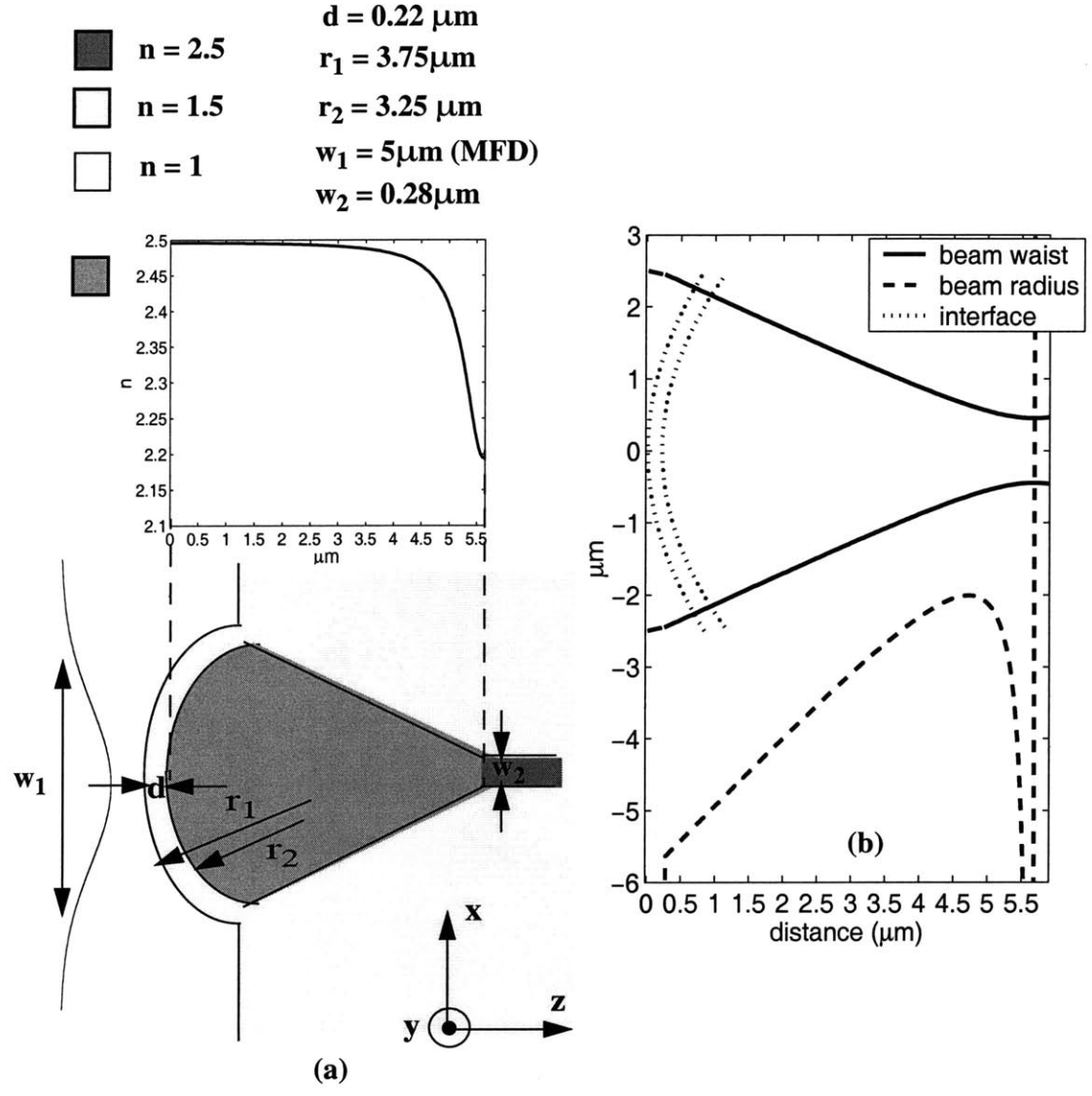

Figure 6.14: (a) Schematic of a lensing structure in the xz-plane (b) Expected beam-width and phase-front radius evolution

FDTD simulations

The numerical results are shown Figure 6.15 for forward propagation and in Figure 6.16 for backward propagation. As expected the coupling between fundamental modes is the same for both propagation directions due to reciprocity.

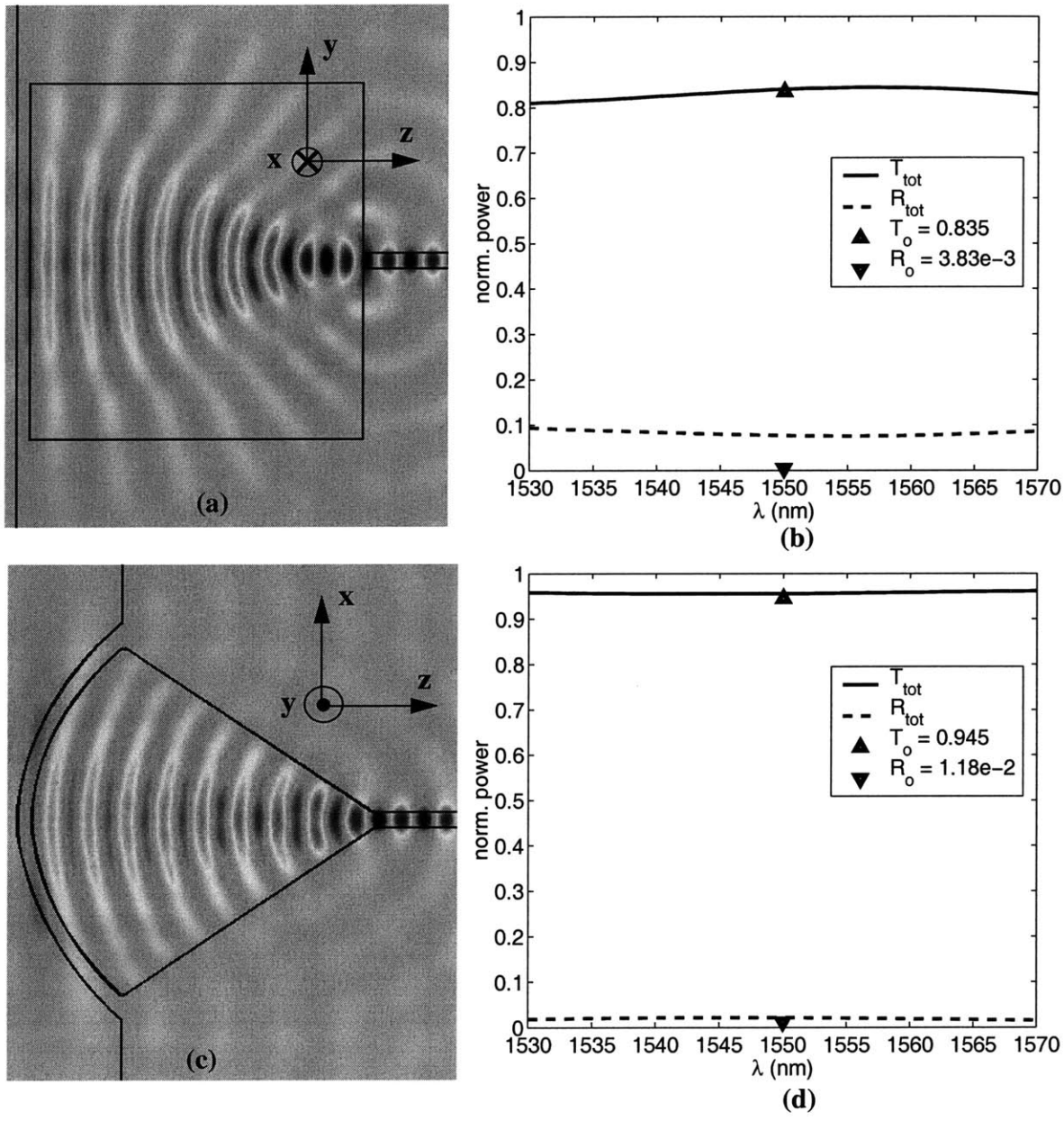

Figure 6.15: (a),(b) Electric field and associated spectra for forward propagation in the yz-plane and (c),(d) same in the xz-plane.

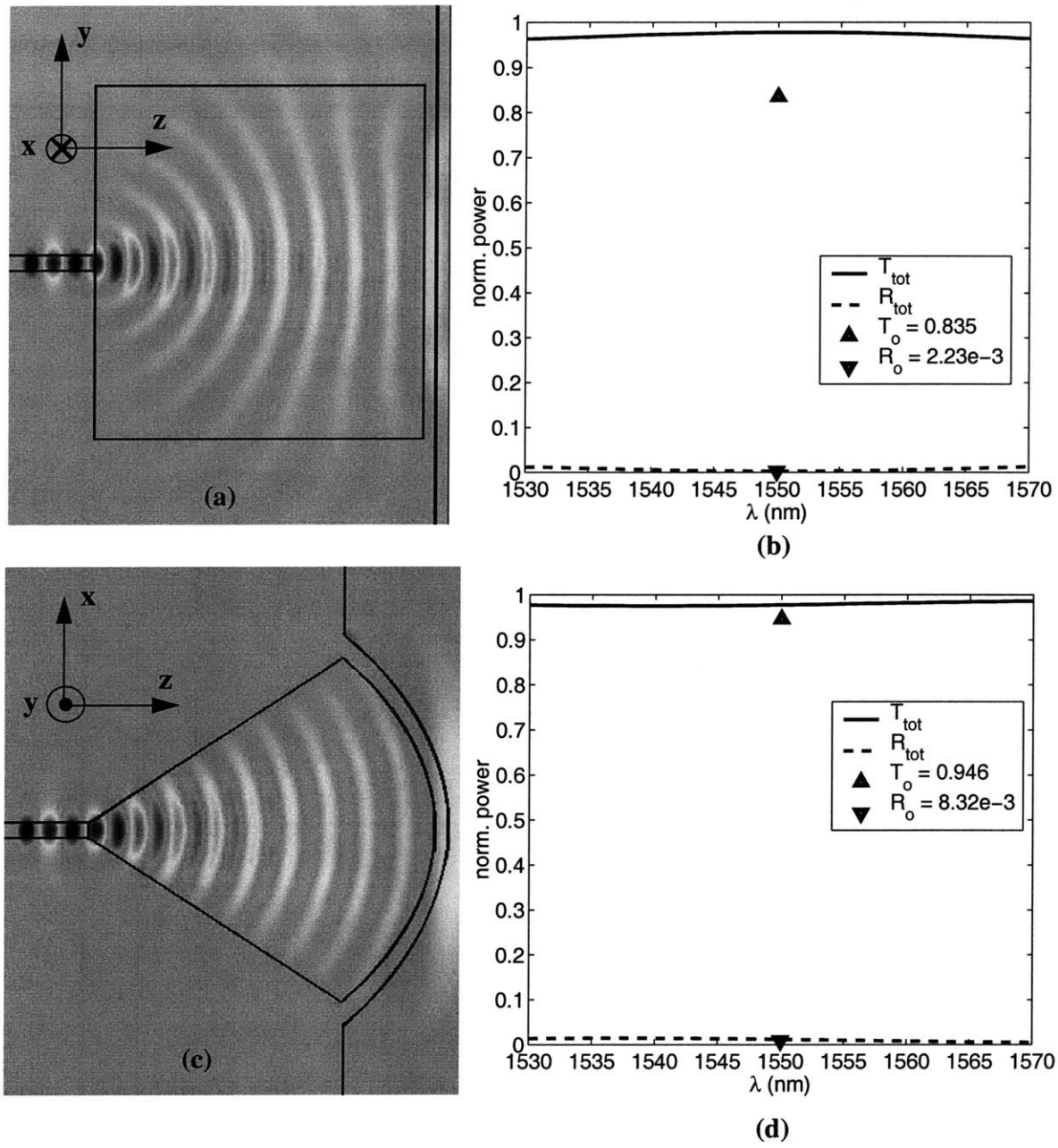

Figure 6.16: (a),(b) Electric field and associated spectra for backward propagation in the yz-plane and (c),(d) same in the xz-plane.

An estimate for the 3D coupling efficiency at 1550nm can be obtained as a product of the mode-to-mode 2D couplings in each plane, that is 0.835 x 0.945 = 0.79 which corre-

sponds to a coupling loss of about 1dB. Better coupling can be obtained with an optimized design especially in the yz-plane (graded index) where the radiation loss seems to be the main problem. In our example more than 15% of the input power was lost to radiation.

In conclusion lens-like fiber-PIC coupling schemes are easier to design, in comparison with the resonator cascades, since Gaussian beam analysis gives us a very good description of the expected beam evolution, while FDTD simulations are necessary to evaluate the transmission and rediation characteristics. Moreover these lens-like structures have a much broader transmission response and are less sensitive to design parameters than the resonant couplers. However their fabrication should be more challenging, especially since they involve curved interfaces that may be susceptible to surface roughness.

Chapter 7

Conclusions

In this thesis we have shown how certain concepts borrowed from physics, microwave engineering and optics can be applied to the design of passive integrated optics, yielding devices with very good performance. These concepts have general validity, but their success in our devices is greatly aided by the strong light confinement in high index-contrast structures which leads to low radiation loss and small device sizes, on the order of the optical wavelength. These are desirable characteristics that enable the dense integration of optical devices on a chip. An additional advantage towards this goal is offered by the fact that some of the main high index-contrast systems are based on silicon for which there are well established ULSI processing techniques.

The behavior of the structures presented here can be understood and qualitatively predicted by simple analytical methods such as CMT and Gaussian or ray optics. However due to the complexity of these structures, numerical techniques are required for accurate modeling and optimization. Our method of choice has been the FDTD which is a very powerful tool for modelling arbitrarily shaped structures, with discontinuities in both the propagation direction and the transverse direction and/or with resonant characteristics.

With our simulations we have verified the predictions of CMT analysis of resonant add/drop filters that are based on symmetry and degeneracy of standing wave modes to implement the function of a traveling wave resonator, e.g. a ring. These filters are very compact with sizes on the order of the optical wavelength and their response can be tailored to meet system specifications using multiple coupled resonators. The FDTD simulations have revealed that, in general, the performance of such high index-contrast devices is

very sensitive to small changes in their geometrical parameters, due to the high dispersion of high index-contrast waveguides.and the high-Q resonances involved. The design of this type of filters is thus very challenging, especially for higher orders, and their fabrication would be even more so. The strict fabrication tolerances create the need for tunability of these filters along with further improvement of fabrication and processing techniques.

FDTD simulations also showed that it is possible to achieve close to full transmission through sharp bends, splitters and crossings within a very small area by modifying the junction region into a low-Q cavity which we called high transmission cavity (HTC). The HTC bends and splitters are extremely broadband due to their weak resonant character and have better fabrication tolerance. The crossings have s stronger resonant character and are therefore more narrowband and sensitive to design parameter variation. Such components are essential for dense integration and optical interconnection of many different devices on a PIC.

Perhaps the most important problem to be overcome for high index-contrast microphotonics to be a viable technology, is the difficulty of coupling light from the optical fiber to the PIC and vice-versa. The coupling schemes proposed in the last chapter can perform the desired mode conversion within only a few microns (instead of several hundred microns in common mode-size converters) and relatively small radiation loss as our 2D FDTD simulations have shown. Using lensing mechanisms as opposed to resonant schemes has the advantage of broadband operation and simpler design since we can obtain a very good approximation through Gaussian and ray optics analysis. A combination of two focusing mechanisms is required for mode-size conversion both vertically and laterally e.g. using graded index and planar lensing, respectively. Our analysis and preliminary simulations have shown that such a coupling structure is promising and may be realizable using existing material systems and fabrication techniques. The drawback of this scheme is that the

layered structure in the vertical dimension must be sufficiently thick to capture the fiber mode (5-10μm) and the waveguide is buried deep into the substrate so this structure may not be very practical. It may thus be preferable to have the mode conversion take place closer to the chip surface. For example, a grating coupler can be used to couple the fiber light into the plane of the chip (shown in the schematic in Figure 7.1) followed by a lateral mode-converter e.g. an integrated lens. A grating coupler designed for operation at normal incidence [74] would enable vertical integration of fibers onto the chip which in turn may allow a larger number of fibers to be coupled to the chip. In addition to coupling other functions could be incorporated in the grating such as polarization splitting, [75]. The main concern about this coupling scheme is that, in general, gratings are narrowband. It may be possible however to broaden the wavelength range of operation by proper grating tooth design [76].

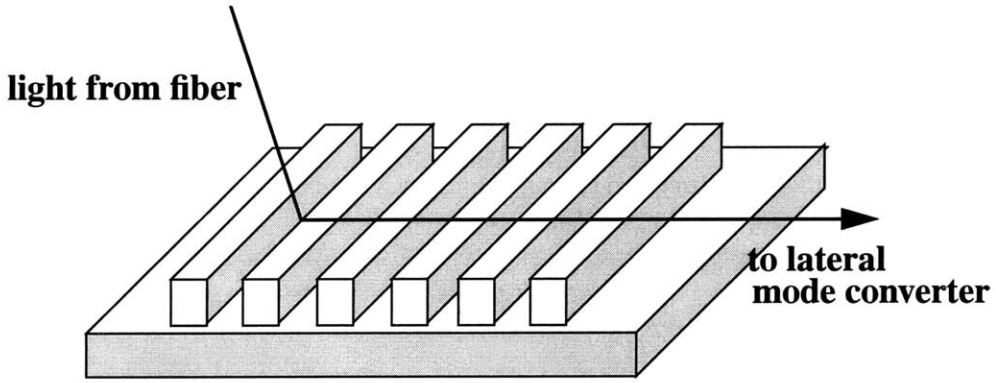

Figure 7.1: Schematic of a grating coupler for coupling light from the fiber into the plane of the chip

One of the main issues that have not been addressed in this work, is the strong polarization dependence of high index-contrast devices. This is of great importance since, usually the incoming light from an optical fiber is randomly polarized. In general TE- and

TM-like modes have very different propagation constants and degrees of confinement in high index-contrast waveguides leading to different behaviors in waveguide based devices. This is most important in resonant filters where the excitation of both polarizations in a cavity will result in split resonance peaks and deterioration of the filter performance. The design of polarization-insensitive high index-contrast structures is a very challenging if not impossible task. The polarization dependence may be reduced by using wave guiding structures with lower index-contrast and with cross-section aspect ratios close to 1, as was briefly discussed at the end of section 5.3. However it may impossible to maintain this condition throughout the various complex devices of a PIC.

A possible solution to this problem, which takes advantage of the very small real estate taken up by high index-contrast structures, is the use of two sets of components each optimized for one polarization as shown in the schematic of Figure 7.2(a). The system is preceded by a polarization splitter which separates the incoming, randomly polarized, light into TE-like and TM-like polarization. The two orthogonally polarized outputs from the two sets of devices are finally recombined and sent to the output fiber. This symmetric arrangement allows bidirectional operation. Because certain types of devices may have better performance for one of the two polarizations, an alternative solution would be to have two identical sets of devices optimized for one, say, TE polarization as shown in Figure 7.2(b). The simplification of the device design, which is now done only once, comes at a price, since we need two polarization rotators to convert the TM mode to TE after the splitting and back before the recombination, respectively. The polarization splitters and converters should ideally have small size, and most importantly low insertion loss and very broadband operation in order to accommodate all the WDM channels.

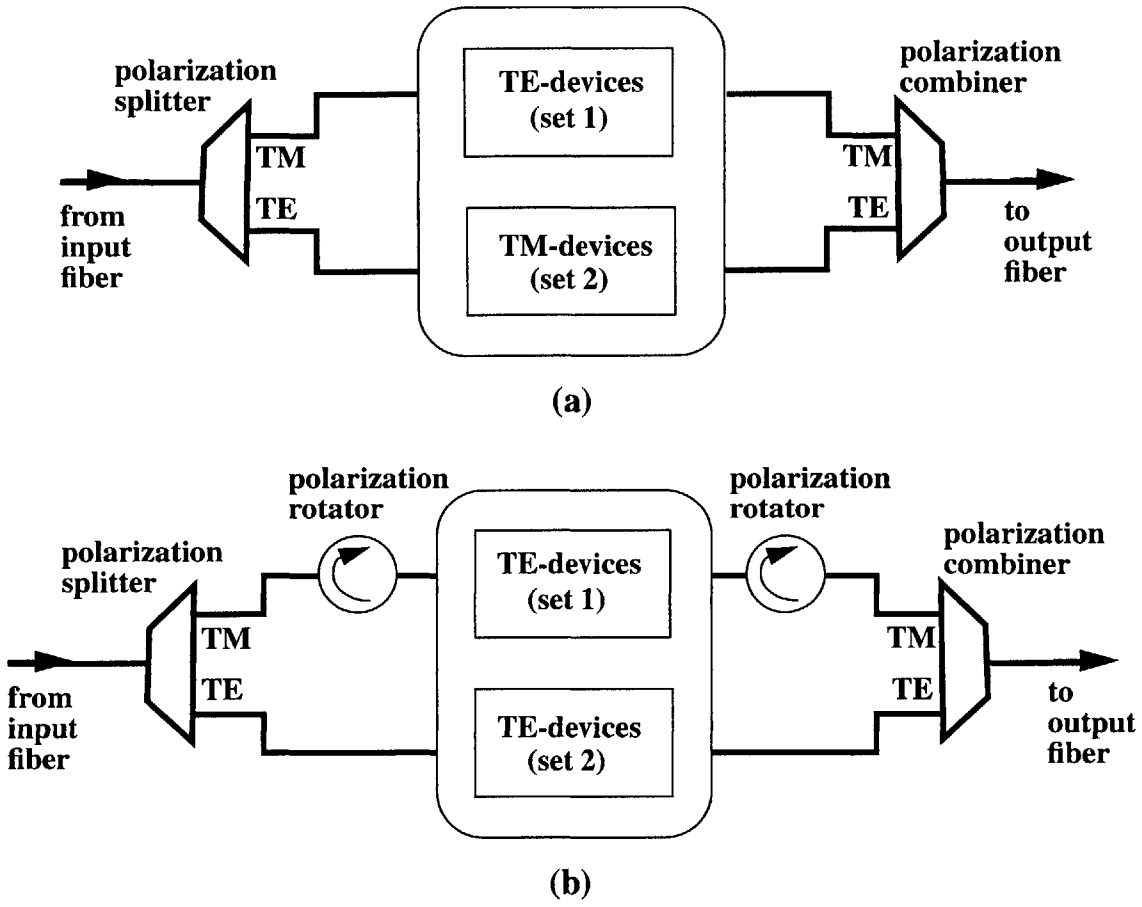

Figure 7.2: Schematic of a possible solution to the polarization-sensitivity problem using two sets of devices (a) each set is optimized for one polarization and (b) two identical sets optimized for one polarization

Polarization splitters can be based on waveguide coupler structures where the beat length of the two polarizations is different or where two or more waveguides are optically identical for one polarization and nonidentical for the other (see [77] and references therein). Such schemes are usually characterized by strict fabrication tolerances, very long lengths and narrow bandwidth which makes them unsuitable for WDM. An alternative mechanism is based on the polarization-dependent properties of asymmetric Y-branches,

where each arm favors a different polarization, and on the concept of mode evolution or mode sorting, (e.g. [78], [79] and references therein). This type of splitter can be shorter, with better fabrication tolerance and operation over a broad wavelength range.

Polarization converters using passive isotropic structures can be based on asymmetric waveguides such as periodic asymmetric-loaded waveguides and angled facet waveguides, or interaction between hybrid supermodes ([80] and references therein). These devices usually involve some critical length (in general associated with narrow-band operation and strict fabrication tolerances), and may require multiple segments and/or long lengths for 90^{o} polarization rotation. An alternative scheme makes use of the polarization rotation that occurs in small-radius bends in deeply etched waveguides [81]. As suggested in [82] the device performance is strongly dependent on the geometrical characteristics of the bending waveguide; however its in essentially wavelength independent and thus suitable for WDM applications.

Although the FDTD is a powerful tool for modelling arbitrarily shaped structures, we cannot rely entirely on it for analyzing systems of varying complexity and many wavelengths long: The the main drawback of FDTD is the enormous time and memory requirement when solving optically long and/or highly resonant structures. This is especially true when the PML boundary conditions are used, since all the fields are split into two components as discussed in Chapter 2. Thus it is essentially impossible to model any 3D structure that is larger than few μm in each direction and we have been mostly limited to 2D simulations where the third direction is taken into account by EIM. The accuracy of this approach is greater for high aspect ratios and when there is little radiation in the vertical direction. This was verified for the HTC bends which, due to their small size and weak resonant character were best suited for 3D FDTD simulations. Their fabrication and testing at MIT offered the opportunity to compare the 3D FDTD data with experimental as

well as with 2D FDTD results and find them in very good agreement. Even non-optimized HTC bends had well under 1dB loss, of which a negligible amount was due to radiation into the substrate. The allowable size of the computational domain that can be simulated in 3D can be almost doubled if we replace the PML boundary conditions with less costly ABCs e.g. [16],[17]. The trade-off is an increase of the spurious reflections from the computational border by orders of magnitude compared to the PML but this may be afforded for systems that do not radiate much into the surrounding space. For optically long structures it may be necessary to combine the FDTD with different numerical and/or analytical methods e.g. BPM, CMT, etc., which can analyze long structures with adiabatic transitions very effectively, thus limiting the use of FDTD to the more complex parts of the system [83].

References

[1] S.E. Miller, "Integrated optics: An introduction", *Bell Sys.Tech. J.*, pp 2059-2069, Sept. 1969

[2] E.A.J. Marcatilli, "'Bends in optical dielectric waveguides", *Bell Sys.Tech. Journal,* pp.2103-2132, Sept.1969.

[3] C. Vassalo, *"Optical Waveguide Concepts"*, Amsterdam, New York : Elsevier, 1991.

[4] A.Yariv, *"Optical Electronics"*, Philadelphia : Saunders College Pub., 1991.

[5] D. Marcuse, *"Light Transmission Optics"*, New York : Van Nostrand Reinhold, 1982.

[6] H.A. Haus, "*Waves and Fields in Optoelectronics*", Prentice-Hall, Englewood Cliffs, NJ, 1984.

[7] L. A. Coldren, S. W. Corzine, "Diode lasers and photonic integrated circuits", New York : Wiley, 1995.

[8] M. D. Feit, J. A. Fleck, Jr., "Computation of mode properties in optical fiber waveguides by a propagating beam method", *Appl. Opt.*, vol. 19, no. 7, pp. 1154-1163, 1980.

[9] D. Yevick, B. Harmansson, "Efficient beam propagation techniques", *IEEE J. Quant. Electron.*, vol. 26, no.1, pp. 109-112, Jan. 1990.

[10] F. Ma, C. L. Xu, W. P. Huang, "Wide-angle full vectorial beam propagation method", *IEE Proc.-Optoelectron.*, vol. 143, no. 2, pp. 139-143, April 1996.

[11] H. Rao, R. Scarmozzino, R. M. Osgood, Jr., "A bidirectional beam propagation method for multiple dielectric interfaces", *IEEE Photon. Technol. Lett.*, vol. 11, no. 7, pp. 830-832, July 1999.

[12] S. T. Chu, S. K. Chauduri, "A finite-difference time-domain method for the design and analysis of guided-wave optical structures", *J. Lightwave Technol.*, vol. 7, no. 12, pp. 2033-2038, Dec. 1989.

[13] K. S. Kunz, R. J. Luebbers, "The finite difference time domain method for electromagnetics", Boca Raton : CRC Press, 1993.

[14] A. Taflove, "Computational electrodynamics : the finite-difference time-domain method", Boston : Artech House, 1995.

[15] K.S. Yee, "Numerical solution of the initial boundary value problems involving Maxwell's equations in isotropic media", *IEEE Trans. Ant. and Prop.*, vol.AP-14, pp.302-307, May 1966.

[16] G.Mur, "Absorbing boundary conditions for the finite-difference approximation of the time-domain electromagnetic-field equations", *IEEE Trans. on Electromag. Compatib.,* vol.EMC-23, no.4, pp.377-382, Nov. 1981.

[17] B. Engquist, A. Majda, "Absorbing boundary conditions for the numerical simulation of waves", *Math. Computation.*, vol. 31, no. 139, pp. 629-51, 1977.

[18] R. Hidgon, "Numerical absorbing conditions for the wave equation", *Math. Comput.*, vol. 49, no. 179, pp. 65-90, July 1987.

[19] J.P. Berenger, "A perfectly matched layer for the absorption of electromagnetic waves", *J. Comp. Phys.*, vol.114, no.2, pp.185-200, Oct. 1994.

[20] J.P. Berenger, "Perfectly matched layer for the FDTD solution of wave-strucure interaction problems", *IEEE Trans. Antennas Propagat.*, vol. 44, no. 1, pp. 110-117, Jan. 1996.

[21] W. C. Chew, W. H. Weedon, "A 3D perfectly matched medium from modified Maxwell's equations with stretched coordinates", *Microwave Opt. Technol. Lett.*, vol. 7, no. 13, pp. 599-605, Sept. 1994.

[22] D. S. Katz, E. T. Thiele, A. Taflove, "Validation and extension to three dimensions of the Berenger PML absorbing boundary condition for FDTD meshes", *IEEE Microwave Guided Wave Lett.*, vol. 4, pp. 268-70, Aug. 1994.

[23] C. E. Reuter, R. M. Joseph, E. T. Thiele, D. S. Katz, A. Taflove, "Ultrawideband absorbing boundary condition for termination of waveguiding structures in FD-TD simulations", *IEEE Microwave Guided Wave Lett.*, vol. 4, no. 10 , pp 344-346, Oct. 1994.

[24] J. De Moerloose, M. A. Stuchly, "Behavior of Berenger's ABC for evanescent waves", *IEEE Microwave Guided Wave Lett.*, vol. 5, no. 10 , pp 344-346, Oct. 1995.

[25] W. P. Huang, C. L. Xu, W. Lui, K. Yokoyama, "The perfectly matched layer boundary condition for modal analysis of optical waveguides: leaky mode calculations", *IEEE Photon. Technol. Lett.*, vol. 8, no. 5, pp. 652-654, May 1996.

[26] W. P. Huang, C. L. Xu, W. Lui, K. Yokoyama, "The perfectly matched layer (PML) boundary condition for the beam propagation method", *IEEE Photon. Technol. Lett.*, vol. 8, no. 5, pp. 649-651, May 1996.

[27] J. Chen, K. Li, "Quartic perfectly matched layers for dielectric waveguides and gratings", *Microwave Opt. Technol. Lett.* Dec. 20, 1995.

[28] M. S. Stern, "Semivectorial polarized finite difference method for optical waveguides with arbitrary index profiles", *IEE Proc.-J*, vol. 135 , no.1, pp. 56-63, 1988.

[29] C. L. Xu, W. P. Huang, M. S. Stern, S. K. Chaudhuri, "Full-vectorial mode calculations by finite difference method", *IEE-Proc.-Optoelectron.*, vol. 141, no. 5, pp. 281-286, Oct. 1994.

[30] E. A. J. Marcatilli, "Dielectric rectangular waveguide and directional coupler for integrated optics", *Bell Syst. Tech. J.*, vol. 48, pp. 2133-2160, 1969.

[31] R. M. Knox, P. P. Toulios, "Integrated circuits for the millimeter through optical frequency region", *Proc. MRI Symp. Submillimeter Waves*, pp. 497-516, 1970.

[32] C. Dragone, C.A. Edwards, R.C. Kistler, "Integrated optics NxN multiplexer on silicon", *IEEE Photon. Technol. Lett.*, vol.3, no.10, pp.896-9, Oct. 1991.

[33] M. K. Smit, C. van Dam, "PHASAR-based WDM-devices: Principles, design and applications", *IEEE J. Selected Topics Quant. Electron,* vol. 2, no. 2, pp 236-250, June 1996

[34] H.A. Haus, Y. Lai, "Theory of cascaded quarter wave shifted distributed feedback resonators", *IEEE J. Quant. Electron.,* vol.28, no.1, pp.205-213, Jan.1992.

[35] H.A. Haus, Y. Lai, "Narrow-band optical channel-dropping filter", *J. Lightwave Technol.,* vol.10, no.1, p. 57-62, Jan. 1992.

[36] B. E. Little, S. T. Chu, H. A. Haus, J. S. Foresi, J.-P. Laine, "Microring resonator channel dropping filters", *J. Lightwave Technol.*, vol.15, no. 6, pp 998-1005, June 1997.

[37] D. Rafizadeh, J.P. Zhang, S.C. Hagness, A. Taflove, K.A. Stair, S.T. Ho, R.C. Tiberio, "Waveguide-coupled AlGaAs/GaAs microcavity ring and disk resonators with high finesse and 21.6-nm free spectral range", *Opt. Lett.*, vol.22, no.16, pp.1244-1246, Aug. 1997.

[38] S.C. Hagness, D. Rafizadeh, S.T. Ho, A. Taflove, "FDTD microcavity simulations: design and experimental realization of waveguide-coupled single-mode ring and whispering-gallery-mode disk resonators", J. *Lightwave Technol.,* vol.15, no.11, pp.2154-65, Nov. 1997.

[39] B. E. Little, J. S. Foresi, G. Steinmeyer, E. R. Thoen, S. T. Chu, H. A. Hans, E. P. Ippen, L. C. Kimerling, W. Greene, "Ultra-compact Si-SiO_2 microring resonator optical channel dropping filters", *IEEE Photon. Technol. Lett.*, vol. 10, no. 4 , pp 549-551, April 1998.

[40] B. E. Little, H. A. Haus, J. S. Foresi, L. C. Kimerling, E. P. Ippen, D. J. Ripin, "Wavelength switching and routing using absorption and resonance", *IEEE Photon. Technol. Lett.*, vol. 10, no. 6 , pp. 816-818, June 1998.

[41] B.E. Little, J.-P. Laine, S.T. Chu, "Surface-roughness-induced contradirectional coupling in ring and disk resonators", *Opt. Lett.,* vol.22, no.1, pp.4-6, Jan. 1997.

[42] M. K. Chin, C. Youtsey, W. Zhao, T. Pierson, Z. Ren, S. L. Wu, L. Wang, Y. G. Zhao, S. T. Ho, "GaAs Microcavity Channel-Dropping Filter Based on a Race-Track Resonator", *IEEE Photon. Technol. Lett.*, vol. 11, no. 12, pp. 1620-1622, Dec.1999.

[43] P. R. Villeneuve, S. Fan, J. D. Joannopoulos, "Microcavities in photonic crystals: mode symmetry, tunability, and coupling efficiency", *Phys. Rev. B-Condensed Matter*, vol.54, no.11, pp 7837-42, Sept. 1996.

[44] S. Fan, P. R. Villeneuve, J.D. Joannopoulos, H.A. Haus, "Channel drop tunneling through localized states", *Phys. Rev. Lett.*, vol.80, no.5, pp.960-3, 1998.

[45] S. Fan, P. R. Villeneuve, J. D. Joannopoulos, M. J. Khan, C. Manolatou, H. A. Haus, "Theoretical analysis of channel drop tunneling processes", *Phys. Rev. B*, vol. 59, no. 24, pp 883-892, June 1999.

[46] S. Fan, P. R. Villeneuve, J. D. Joannopoulos, "Theoretical investigation of fabrication-related disorder on the properties of photonic crystals", J. Appl. Phys. vol. 78, no. 3, pp.1415-1418, Aug. 1995.

[47] C. Manolatou, M. J. Khan, S. Fan, P. R. Villeneuve, H. A. Haus, J. D. Joannopoulos, "Coupling of modes analysis of resonant channel add/drop filters", *IEEE J. Quantum Electron.,* vol.35, no.9, pp.1322-1331, Sept. 1999.

[48] M.J. Khan, C. Manolatou, S. Fan, P. R. Villeneuve, H. A. Haus, J. D. Joannopoulos, "Mode Coupling Analysis of Multipole Symmetric Resonant Add/Drop Filters", *IEEE J. Quant. Electron.,* vol.35, no.10, pp.1451-1460, Oct. 1999.

[49] G. Lenz, B. J. Eggleton, C. R. Giles, C. K. Madsen, R. E. Slusher,"Dispersive properties of optical filters for WDM systems", *IEEE J. Quant. Electron.*, vol.34, no.8, pp.1390-1402, Aug. 1998.

[50] G. Lenz, B. J. Eggleton, C. K. Madsen, C. R. Giles, G. Nykolak, "Optimal dispersion of optical filters for WDM systems", *IEEE Photon. Technol. Lett.*, vol.10., no.4, pp. 567-569, April 1998.

[51] B.J. Eggleton, G. Lenz, N. Litchinitser, D.B. Patterson, R.E. Slusher, "Implications of fiber grating dispersion for WDM communication systems", *IEEE Photon. Technol. Lett.* , Vol. 9, no. 10 , pp. 1403-1405, Oct. 1997.

[52] G. P. Agrawal, *"Nonlinear fiber optics"*, San Diego : Academic Press, 1995.

[53] A. Mekis, J. C. Chen, I. Kurland, S. Fan, P. R. Villeneuve, J. D. Joannopoulos, "High transmission through sharp bends in photonic crystal waveguides", *Phys. Rev. Lett.,* vol.77, no.18, pp.3787-90. Oct. 1996.

[54] S. G. Johnson, C. Manolatou, S. Fan, P. R. Villeneuve, J. D. Joannopoulos, H. A. Haus, "Elimination of crosstalk in waveguide intersections", *Optics. Lett.,* vol.23, no.23, pp.1855-1857, Dec. 1998.

[55] E.G. Neumann, "Reducing radiation loss of tilts in dielectric optical waveguides", *Electron. Lett.,* vol.17, no.5 pp.369-371, 1986.

[56] T. Shiina, K. Shirashi, S. Kawakami, "Waveguide-bend configuration with low-loss characteristics", *Opt. Lett.,* vol.11, no 11, p. 736-738, 1986.

[57] H.B. Lin, J.Y. Su, P.K. Wei, W.S. Wang, "Design and application of very low-loss abrupt bends in optical waveguides", *IEEE J. Quant. Electron.*, vol.QE-30, no.12, pp.2827-2835, Dec. 1994.

[58] H.F. Taylor, "Losses at corner bends in dielectric waveguides", *Appl. Opt.,* vol.16, no.3, pp.711-716, 1977.

[59] K. Ogusu, "Transmission characteristics of optical waveguide corners", *Opt. Commun.*, vol.55, no.3, pp.149-153, 1985.

[60] J. S. Foresi, D.R. Lim, L. Liao, A.M. Agarwal, L.C. Kimerling, "Small radius bends and large angle splitters in SOI waveguides", *Proc. SPIE,* vol.3007, pp.112-118, 1997.

[61] J. S. Foresi, "Optical Confinement and Light Guiding in High Dielectric Contrast Material Systems" , PhD Thesis, MIT, 1997.

[62] D. R. Lim, "Device Integration for Silicon Microphotonics Platforms", PhD Thesis, MIT, 2000.

[63] M. H. Hu, J. Z. Huang, R. Scarmozzino, M. Levy, R. M. Osgood Jr., "A low-loss and compact waveguide Y -branch using refractive index tapering", *IEEE Photon. Technol. Lett.*, vol. 9, no. 2, pp. 203-205, Feb. 1997.

[64] M. H. Hu, J. Z. Huang, R. Scarmozzino, M. Levy, R. M. Osgood Jr., "Tunable Mach-Zehnder polarization splitter using height-tapered Y -branches", *IEEE Photon. Technol. Lett.*, vol. 9, no. 6, pp. 773-775, June 1997.

[65] H. B. Lin, R. S. Cheng, and W. S. Wang, "Wide-angle low-loss single-mode symmetric Y-juntions", *IEEE Photon. Technol. Lett.*, vol. 6, July 1994.

[66] M. G. Daly, P. E. Jessop, D. Yevick, "Crosstalk reduction in intersecting rib waveguides", *J. Lightwave Technol.* , vol.14, no.7, p. 1695-8, July 1996.

[67] C. Manolatou, S.G. Johnson, S. Fan, P.R. Villeneuve, H.A. Haus, J.D. Joannopoulos, "High-Density Integrated Optics", *J. Lightwave Technol.,* vol.17, no.9, pp.1682-1692, Sept. 1999.

[68] W. B. Joyce, B. C. DeLoach, "Alignment of Gaussian beams", Appl. Opt., vol. 23, no. 23, pp. 4187-4196, Dec. 1984.

[69] C. A. Edwards, H. M. Presby, C. Dragone, "Ideal microlenses for laser to fiber coupling", *J. Lightwave Technol.,* vol.11, no.2, p. 252-257, Feb. 1993.

[70] K. Shiraishi, A. Ogura, K. Matsura, "Spotsize contraction in standard single mode fiber by use of a GI-fiber tip with a high focusing parameter", *IEEE Photon. Technol. Lett.*, vol. 10, no. 12, pp 1757-1759, Dec. 1998

[71] T. Brenner, H. Melchior, "Integrated optical modeshape adapters in InGaAsP/InP for efficient fiber-to-waveguide coupling", *IEEE Photon. Technol. Lett.,* vol. 5, no. 9, pp 1053-1056, Sept. 1993

[72] Y. Itaya, Y. Tohmori, H. Toba, "Spot-size converter integrated laser diodes (SS-LD's)", *IEEE J. Selected Topics Quant. Electron,* vol. 3, no. 3, pp 968-974, June 1997

[73] S. Saini, V. Vusirikala, R. Whaley, F.G. Johnson, D. Stone, M. Dagenais, "Compact mode expanded lasers using resonant coupling between a 1.55μm InGaAsP tapered active region and an underlying coupling waveguide", *IEEE Photon. Technol. Lett.*, vol. 10, no. 9, pp. 1232-1234, Sep. 1998.

[74] G.W. Taylor, C. Kwan, "Diffraction into a corrugated waveguide from normally incident radiation", *J. Lightwave Technol.*, vol. 16, no. 12, pp. 2393-2400, Dec. 1998.

[75] .S. Ura, H. Sunagawa, T. Suhara, H. Nishihara, "Focusing grating couplers for polarization detection", *J. Lightwave Technol.*, vol. 6, no. 6, pp. 1028-1033, June 1988.

[76] S. Zhang, T. Tamir, "Analysis and design of broadband couplers", *IEEE J. Quant. Electron.*, vol. 29, no. 11, pp. 2813-2824, Nov. 1993.

[77] U. Trutschel, F. Ouellette, V. Delisle, M. A. Duguay, G. Fogarty, F. Lederer, "Polarization splitter based on antiresonant reflecting optical waveguides", *J. Lightwave Technol.*, vol. 13, no. 2, pp. 239-243, Feb. 1995.

[78] R. M. de Ritter, A. F. M. Sander, A. Driessen, J. H. J. Fluitman, "An integrated optic adiabatic TE/TM polarization splitter on silicon", *J. Lightwave Technol.* vol. 11, no. 11, pp. 1806-1811, Nov. 1993.

[79] J. J. G. M. van der Tol, J. W. Petersen, E. G. Metaal, Y. S. Oei, H. van Brug, I. Moerman, "Mode evolution type polarization splitter on InGaAsP/InP", *IEEE Photon. Technol. Lett.,* vol. 5, no. 12, pp. 1412-1414, Dec. 1993.

[80] J. Z. Huang, R. Scarmozzino, G. Nagy, M. J. Steel, R. M. Osgood, Jr. , "Realization of a compact and single-mode optical passive polarization converter", *IEEE Photon. Technol. Lett.*, vol. 12, no. 3, pp. 317-319, March 2000.

[81] C. van Dam, L. H. Spiekman, F. P. G. M. van Ham, F. H. Groen, J. J. G. M. van der Tol, I. Moerman, W. W. Pascher, M. Hamacher, H. Heidrich, C. M. Weinert, M. K. Smit, "Nover polarization converters based on ultra short bends", *IEEE Photon. Technol. Lett.*, vol. 8, no. 10, pp. 1346-1348, Oct. 1996.

[82] W. W. Lui, T. Hirono, K. Yokoyama, W-P. Huang, "Polarization rotation in semiconductor bending waveguides: A coupled-mode theory formulation", *J. Lightwave Technol.*, vol. 16, no. 5 , pp. 929-936, May 1998.

[83] S. T. Chu, W. P. Huang, S. K. Chaudhuri,"Simulation and analysis of waveguide based optical integrated circuits", *Comp. Phys. Commun.*, vol. 68, no.1-3, pp.451-84, Nov. 1991.